

Dissertation

submitted to the

Combined Faculty of Natural Sciences and Mathematics

of the Heidelberg University, Germany

for the degree of

Doctor of Natural Sciences

Put forward by

Isabela Paredes Cisneros,

born in Popayán, Colombia

Oral examination: 3rd of May, 2022

**Validation of an oxygen-dependent tumour response simulation model
in three sublines of a rat prostate carcinoma**

Referees: Prof. Dr. Joao Seco
Prof. Dr. Christian Karger

Summary

Radiotherapy outcome of poorly oxygenated tumours is currently limited. Mathematical models describing the oxygen-dependent tumour response may help to optimise treatment schedules and improve radiotherapy outcome. The tumour response model (TRM) predicts the spatiotemporal development of tumours based on radiation dose, microscopic oxygenation distributions, proliferation of tumour cells, angiogenesis, tumour growth, resorption of dead tumour cells and tumour shrinkage. In this thesis, the TRM was validated and its input parameters were adjusted to reproduce experimental dose-response curves of three rat prostate carcinoma sublines. The validation confirmed the correct implementation of the main TRM components and the dependence on input parameters were consistent with underlying principles. The adjustment to experimental data could only be achieved after changing the assumption on oxygen consumption of radiation-inactivated tumour cells. The adjusted intrinsic fractionation parameter, α/β , was smaller than the experimentally obtained value, revealing the impact of additional biological processes on the tumour response to fractionated irradiations. Additionally, available experimental α/β and α values were compatible with the values adjusted in the TRM. This study demonstrates the ability of the TRM to reproduce experimental *in-vivo* tumour response data.

Zusammenfassung

Die Ergebnisse der Strahlentherapie bei schlecht mit Sauerstoff versorgten Tumoren sind derzeit begrenzt. Mathematische Modelle, die die sauerstoffabhängige Reaktion des Tumors beschreiben, können dazu beitragen, die Behandlungspläne zu optimieren und die Ergebnisse der Strahlentherapie zu verbessern. Das Tumor-Response-Modell (TRM) prognostiziert die räumlich-zeitliche Entwicklung von Tumoren basierend auf der Strahlendosis, der mikroskopischen Sauerstoffverteilung, der Proliferation von Tumorzellen, der Angiogenese, des Tumorwachstums, der Resorption abgestorbener Tumorzellen und der Schrumpfung des Tumors. In dieser Arbeit wurde das TRM validiert und seine Eingangsparameter wurden angepasst, um experimentelle Dosis-Wirkungs-Kurven von drei Sublinien eines Ratten-Prostatakarzinoms zu reproduzieren. Die Validierung bestätigte die korrekte Implementierung der Hauptkomponenten des TRM, und die Abhängigkeit von den Eingangsparametern war konsistent mit den zugrunde liegenden Prinzipien. Die Anpassung an die experimentellen Daten konnte nur durch eine Änderung der Annahme über den Sauerstoffverbrauch von strahlungsinaktivierten Tumorzellen erreicht werden. Der angepasste intrinsische Fraktionierungsparameter, α/β , war kleiner als der experimentell ermittelte Wert, was den Einfluss zusätzlicher biologischer Prozesse auf die Reaktion des Tumors auf die fraktionierte Bestrahlungen offenbart. Außerdem waren die verfügbaren experimentellen α/β - und α -Werte mit den im TRM angepassten Werten kompatibel. Die Studie demonstriert die Fähigkeit des TRM, experimentelle in-vivo-Tumorreaktionsdaten zu reproduzieren.

*Para mi abuela,
Ana Myriam*

*“For small creatures such as we the vastness
is bearable only through love”*

Carl Sagan
Contact (1985)

Table of Contents

List of Abbreviations	xi
1 Introduction	1
2 Materials and methods	3
2.1 Background.....	3
2.1.1 Physics of radiotherapy	3
2.1.2 Radiobiology.....	6
2.2 Tumour response model (TRM).....	15
2.2.1 Model structure.....	16
2.2.2 Initial characterization of the tissue	17
2.2.3 Tumour oxygenation model (TOM).....	18
2.2.4 Biological processes in the TRM.....	20
2.2.5 Integration with the Medical Imaging Interaction Toolkit (MITK).....	23
2.3 Improvement of the TRM.....	23
2.4 Adjustment of the TRM to experimental <i>in-vivo</i> data	24
2.4.1 Experimental <i>in-vivo</i> data	25
2.4.2 Adjustment to experimental <i>in-vivo</i> data	29
2.4.3 Simulations.....	32
3 Results	37
3.1 Validation by analytical calculations.....	37
3.2 The interplay of key input parameters	40
3.3 Adjustment to experimental <i>in-vivo</i> data	43
3.3.1 Experimental tumour parameters.....	43
3.3.2 AT1 tumour subline.....	43
3.3.3 HI tumour subline	48
3.3.4 H tumour subline	49

3.3.5	Summary of adjusted parameters	51
4	Discussion.....	54
4.1	Validation by analytical calculations.....	54
4.2	The interplay of key input parameters	55
4.3	Adjustment to experimental <i>in-vivo</i> data	55
4.3.1	AT1 tumour subline.....	56
4.3.2	Cell death and oxygen availability.....	57
4.3.3	HI and H tumour sublines	58
4.3.4	Modelling of tumour heterogeneity.....	59
4.3.5	Impact of the choice of OF and AQM.....	60
4.3.6	Biological interpretation of the adjusted α/β	60
4.4	Limitations and challenges.....	62
5	Conclusion	64
6	Outlook.....	65
	Appendix.....	66
	Publications.....	67
	Bibliography.....	68
	Acknowledgements.....	74

List of Abbreviations

AQM	Adjustment quantitative metric
CC	Capillary cell
CD31	Cluster of differentiation 31
CK19	Cytokeratin 19
CT	Computed tomography
DAPI	4',6-diamidino-2-phenylindole
DC	Dead cell
DF	Dead fraction
DNA	Deoxyribonucleic acid
fx	Fraction
H&E	Haematoxylin and eosin
HF	Hypoxic fraction
LQM	Linear quadratic model
MITK	Medical Imaging Interaction Toolkit
MRI	Magnetic resonance imaging
NC	Normal cell
OER	Oxygen enhancement ratio
OF	Objective function
PET	Positron emission tomography
PF	Proliferation factor
pO_2	Spatiotemporal distribution of oxygen partial pressure
RN	Random number
RT	Resorption half-time
SD	Standard deviation
SE	Standard error
SF	Survival fraction
ST	Slice thickness
TC	Tumour cell
TCP	Tumour control probability
TOM	Tumour oxygenation model
TRM	Tumour response model
VDT	Volume doubling time
VF	Vascular fraction

1 Introduction

The uncontrolled growth and subsequent spread of abnormal cells characterise the group of diseases known as cancer. Certain environmental factors are known to increase cancer risk, but the causes of this disease remain mostly unknown and are the subject of ongoing research. Cancer leads to one out of six deaths worldwide and as of 2018, is the second-leading cause of death, surpassed only by cardiovascular diseases [1].

Radiotherapy uses ionising radiation to kill cancer cells and is currently an essential component of effective cancer treatment. Approximately half of the cancer patients would benefit from radiotherapy to cure the disease and alleviate symptoms [2], [3]. A clear relationship between the tumour response to radiation and the delivered radiation dose has been observed when radiotherapy is used with curative intent. This dose-dependent response is influenced by the intrinsic tumour cell sensitivity to radiation, as well as by additional biological processes and microenvironmental factors [4]. Improvements in radiotherapy outcome have been achieved thanks to the latest technological developments. These allow delivering highly conformal dose distributions to the tumour while minimising the dose to the surrounding healthy tissue. Nonetheless, radiotherapy efficacy is still compromised by various factors, especially by the deficient oxygenation, referred to as hypoxia, present in most solid tumours [5].

The impact of oxygen on tumour response to radiation was first described by Gray in 1953 [6]. Since then, several studies established the negative impact of hypoxia on radiotherapy outcome in terms of local disease control and overall survival [5], [7]. Hypoxia is caused by the rapid growth of solid tumours, which increases the oxygen demand on the existing tumour vasculature. Driven by this high oxygen demand, new tumour vasculature is rapidly formed. However, this new vasculature is usually immature, chaotic, dysfunctional and structurally abnormal. As a consequence, tumours become hypoxic, with spatially and temporarily strongly varying oxygen deficiencies [4].

Recent efforts to improve radiotherapy outcome have focused on *in-vivo* assessment of tumour oxygenation. Non-invasive three-dimensional estimation of tumour hypoxia may be achieved by different imaging techniques such as positron emission tomography (PET) or magnetic resonance imaging (MRI). However, the quantitative assessment of the oxygen partial pressure based on these imaging techniques is not yet feasible. Microscopic variations at low and intermediate oxygen levels are key determinants of treatment success or failure, while the available imaging techniques provide only millimetre-resolution information on tumour oxygenation [8].

An alternative strategy to understand the radiation response of tumours is the mathematical modelling and computer simulation of the underlying biological processes. These models may consider different processes, such as tumour oxygenation, tumour growth or the generation of new tumour vasculature. Additionally, calculations may be performed on different spatiotemporal scales. These models allow considering a higher degree of complexity than calculations solely based on simple analytical models. In the context of tumour response, they may potentially serve as a tool to predict the radiation response of experimental *in-vivo* tumours. Regardless of the specific characteristics of a mathematical model, various challenges have to be addressed before implementing the model clinically. The complexity of a model is usually reflected in the number of parameters needed to perform the calculations. These parameters present sources of uncertainty and may limit the model's applicability. Additionally, comparison and validation against experimental pre-clinical data are necessary to prove the model's suitability for clinical application.

The objective of this thesis is to further improve and validate the tumour response model (TRM) developed by Espinoza *et al.* [9], [10]. The TRM is a multi-scale model that accounts for the oxygen impact on tumour response. Tumours are represented in a voxel-discretised space, where microscopic oxygen distributions are assigned voxel-wise in terms of oxygen histograms. Six biological processes are modelled in the TRM: Tumour cell proliferation, capillary cell proliferation, tumour growth, oxygen-dependent tumour cell kill, dead cell resorption and tumour shrinkage. The TRM simulates the spatiotemporal tumour response to a radiotherapy course and gives output on multiple scales: The number of tumour, capillary, dead and normal cells per voxel, the survival fraction of tumour cells per voxel, the spatiotemporal development of the tumour and the information whether the tumour is controlled or not.

The thesis firstly focuses on validating the TRM by analytical calculations by assessing the reliability and importance of the main radiobiological components of the model. The second and main objective is to adapt the TRM to predict the radiation response of preclinical *in-vivo* data of three rat prostate carcinoma sublines. These sublines differ in their degree of differentiation, growth rate and oxygenation status, and were irradiated with 1, 2, or 6 fractions in previous studies [11]–[14]. The parameter adjustment was performed by comparing the TRM-simulated and experimental dose-response curves for the three fractionation schemes.

2 Materials and methods

In this section, the bases of the physics of radiotherapy as well as of radiobiology are presented, to equip the reader with the tools to understand how tumours respond to radiotherapy, and how the response is measured and affected by the presence of oxygen. Next, the tumour response model (TRM) is explained, and further developments of the original model are described. Lastly, the experimental *in-vivo* data is presented and the adjustment strategy to fit the TRM input parameters to this data is described.

2.1 Background

2.1.1 Physics of radiotherapy

Radiation is considered ionising if it has enough energy to release electrons from atoms or molecules as the radiation travels through matter. Among the radiation qualities used for radiotherapy, charged particles such as electrons, protons, and carbon ions are considered as directly ionising radiation, whereas uncharged particles such as photons and neutrons are considered as indirectly ionising radiation [15]. While directly ionising radiation deposits its energy via collisions caused by the interaction of electromagnetic fields, indirectly ionising radiation releases its energy to the medium in two steps: energy is first transferred from the uncharged particles to charged particles and in a second stage, energy is deposited in the medium by these charged particles [16]. The most frequently used radiation type in radiotherapy are high-energy photons.

The number of photons in the primary beam is reduced by the interaction with the material. The decrease in the number of photons dN is proportional to the number of incident photons and the thickness of the absorber, N and dx respectively [15]. Taking μ as a proportionality constant, and considering the number of photons decreases as the absorber thickness increases, the following equation is obtained:

$$dN = -\mu N dx \quad (2.1)$$

Equation (2.1) can be written in terms of the photon beam intensity I , being proportional to the number of photons. If the thickness of the absorber x is considered as a length, μ is the linear attenuation coefficient, with units of cm^{-1} , and it follows:

$$\frac{dI}{I} = -\mu dx \quad (2.2)$$

The differential equation in (2.2) can be expressed in terms of the absorber's thickness x and the incident photon intensity I_0 , to obtain:

$$I(x) = I_0 e^{-\mu x} \quad (2.3)$$

The linear attenuation coefficient μ depends on the energy of the photons and the properties of the absorber material, such as its relative atomic mass and its density. To remove the dependency of μ on the absorber's density ρ , the mass attenuation coefficient μ/ρ is defined. For compound substances, μ/ρ can be calculated as the weighted sum of the different mass attenuation coefficients [17].

There are five major types of interactions contributing to photon beam attenuation by the material. For the photon energies commonly used in radiotherapy (< 10 MeV), attenuation by photodisintegration of a charged particle in the nucleus is considered to have a negligible contribution. Therefore, the four major interactions contributing to photon attenuation are coherent (Rayleigh) scattering, photoelectric effect, Compton effect, and pair production. Each of these interactions can be represented by a dedicated attenuation coefficient which depends, in different ways, on the photon energy and the absorber's properties. By adding up the individual coefficients, the total mass attenuation coefficient is obtained:

$$\frac{\mu}{\rho} = \frac{\sigma_{coh}}{\rho} + \frac{\tau}{\rho} + \frac{\sigma_C}{\rho} + \frac{\pi}{\rho} \quad (2.4)$$

In equation (2.4), σ_{coh} , τ , σ_C and π correspond to the attenuation coefficients for the interactions of coherent (Rayleigh) scattering, photoelectric effect, Compton effect, and pair production, respectively [15].

Rayleigh scattering

This interaction is also known by the name of "classical interaction" or "coherent scattering", and it occurs between a photon and an absorber atom. The photon is scattered by bound atomic electrons, while the atom is neither ionised nor excited. The transferred momentum is absorbed by the entire atom, with very small recoil energy. The photon is scattered at a relatively small angle with essentially the same initial energy. This interaction occurs predominantly at high atomic number Z of the absorber and low photon energies $h\nu$ [16], and it has minor importance in the context of radiotherapy [15]. Rayleigh scattering does not contribute to energy absorption and therefore to the deposited dose.

Photoelectric effect

During this interaction, an incoming photon is absorbed by an atom and as a result, an atomic electron is ejected. The kinetic energy of the ejected electron is the difference between the incoming photon's energy and the electron's binding energy. Once the electron is ejected, a vacancy in the atom's shell is created. This vacancy can be filled by an outer electron, resulting in the emission of a characteristic x-ray. Since the K-shell binding energy for soft tissues is approximately 0.5 keV, the energy of characteristic photons is very low and considered to be locally absorbed. The cross section of the photoelectric effect depends on the absorber's atomic number and the photon energy, $\tau/\rho \propto Z^3/E^3$ [15]-[17].

Compton effect

In the Compton effect, also known as incoherent scattering, a photon interacts with a loosely bound electron, considered to be "free" since the energy of the photon is considerably larger than the electron's binding energy. As a result, the photon transfers energy to the electron and is scattered, with reduced energy, at an angle Φ . On the other hand, the electron is emitted from the atom at an angle θ . The cross section of the Compton effect in water-like tissues increases with photon energy until approximately 1 MeV and decreases for further photon energy increment. Taking into account that Compton interactions occur mainly with "free" electrons, the cross-section does not depend on the absorber's atomic number. Instead, the Compton mass attenuation coefficient σ_c/ρ depends on the electron density [15], [16], [18].

Pair production

A pair production, the creation of an electron-positron pair, is possible when the energy of the incident photon exceeds $2m_e c^2 = 1.02$ MeV, where $m_e c^2$ is the rest energy of the electron. In this process, the photon interacts with the strong electromagnetic field close to the nucleus and is converted into an electron-positron pair. In the case the photon's energy exceeds $2m_e c^2$, the exceeding energy is shared between the electron-positron pair as kinetic energy. Annihilation radiation occurs when the positron has travelled through the absorber and lost most of its kinetic energy. The slowly travelling positron combines with an electron in the neighbourhood and two annihilation photons arise. These annihilation photons have an energy of 0.51 MeV each and due to momentum conservation, they are ejected in opposite directions [15], [16]. The cross section of occurrence for pair production is zero for photon energy below the $2m_e c^2$ threshold, and increases swiftly with $h\nu$ beyond this threshold. For energies above 20 MeV, the cross-section is approximately proportional to Z^2 .

Total mass attenuation coefficient

The contributions of the previously mentioned interactions to the total mass attenuation coefficient in water are shown in Figure 2.1. For the photon energies used in radiotherapy (1-15 MeV), the major contribution in water-like soft biological tissues is from the Compton effect.

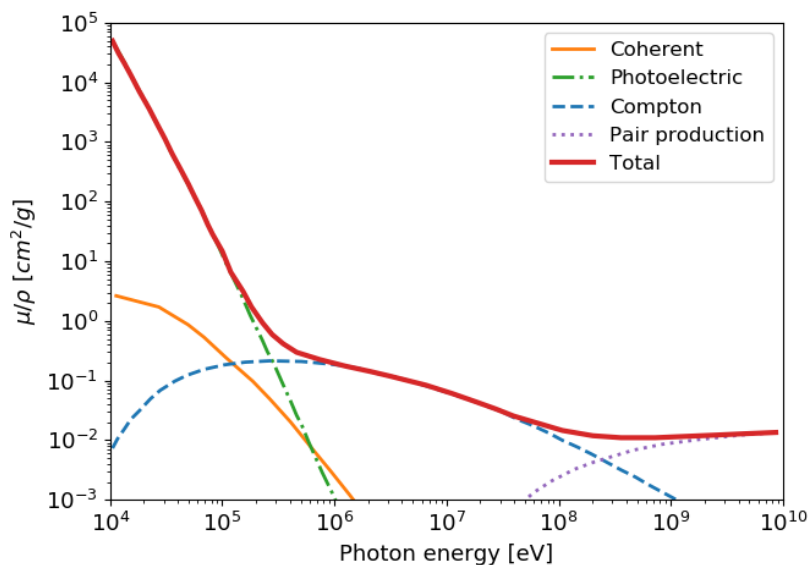


Figure 2.1: Total mass attenuation coefficient μ/ρ as a function of the photon energy for water, with the separate contributions from coherent (Rayleigh) interaction, photoelectric effect, Compton effect, and pair production. Adapted with permission of IOP Publishing from [18].

Absorbed dose

In the context of radiotherapy, the energy deposited in the absorbing material, *i.e.* the biological tissue, is the most relevant quantity. The total absorbed energy is described by the respective mass attenuation coefficients of the underlying interaction processes. The absorbed dose D is then defined as the quotient of the mean energy imparted $d\bar{\epsilon}$ by ionising radiation to the material of mass dm : $D = d\bar{\epsilon}/dm$. D is usually measured in units of Gray, denoted as Gy, where $1 \text{ Gy} = 1 \text{ J/kg}$. While the absorbed dose is related to the biological effect, this relationship is not simple and therefore specialised disciplines, such as radiobiology, are needed to understand how the absorbed dose relates to biological effect [15], [16].

2.1.2 Radiobiology

Radiobiology focuses on understanding, experimentally and theoretically, the events that follow the irradiation of biological systems. In the case of photon radiotherapy, secondary electrons generated by incident photons release the energy in the tissue. Therefore, these electrons are the major contributor to the biological damage imparted to the tissue exposed to radiation. The first series of events post-irradiation occur during the physical phase, where the secondary electrons

traverse the tissue in $10^{-18} - 10^{-12}$ seconds. During the following chemical phase, chemical changes occur in the molecules ionised by the electrons, which result in molecular damage. In most cases, molecules can be repaired or replaced, when various copies are available in the cell, and in those cases, the survival of the cell is not jeopardised. However, there are only two copies of the largest and most important molecule in the cell: The deoxyribonucleic acid (DNA). Damage to the DNA can be permanent, leading to mutations or cell death. Subsequent reactions after the chemical phase, for both healthy and tumour tissue, can appear from seconds to years after irradiation. This last phase is referred to as the biological phase, and it is characterised by early loss of cells, compensatory cell proliferation and in some cases the appearance of secondary tumours [19].

The structure, size and function of healthy tissue are determined by stem cells, with the unlimited capability of proliferation. Tumours are driven by cancer stem cells, which constitute the tumour tissue by generating additional stem cells, as well as well-differentiated non-malignant cells. When cancer stem cells can form a cell colony they are called clonogenic cells. Clonogenic cells drive tumour growth and therefore radiotherapy aims to prevent these cells from further proliferation [17].

Linear Quadratic Model

Clonogenic assays are essential to study the radiation response of cancer cells. These assays are performed by placing cells in a defined growth environment to then assess their colony-forming ability after irradiation. Cell kill is determined as the complement to the survival fraction (SF), which is the fraction of surviving relative to the irradiated cells:

$$SF = \frac{\# \text{ surviving cells}}{\# \text{ irradiated cells}} \quad (2.5)$$

The SF for a given cell line depends on the dose and its temporal delivery pattern, *i.e.* the dose fractionation. It is of radiobiological interest to describe the relationship between cell survival, dose and dose fractionation, to provide a common framework for comparing and analysing data, and in the long term to build a consistent theory of this particular phenomenon [19]. Various descriptive models have been developed in the past decades to describe the SF as a function of dose. To describe the combined dependence of the SF on the dose and fractionation for different cell lines, the Linear Quadratic Model (LQM) is used [20].

The LQM results from the fit of a second-order polynomial to the cell survival curves (Figure 2.2), with a zero constant term to obtain $SF = 1$ at zero doses. The LQM is a key tool in radiobiology

and radiation physics since it provides a simple relation between dose and cell survival [21]. The basic formulation of the LQM describes the cell SF after exposure to a single radiation dose D as:

$$SF = e^{-\alpha D - \beta D^2} \quad (2.6)$$

where the fitting parameters α and β , measured in Gy^{-1} and Gy^{-2} respectively, describe the cell's sensitivity to radiation. Radiotherapy is usually delivered in multiple radiation doses, in what is called a fractionated treatment, consisting of n irradiations, each delivering a fraction dose d for a total dose of $D = nd$. As a result of each radiation fraction, a cell may either die or survive with or without sublethal damage. Assuming irradiated cells are given enough time to recover after each fraction (6-24 hours), all sublethal damage would be repaired and the cells would respond to the following fraction as if they have not been previously irradiated [19], [21]. Under this assumption, the cell SF after n fractions of dose d is:

$$SF = (e^{-\alpha d - \beta d^2})^n = e^{-n(\alpha d + \beta d^2)} = e^{-D(\alpha + \beta d)} \quad (2.7)$$

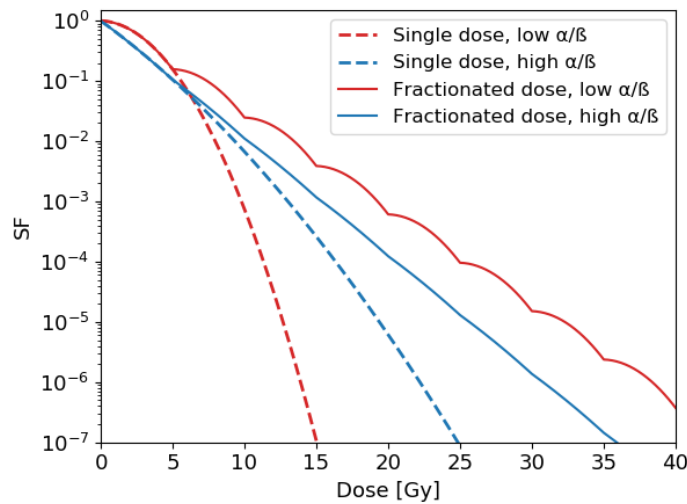


Figure 2.2: SF curves for single (dashed lines) and fractionated irradiations (continuous lines), for low and high α/β values (red and blue lines, respectively). Note that a given SF, for example 10^{-5} , is achieved at a different dose level for each irradiation schedule. The dose difference between the dashed and continuous lines of the same colour at a given survival level indicates how sensitive a cell line, with a given α/β , is to changes in fractionation.

The ratio α/β , with units of Gy, is used to describe the curvature of the SF as a function of the dose shown in Figure 2.2. Acute-responding tissues express biological damage days or weeks after radiation exposure and are characterised by α/β values ranging from 7 to 20 Gy. On the contrary, late-responding tissues express biological damage months or even years after irradiation, with α/β values between 0.6 and 6 Gy. The response to fractionated treatments of most well-oxygenated tumours is similar to that of acute-responding tissues, in some cases reporting even higher values of α/β . As shown in Figure 2.2, the SF of cells with low α/β , with more pronounced curvature, is more sensitive to dose fractionation than for cells with high α/β . Therefore, the

rationale behind fractionated treatments is the sparing of late-responding normal tissues, while treating the tumour [19].

It is possible to provide a mechanistic interpretation of the LQM. For example, α is thought to be related to the lethal damage (damage that cannot be repaired by the cell and leads to cell death) produced by a single hit, and therefore proportional to d . On the other hand, β is related to the combination of two independent single hits, proportional to d^2 [22]. There are other interpretations, related either to the cell repair process [23], the creation of potentially lethal damages [24], or the repair rate saturation [25]. However, it is important to note there are many factors affecting cell death following irradiation. Some of these factors are related to the density and type of cell damage caused by radiation, the repair mechanisms available in the cell, the cell cycle phase during irradiation, and the cell death pathways, among others. Therefore, the LQM with its fitting parameters is often considered as a phenomenological description of the resulting cell survival.

Besides the dependence on the cell-specific characteristics, cell death depends on the various additional treatment and biological factors, such as the radiation quality and microenvironmental conditions. One of the first radiation response-modifying factors identified was oxygen. Low oxygen levels in tumours are associated with increased radioresistance and therefore poor radiotherapy outcome [21].

Impact of oxygen on the radiation response

Advanced tumours usually develop areas with poor oxygenation, mainly due to the imbalance between vasculature growth and tumour nutrient consumption. New vasculature in tumours is created by a process called angiogenesis. However, rapidly-growing tumours usually outpace the vascular development, resulting in functional and structural abnormalities of the tumour vasculature, altered vascular geometry, and local anaemia, leading to reduced oxygen availability. Hypoxia refers to low oxygen concentration and is generally classified into two categories: Chronic or diffusion-limited hypoxia which is caused by decreased oxygen concentration at large distances from the vessel ($> 70\mu\text{m}$) due to large inter-vessel distances, and acute or perfusion-limited hypoxia, which takes place when the oxygen concentration varies over short intervals of time (minutes to hours) due to perfusion changes [5], [19]. Both types of hypoxia are illustrated in Figure 2.3.

Hypoxia is characterised as being heterogeneous in various aspects. Hypoxia occurs not only at zero oxygen concentrations but also at higher concentrations. These concentrations can vary spatially as well, with tumour regions showing high oxygen concentrations and others showing hypoxia. Additionally, hypoxia can vary over short periods, or may be stable in time. In the context

of radiotherapy, it is important to note that hypoxia is also markedly different among patients, and therefore personalised approaches are necessary to successfully treat cancer [19], [26].

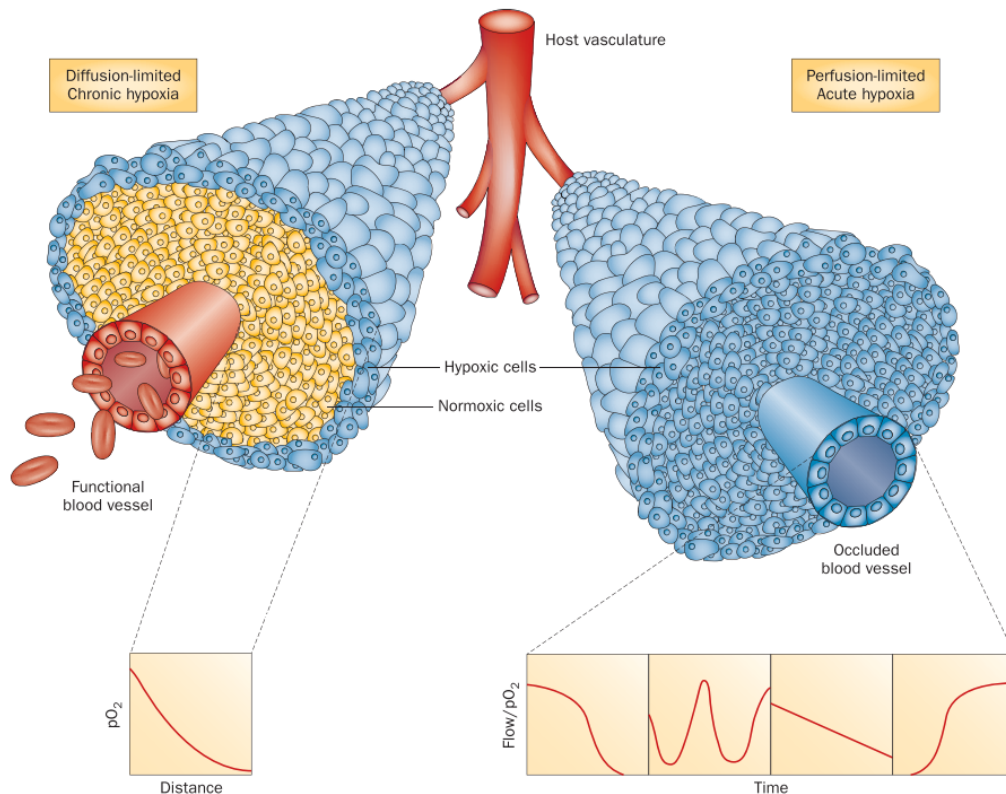


Figure 2.3: Illustration of the two different types of hypoxia. Chronic or diffusion-limited hypoxia (left) is caused by large inter-vessel distances, leading to chronically hypoxic cells at large distances from the vessel. Acute or perfusion-limited hypoxia is caused by the variation of oxygen concentration due to perfusion changes in the vessel over time, causing surrounding cells to become temporarily hypoxic. Reprinted with permission of Springer Nature and Elsevier, from [4] and [27], respectively.

The relation between oxygen concentration and cell sensitivity to radiation was first reported in 1955 by Gray [28]. Nowadays, the negative impact of hypoxia on the radiotherapy outcome has been further studied and continues to be a topic of research [4], [19], [26], [29]–[31]. Different approaches have been established to target hypoxia-induced radioresistance, ranging from cell sensitisers to radiation boost to hypoxic tumour regions [32]–[34]. Additional efforts include modelling and simulation of the radiation response of hypoxic tumours, a topic which will be covered in further detail later in this thesis.

Oxygen as a dose-modifying factor

The impact of oxygen on radiation response has been studied using clonogenic assays. The cell SF decreases more rapidly when oxygen is present, which in the context of radiotherapy means that more tumour cells are killed by radiation when oxygen is available. This enhanced damage caused

by oxygen is equivalent to an increased delivered dose. This increase is given by a factor termed oxygen enhancement ratio (OER), which is approximately the same at all survival levels. The OER is calculated as:

$$\text{OER} = \frac{\text{Dose}_{\text{hypoxia}}}{\text{Dose}_{\text{air}}} \Bigg|_{\text{same biological effect}} \quad (2.8)$$

For most cells exposed to photon irradiation *in-vitro*, the OER has a value of around 3. Expressing the oxygen concentration as the partial pressure of the gas pO_2 , the OER is parameterised as follows:

$$\text{OER}(pO_2) = \frac{m \cdot pO_2 + k}{pO_2 + k} \quad (2.9)$$

In equation (2.9), m is the maximum OER and k is the pO_2 at which the OER equals half of its range [35]. The OER as a function of pO_2 is shown in Figure 2.4, where the rapid variation of OER occurring at intermediate pO_2 levels can be seen.

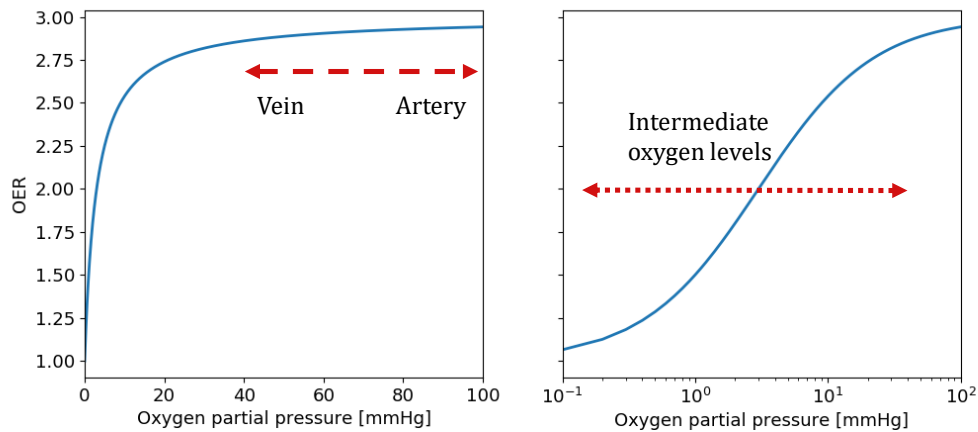


Figure 2.4: OER as a function of pO_2 . The oxygen partial pressure ranges between zero and 100mmHg, covering the pO_2 of veins and arteries (left). At intermediate and low pO_2 , as found in tumours, the OER decreases. For better visualisation, the curve is additionally shown on a logarithmic scale (right).

The dose-modifying effect of oxygen is currently explained by the so-called oxygen fixation hypothesis, as illustrated in Figure 2.5. Under this hypothesis, the secondary electrons generated by a photon beam ionise water molecules in the cell, creating free radicals. These free radicals quickly attach to the DNA, resulting in radiation damage that can be repaired by different cell repair mechanisms. However, in the presence of oxygen, additional radical reactions lead to a fixation of the radiation damage, making repair less likely.

The OER can be used to extend the LQM, resulting in a mathematical formula that considers the oxygen level and its impact on cell survival after irradiation:

$$\text{SF(OER)} = \exp \left[-\frac{\alpha}{m} D \cdot \text{OER}(pO_2) - \frac{\beta}{m^2} D^2 \cdot \text{OER}^2(pO_2) \right] \quad (2.10)$$

In equation (2.10), the OER as parameterised in equation (2.9) is inserted into the LQM formulation from equation (2.6), and α and β refer to completely oxygenated conditions. Since m is the maximum OER, and the $\text{OER}(pO_2)$ varies from 1 to m , the SF under hypoxic conditions is always larger than under well-oxygenated conditions, as shown in Figure 2.6.

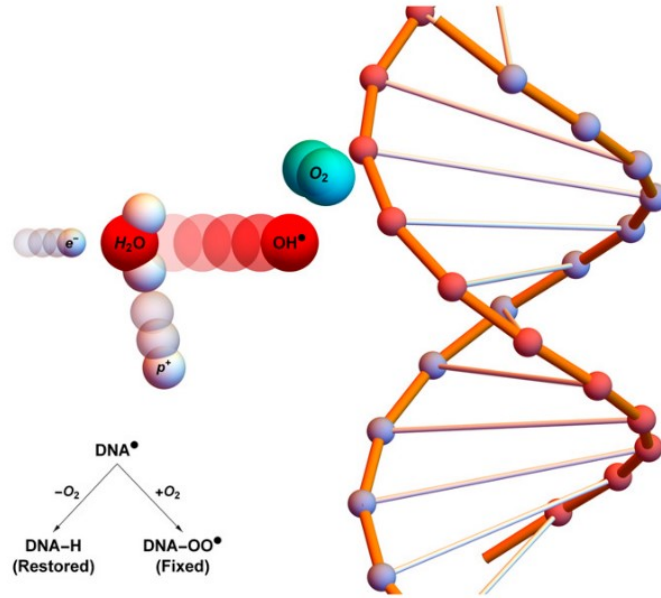


Figure 2.5: The oxygen fixation hypothesis is the currently accepted mechanism underlying the dose-modifying effect of oxygen in radiotherapy. In the presence of oxygen, the radical $-OO^*$ is created by secondary electrons, and it binds to the DNA, fixing the radiation damage, making repair less likely. Reprinted from [36] under the terms of the Creative Commons Attribution 3.0 licence.

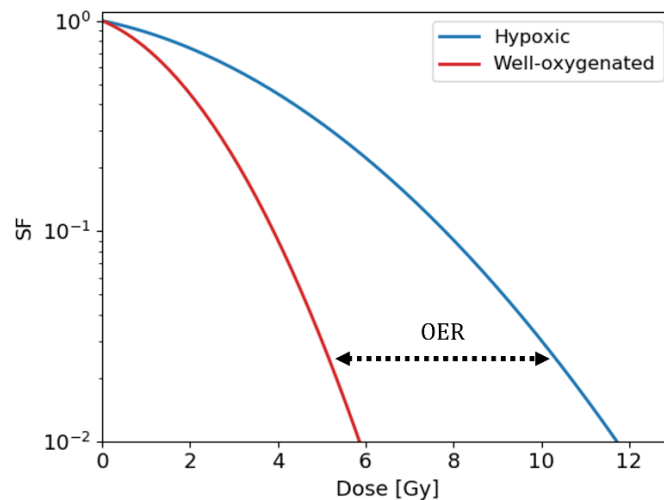


Figure 2.6: Example of SF curves for well-oxygenated and hypoxic conditions for a given clonogenic assay, as calculated with equation (2.10), for α and β referring to the same well-oxygenated condition and for $\text{OER}(pO_2) = 1.5$. A given SF is achieved at lower doses for the well-oxygenated condition than for the hypoxic one.

Dependence of the fractionation effect on the tumour oxygenation

Based on equation (2.10), the OER may also be thought to modify the effective tumour radiosensitivity rather than the dose. If the tumour is completely hypoxic (OER = 1, see equation (2.9) and Figure 2.4), the effective radiosensitivity parameters are: $\alpha_{eff} = \alpha/m$ and $\beta_{eff} = \beta/m^2$, where α and β refer to completely oxygenated conditions. For any other tumour oxygenation, the effective radiosensitivity parameters are given by $\alpha_{eff} = \alpha \cdot \text{OER}(pO_2)/m$ and $\beta_{eff} = \beta \cdot \text{OER}^2(pO_2)/m^2$, and it follows that the effective α/β is given by the expression:

$$\left(\frac{\alpha}{\beta}\right)_{eff} = \frac{\alpha_{eff}}{\beta_{eff}} = \frac{\alpha}{\beta} \cdot \frac{m}{\text{OER}(pO_2)} \quad (2.11)$$

The parameter α/β_{eff} describes the effective fractionation effect observed for tumours of a given oxygenation condition, and due to the asymptotic behaviour of $\text{OER}(pO_2)$, it follows that $\alpha/\beta_{eff} > \alpha/\beta$ for all pO_2 values. Taking into account that m is constant, the α/β_{eff} depends only on α/β and $\text{OER}(pO_2)$. Therefore, a higher fractionation effect, as illustrated in Figure 2.2, may be achieved by decreasing α/β or increasing $\text{OER}(pO_2)$.

Dose-response curves

Radiobiology focuses on studying the biological response caused by radiation, and the factors influencing this response. Specifically, it is relevant to know the relationship between dose and local tumour control probability (TCP), where a tumour is considered as being locally controlled if all clonogenic tumour cells are sterilised by the radiation. The TCP approaches zero at low doses and tends to 100% at very high doses. The intermediate region of this dose-response curve is of particular interest, and its sigmoid shape, as shown in Figure 2.7, may be described by different statistical models. Considering that the killing of clonogenic tumour cells with radiation is a stochastic event, the TCP can be described using a Poisson distribution, which depends on the average SF and the initial number of cells. If the SF is defined by the LQM, the TCP is given by:

$$\text{TCP}(D) = \exp(-N_0 \cdot \text{SF}(D)) = \exp[-N_0 \exp(-\alpha D - \beta D^2)] \quad (2.12)$$

Empirically, TCP curves may be estimated if incidence rates, defined as the ratio of the number of locally controlled and irradiated tumours, are available at different dose levels. In this case, the logistic dose-response model may be fitted [19], [37]:

$$\text{TCP}(D) = \frac{\exp(b_0 + b_1 D)}{1 + \exp(b_0 + b_1 D)} \quad (2.13)$$

In equation (2.13), the logarithm of the probability has been expanded to the first term, resulting in two fitting parameters for the TCP, b_0 and b_1 , estimated via maximum likelihood regression. These fitting parameters can be used to calculate D_{50} , the dose leading to a TCP of 50%:

$$D_{50} = -\frac{b_0}{b_1} \quad (2.14)$$

which is used to specify the position of the TCP curve [11], [19]. Additionally, the TCP slope may also be calculated as the derivative of TCP(D) at D_{50} , depending only on b_1 , as shown in equation (2.15):

$$\text{TCP}'(D = D_{50}) = \frac{b_1}{4} \quad (2.15)$$

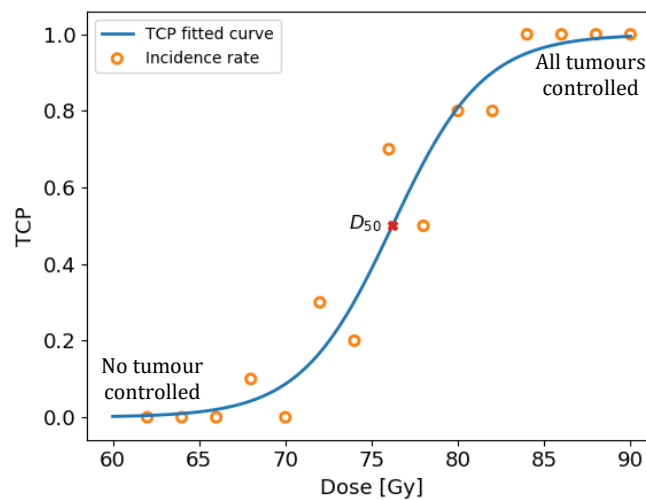


Figure 2.7: Example of a TCP curve with D_{50} indicated. The TCP curve is fitted to the experimentally obtained tumour control rates (incidence rates), calculated as the ratio of the number of locally controlled and irradiated tumours at different dose levels. For small doses, no tumour is controlled, whereas for large doses all tumours are controlled.

The 5 R's of Radiotherapy

There is a variety of factors influencing the tumour response and thus the tumour control after radiotherapy. After decades of radiobiology research, the following influence factors have been identified and are often referred to as the “5 R's of Radiotherapy” [19]:

- Radiosensitivity: Each cell population and tumour type has an intrinsic radiosensitivity.
- Recovery of sublethal damage: There are various repair mechanisms available in the cell to deal with sublethal radiation damages.

- Cell-cycle redistribution: Cell radiosensitivity varies over the cell cycle. After delivering some radiation fractions, the surviving cells are synchronised in the most resistant phases of the cell cycle.
- Repopulation: Remaining cancer stem cells can repopulate the tumour after radiotherapy, in some cases at an increased pace.
- Reoxygenation: Hypoxia in the tumour may diminish during the treatment, due to the increased oxygen availability after killing well-oxygenated cells.

Nowadays, an increasing number of malignant tumour types are treated with hypofractionation, which includes a low number of high-dose fractions. At high doses (> 8Gy), there are some indications of additional factors influencing the tumour response to radiotherapy, such as damage to the blood capillaries, enhanced immune stimulation, and decreased impact of hypoxia on the tumour response. Even in this scenario, there is evidence suggesting that the cell SF is still accurately modelled by the LQM [38].

Modelling of tumour response to radiotherapy

Radiotherapy aims to treat tumours with sufficiently high radiation doses while sparing the surrounding healthy tissue. The tumour response to radiation depends on many factors, making it challenging to objectively choose the best treatment course for each patient. Computational models provide a tool to improve the understanding of the biological processes involved in radiation response, as well as to assess different treatment scenarios during treatment planning. There are plenty of approaches to the modelling of tumour response, varying in the spatial scale, the considered biological processes and the way the response is quantified [39]. This thesis is based on the tumour response model developed by Espinoza *et al.* [9], [10]. This model is appealing for its implementation of the LQM along with the consideration of the most relevant biological processes in the tumour response to radiation. Additionally, it allows accounting for microscopic variations of oxygen while providing the macroscopic evolution of the tumour in the course of radiotherapy. In the following section, the tumour response model as developed by Espinoza *et al.* is summarised.

2.2 Tumour response model (TRM)

The tumour response model (TRM) is a mathematical model to simulate the response of a discretised tumour volume to radiation, depending on the oxygenation of the tumour cells in the volume, as well as on other relevant biological processes. As a result, the spatiotemporal development of a single tumour is obtained. The TRM together with the tumour oxygenation

model, as implemented by Espinoza *et al.* [9], [10], along with its components is explained in this section.

2.2.1 Model structure

The TRM considers a voxel-based volume, where each voxel may contain four different types of cells: Viable tumour cells (TC), dead tumour cells (DC), capillary cells (CC), and normal cells (NC). The absolute number of cells N_C is given by the sum of all cell types:

$$N_C = N_{TC} + N_{DC} + N_{CC} + N_{NC} \quad (2.16)$$

At the beginning of the simulation, the volume is spatially and biologically characterised, and information about the radiation treatment, such as total dose and dose per fraction, is provided. Additionally, information about the tumour oxygenation for each voxel is given in terms of oxygen histograms, which specify the fraction of TCs at given oxygen levels.

There are six main biological processes considered in the TRM: Proliferation of TCs, proliferation of CCs (angiogenesis), tumour growth, radiation-induced cell kill, DC resorption, and tumour shrinkage. The information about tumour oxygenation impacts two of the six functions: Angiogenesis, where CCs proliferate only under hypoxic conditions, and the radiation response, where the SF is calculated with the OER-modified LQM formulation, given by equation (2.10). Once the TRM simulation starts, these six functions are repeatedly executed in a loop, until the tumour is either controlled or all dose fractions are delivered. This TRM loop is illustrated in Figure 2.8, including the influence of tumour oxygenation.

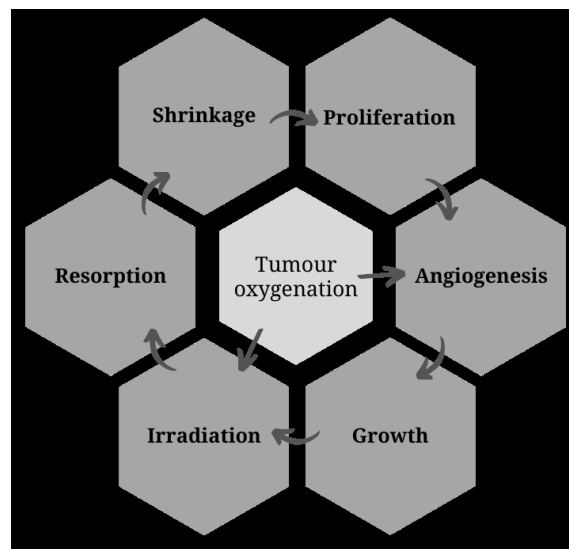


Figure 2.8: TRM loop consisting of six main functions that are repeatedly executed. Only angiogenesis and radiation-induced cell-kill depend on tumour oxygenation.

At the beginning of the simulation, the tumour volume is characterised. During the simulation, information about the tumour oxygenation and the treatment is used. The resulting spatiotemporal tumour development provides information about the number of all cell types in the volume over the entire simulation time, from which the SF and the status of the tumour control (Y/N) are obtained. A tumour is considered as being controlled only if no tumour cell survived. The TRM simulation of one single tumour is illustrated in Figure 2.9.

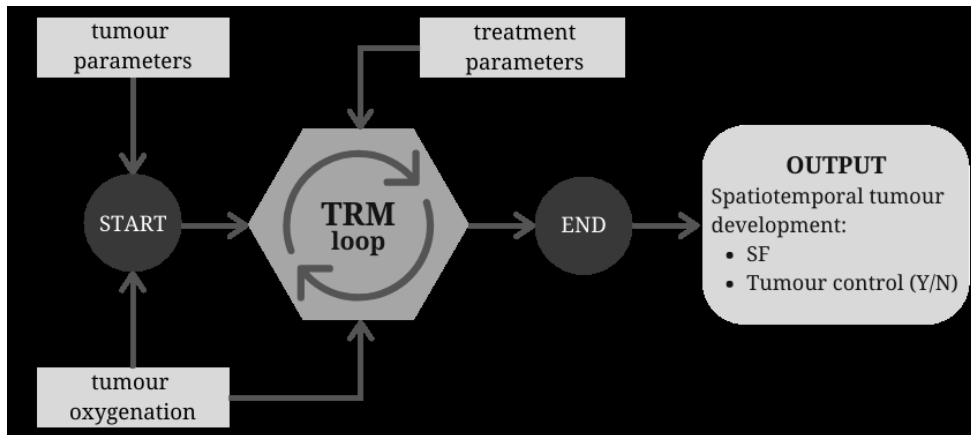


Figure 2.9: Flowchart of the TRM simulation for a single tumour. The tumour is controlled (Y) if all TCs were killed by the end of the simulation. If several tumours are simulated at different dose levels, TCP curves can additionally be calculated, as described in section 2.1.2.

2.2.2 Initial characterization of the tissue

The TRM considers four different types of data for the initial characterisation:

- **Anatomical characterisation:** Specification of the shape and tissue type, which may be tumour, normal soft tissue, bone, or air. A fixed total cell density is assigned to the entire volume, while the TC and CC densities can be specified for every single voxel. In this study, this information is generated manually. However, the TRM also supports processed input data from medical imaging such as computed tomography (CT), positron emission tomography (PET) or magnetic resonance imaging (MRI).
- **Hypoxic status:** Information about the tumour oxygenation is provided for each tumour voxel in terms of oxygen histograms. Currently, these histograms are generated before the TRM simulation using the tumour oxygenation model [40], explained in further detail in section 2.2.3. According to the vascular fraction (VF, fraction of the voxel volume occupied by CCs) and the dead fraction (DF, fraction of the voxel volume occupied by DCs, which do not consume oxygen), an oxygen histogram is selected. Cell kill and angiogenesis depend on the tumour oxygenation given by the oxygen histogram.
- **Tumour development:** Specification of the parameters related to all the biological processes considered in the TRM, as shown in Figure 2.8 and explained in section 2.2.4.

- Treatment parameters: Information about the radiation dose delivery, such as dose per fraction, number of fractions, the time between fractions and eventually additional breaks (for example, during the weekend). Additionally, the spatial dose distribution is specified.

Preparation of the input data

The initial characterisation of the tissue within the TRM in the version of Espinoza *et al.* [9], [10], later modified by Mang [41], is performed according to the following specifications [42]:

- Anatomical characterisation: Provided in the file format NRRD, with all files having the same voxel size and domain dimensions. N_C is calculated as the ratio of the cell density, ρ_C , and the voxel volume, v : $N_C = \rho_C \cdot v$.

- N_{TC} is coded on a logarithmic scale, where the image value I_{TC} is given by:

$$I_{TC} = 100 \cdot \log_{10}(N_{TC}) \quad (2.17)$$

If $N_{TC} = 0$, the NRRD image value is coded as $I_{TC} = -1$.

- The VF is coded with the image value I_{CC} as follows:

$$I_{CC} = 10^3 + 10^4 \cdot VF \quad (2.18)$$

For example, a VF of 0.035 has an image value of 1350. Then, $N_{CC} = N_C \cdot VF$.

- DCs are assumed to be zero at the beginning of the simulation.
- N_{NC} is calculated as $N_{NC} = N_C - N_{TC} - N_{CC}$.
- Air and bony structures are given as two separate binary images, where the image value 1 corresponds to air or bone, respectively. Soft tissue (non-bone and non-air structures) has an image value of zero. A voxel cannot be air and bone at the same time.
- Hypoxic status: Oxygen histograms are provided as text files, one file per DF, with VF ranging from 0.001 to 0.20.
- Tumour development: The parameters associated with the different biological processes considered in the TRM (section 2.2.4) are provided in a text file.
- Treatment parameters: Information about the number of fractions and time between fractions is provided in the text file previously mentioned. The dose distribution is provided in a NRRD file, where the image value is the dose per fraction in units of Gy.

2.2.3 Tumour oxygenation model (TOM)

Oxygen is assumed to diffuse from capillaries into the tissue, where it is consumed by the cells. This process can be modelled by a diffusion-reaction partial differential equation [43]–[46]:

$$\frac{\partial pO_2}{\partial t} = D_{O_2} \nabla^2 pO_2 - g_{max} \frac{pO_2}{pO_2 + k} \quad (2.19)$$

where pO_2 is the spatiotemporal distribution of oxygen, D_{O_2} is the oxygen diffusion coefficient, g_{max} is the maximum consumption rate and k is the Michaelis-Menten coefficient of oxygen consumption. For short time scales, equation (2.19) can be considered as stationary, *i.e.* $\partial pO_2 / \partial t \cong 0$. Equation (2.19) can be solved through different numerical methods [46]–[49].

The tumour oxygenation model (TOM) was developed by Espinoza *et al.* [9], [46] to calculate the spatiotemporal distribution of oxygen. The TOM originally solved equation (2.19) in a 1 mm^3 cubic tumour volume with a given vascular architecture using the particle strength exchange method. Later, the TOM was adapted and modified by A. Neuholz [47], and currently, the calculation is performed using the finite difference method.

Using a vascular architecture of randomly distributed parallel linear vessels in 3D, each of $20 \text{ }\mu\text{m}$ diameter, the 3D oxygen distribution is calculated with TOM for different VF and DF. These distributions are condensed in a database of oxygen histograms. The main factors influencing the shape of the oxygen histogram are the VF and DF: The VF is determined by the volume occupied by vessels, where increased VF leads to a higher number of vessels and subsequently to a better oxygenated histogram. As DCs are assumed not to consume oxygen, the available oxygen increases with decreasing DF. This is achieved by decreasing the consumption rate g_{max} in the same proportion as the DF increases, in steps of 10% at a time. Hence, the database provides histograms with different combinations of VF and DF to cover all possible scenarios. For this thesis, the impact of the DF on the oxygen histogram selection is referred to as “DF influence”. Examples of the vascular architecture and the oxygen histograms are shown in Figure 2.10.

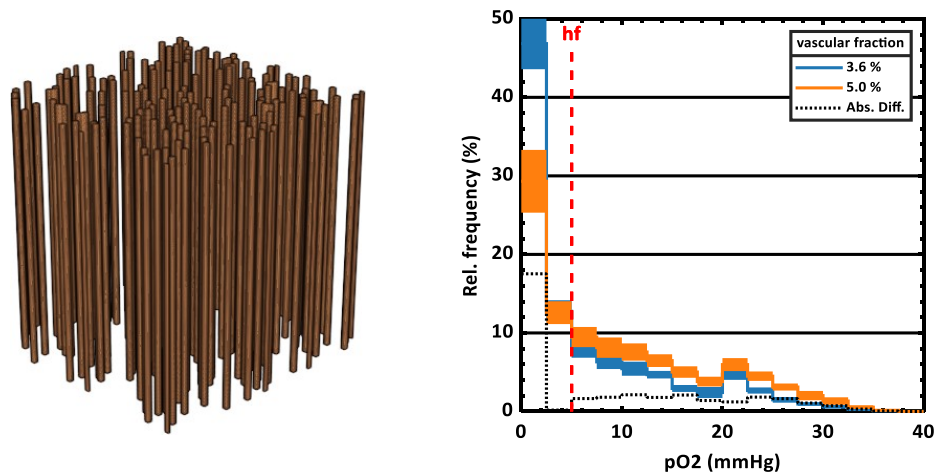


Figure 2.10: Example of parallel linear vessels of $20 \text{ }\mu\text{m}$ diameter in a 1 mm^3 cube, considered for the simulations with the TOM (left) and oxygen histograms for VF 3.6% and 5.0% (right). The HF corresponds to the sum of the two leftmost oxygen bins ($pO_2 < 5 \text{ mmHg}$). Images courtesy of A. Neuholz [47].

At the beginning of the TRM simulation, an oxygen histogram is selected from the database for each voxel, according to its VF and DF. The different biological processes considered in the TRM, such as the oxygen-dependent cell kill, angiogenesis and cell redistribution between voxels, modify the VF and DF after each iteration and thus also the shape of the histograms for each voxel. At the beginning of the next iteration, a new oxygen histogram is selected from the database, based on the updated VF and DF. The parameter values used by A. Neuholz to obtain the oxygen histogram database are summarised in Table 2.1.

Table 2.1: Parameters used for simulations with the TOM to obtain the oxygen histogram database used for the TRM simulations.

Parameter	Symbol	Value
Diffusion coefficient of molecular oxygen at 37 °C	D_{O_2}	$2 \cdot 10^{-9} \text{ m}^2/\text{s}$ [50], [51]
Maximum oxygen consumption rate in the tissue	g_{max}	15 mmHg/s [43], [50], [52]
pO_2 at the half-maximum consumption rate	k	2.5 mmHg [43], [50], [52]

2.2.4 Biological processes in the TRM

The TRM in the version of Espinoza [9], [10] considers six biological processes in the simulation of the tumour response to radiotherapy, as shown in Figure 2.8:

1. Tumour cell proliferation

Experimentally, the tumour volume increases exponentially with time. However, above a certain volume, the growth rate decreases as nutrients and oxygen become scarce and the growth curve begins to saturate. This growth behaviour is described by the Gompertz equation:

$$V = V_0 \exp \left[\frac{A}{B} (1 - e^{-Bt}) \right] \quad (2.20)$$

where V is the volume, V_0 is an arbitrary initial volume, t is the time, and A and B determine the growth rate. Experimental data may be used to fit equation (2.20) and to obtain the volume doubling time (VDT, time required for the tumour to double its volume): $VDT = \ln(2) / A$. For short times as used in the TRM, the TC proliferation is modelled by a purely exponential function of time, leading to the proliferation factor PF [19]:

$$PF = \exp \left(\frac{\ln(2)}{VDT} \cdot t \right) \quad (2.21)$$

2. Angiogenesis

The proliferation of CCs is modelled similarly to TC. However, as angiogenesis takes place only under hypoxic conditions, the oxygen histogram is additionally taken into account. In the TRM, angiogenesis is only considered in proportion to the hypoxic fraction (HF, the fraction of the volume with less than 5mmHg of oxygen pressure, as given by the voxel's oxygen histogram). Otherwise, the proliferation factor for capillary cells PF_{angio} [9], [10] is defined analogue to equation (2.21):

$$PF_{\text{angio}} = \exp\left(\frac{\ln(2)}{VDT_{\text{angio}}} \cdot t\right) \quad (2.22)$$

3. Tumour growth

The proliferation of TCs and CCs leads to an overall increase in the total cell density. Once a density threshold of 10% above the initial cell density is exceeded, tumour growth occurs. In this case, cells are exchanged with neighbouring voxels with lower cell density, proportionally to the absolute difference in cell number and inversely proportional to the distance between voxels. All cell types are distributed in this manner until all voxels fall again below the given density threshold. The tumour is allowed to invade air and normal tissue but not bone [9], [10].

4. Radiation-induced cell kill

Initially, the frequency of oxygen levels of the TCs is assumed to be distributed according to the corresponding oxygen histogram (see Figure 2.10). The number of surviving TCs per bin of the oxygen histogram is then calculated, according to the LQM-OER equation (2.10).

To reflect the variation of tumour radiosensitivity among tumours of different patients [53], [54], an additional parameter σ_α , introduces inter-tumour variability to the TRM, which allows the sampling of the LQM parameters. Initially, α_0 , β_0 , and σ_α are specified, and before the simulation of an individual tumour starts, α is sampled based on a probability distribution defined by α_0 and σ_α . Originally, a normal distribution was used, with mean α_0 and standard deviation σ_α . For this thesis, the normal distribution has been replaced by a lognormal distribution, to ensure $\alpha > 0$ for all values of σ_α and α_0 , since the radiosensitivity given by the LQM parameters is always positive. For $\sigma_\alpha \ll \alpha_0$, the lognormal distribution in equation (2.23) approximates to a normal distribution.

$$\text{Lognormal}(\mu, \sigma^2) = \frac{1}{x\sigma\sqrt{2\pi}} \cdot \exp\left[-\frac{(\ln x - \mu)^2}{2\sigma^2}\right] \quad (2.23)$$

$$\mu = \ln\left(\frac{\alpha_0}{\sqrt{1 + \sigma_a^2/\alpha_0^2}}\right) ; \quad \sigma = \sqrt{\ln\left(\frac{\sigma_a^2}{\alpha_0^2} + 1\right)}$$

Once α is determined, β is calculated assuming a fixed α_0/β_0 ratio.

The calculation of the number of surviving TCs is performed in two different ways, depending on N_{TC} per bin: If more than 100 TCs remain in a bin, the surviving N_{TC} is calculated by multiplying N_{TC} by the average SF given by equation (2.10): $N_{TC}^{\text{surviving}} = \text{SF} \cdot N_{TC}$. However, if less than 100 TCs remain, the fate of each TC is stochastically determined, using the respective SF as the average survival probability and a random number generator (RN), as shown in Figure 2.11:

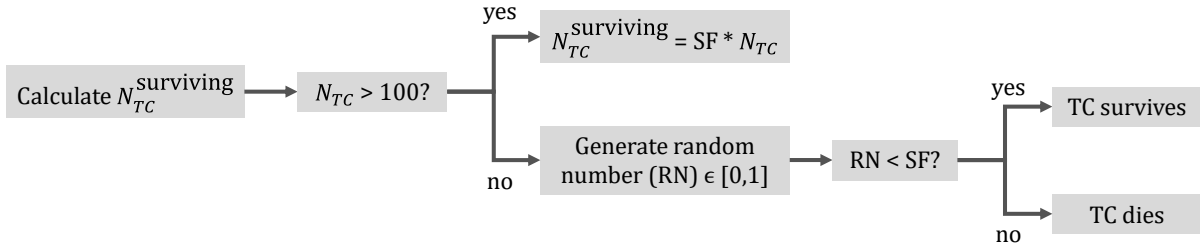


Figure 2.11: Process to calculate $N_{TC}^{\text{surviving}}$ for each bin of the oxygen histogram.

The threshold of 100 cells defines a compromise between computation time and biological accuracy of the model: Ideally, cell survival would be calculated stochastically for all cells. However, this stochastic approach comes with the cost of a longer calculation time and therefore is used only when N_{TC} falls below the defined threshold and when stochastic fluctuations become important. Due to this stochastic component, it is expected that two independent simulations for the same tumour lead to slightly different results.

The total number of surviving TC, $N_{TC}^{\text{surviving}}$, in a voxel is given by the sum of $N_{TC}^{\text{surviving}}$ over all bins in the oxygen histogram calculated by the above procedure. Those TCs killed by radiation are no longer considered as TCs but as DCs. CCs and NCs are considered completely radioresistant and are therefore not killed by radiation.

5. Dead cell resorption

DCs are assumed to be resorbed with time. DC resorption is modelled as an exponential probability function of time, with a given resorption half-time RT , after which half of the remaining dead cells are resorbed. The resorption factor RF is calculated as:

$$RF = \exp\left(-\frac{\ln(2)}{RT} \cdot t\right) \quad (2.24)$$

If more than 100 DC remain to be resorbed in the voxel, the remaining number of DC N_{DC}^{remain} is calculated as $N_{DC} \cdot RF$. However, if less than 100 DC remain, cell resorption is calculated stochastically employing a random number generator, using the RF as the average resorption probability, similarly as for cell kill.

6. Tumour shrinkage

The resorption of DCs leads to a decrease in the voxel cell density. Once the decrease is larger than 10% of the initial cell density, tumour shrinkage is triggered. Cells are exchanged between voxels, in proportion to the absolute cell density difference and inversely proportional to the distance to neighbouring voxels, for all cell types.

Further details about all biological processes are given in Espinoza's previous work [9], [10].

2.2.5 Integration with the Medical Imaging Interaction Toolkit (MITK)

The original TRM as developed by Espinoza at the German Cancer Research Center (DKFZ) has been further modified for the simulation to be executed from the Medical Imaging Interaction Toolkit (MITK). With this modification, the TRM can be executed from the MITK graphical user interface to simulate the radiation response of one single tumour. MITK also provides a platform to visualise the spatiotemporal development of the tumour, along with the additional image input and output files. The TRM implementation in MITK was possible thanks to the support of the Medical Image Computing department at the DKFZ.

2.3 Improvement of the TRM

The TRM as described in section 2.2 was developed in its basic version by Espinoza [9], [10]. In this thesis, the model was further developed and tested. These further developments are described in this section and the results are shown in section 3.

Stochastic components of proliferation and angiogenesis

A stochastic component for small cell numbers was added to the proliferation and angiogenesis functions, similarly as for the radiation-induced cell kill function (section 2.2.4): If less than 100 cells remain, the fate of each cell is stochastically determined, *i.e.* a cell either generates a new cell or not. This decision is simulated based on a random number generator and the average

proliferation probability ($PF - 1$), where PF is given by equations (2.21) and (2.22), for proliferation and angiogenesis respectively.

Variable type for cell counting

Initially, Espinoza implemented integers to count cells, motivated by the fact that cells are single discrete entities. As a result, computational cell loss due to rounding occurred when calculating $N_{TC}^{\text{surviving}}$ by multiplication with the SF. This issue was solved with the implementation of double-precision variables.

Stochastic distribution of cells in the oxygen histogram

Radiation-induced cell kill depends on the oxygen distribution, as shown in section 2.2.4. Before calculating the SF, N_{TC} per bin must be determined. This calculation was previously performed by multiplying the relative frequency f_i of the bin by N_{TC} : $N_{TC_i} = f_i \cdot N_{TC}$, leading to computational cell loss due to fractions of TCs not being distributed to the different oxygenation levels. To correct this, the distribution of all TCs over the oxygen histogram is now performed stochastically: Using the respective cumulative oxygen histogram and a random number generator, the bin to which a TC is assigned is determined. This implementation corrects the computational TC loss which has been visible in the SF curves. This implementation was performed in collaboration with A. Gago-Arias (Instituto de Investigación Sanitaria, Santiago de Compostela, Spain).

Code regression test

From a technical point of view, the TRM code is quite complex. To check if the TRM calculations are not unintentionally changed by code modifications, a regression test was implemented. Synthetic input images were generated to cover a wide range of combinations of VF, dose, and TC density. The regression test evaluates two scenarios, one considering bone and air structures and the other one only soft tissue. During the test, all functions in the TRM are executed and other basic code structures are tested. The test is passed if all functions are correctly executed, and if the resulting cell distribution does not differ from the stored reference distribution by more than 10^{-10} . The regression test was implemented with the support of the Medical Image Computing department at the DKFZ.

2.4 Adjustment of the TRM to experimental *in-vivo* data

The validation of the TRM as an adequate model to predict the response of hypoxic tumours to radiotherapy can be achieved by fitting the simulation model to experimental *in-vivo* data. In this

thesis, the input parameters of the TRM are adjusted to reproduce the TCP curves obtained for three different tumour sublines of a rat prostate carcinoma irradiated with different fractionation schemes [11]–[14], [55], [56]. In this section, the experimental data is presented, followed by the strategy to adjust the TRM parameters to describe the experimental dose-response curves.

2.4.1 Experimental *in-vivo* data

Three different syngeneic rat prostate adenocarcinomas sublines, Dunning R3327-AT1, -HI, and -H were studied. These syngeneic tumours are a good model system for human prostate tumours and have been extensively characterised. The different sublines vary in degree of differentiation, overall cell density, proliferation rate, hypoxic status, and hormonal response. The main endpoint studied was local tumour control, represented by TCP curves for each tumour subline [11]–[14], [57], [58].

Fresh tumour segments were implanted in the distal thigh of male Copenhagen rats. At the time of treatment, the mean tumour diameter was 10 mm. The animals were irradiated under anaesthesia with a single 6MV photon beam, shaped with a cylindrical tungsten collimator to provide a 90% isodose of 15 mm at the isocenter, with the tumour located at 99 cm from the beam source. A homogeneous depth-dose profile in the tumour was achieved by placing two polymethylmethacrylate boli in front and behind the tumour. The lateral dose distribution in the x- and the y-axis is shown in Figure 2.12, where the position of the tumour within the 95% isodoses can be seen. For fractionated treatments, the dose was delivered in consecutive days. Tumour control was the primary endpoint measured in these studies and was defined as no detectable tumour regrowth assessed up to 300 days after the last fraction was delivered.

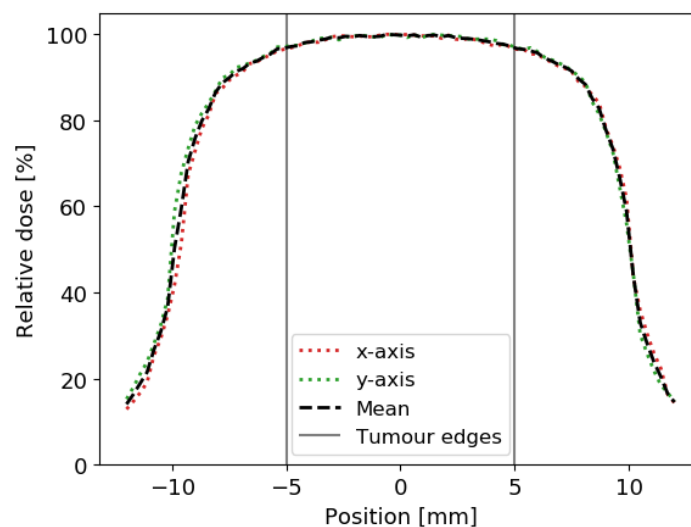


Figure 2.12: Experimental dose profiles in the x- and y-axis obtained for 50 monitor units. The tumour is located within the 95% isodoses. For this thesis, the average profile was used for the simulations.

Biological characterisation

Tumour growth, total and tumour cell density for the three tumour sublines were determined by immunohistochemistry and flow cytometric characterisation [11], [55], [56].

- The tumour volume of untreated animals was calculated assuming the tumours were spherical, with the diameter determined by the average orthogonal diameter measured with a calliper. The growth data for the AT1 tumour subline can be found in the literature [11], [12], whereas the original growth data for the HI and H tumour sublines were kindly provided by C. Glowa. The complete growth data for the three tumour sublines is shown in Figure 2.13.
- Cell nuclei were stained with 4',6-diamidino-2- phenylindole (DAPI). The total number of cells per mm^2 was determined as the ratio of DAPI⁺ cells and the area of the analysed histological sample. The average DAPI⁺ nucleus diameter was determined as $8.3 \pm 1.3 \mu\text{m}$. Taking into account that the slice thickness (ST) of the tumour samples studied was $7 \mu\text{m}$, it is assumed that most DAPI⁺ nuclei are detected at most in two of the consecutive slices analysed. Under this assumption, the volumetric cell density is given by equation (2.25). Original data collection and analysis was performed by A. Bendinger and C. Glowa [56]. Additional image protocols not included in the literature can be found in the Appendix (page 66).

$$\rho_C = \frac{N_C}{\text{mm}^3} = \frac{N_C}{\text{mm}^2} \cdot \frac{1}{\text{ST}} \quad (2.25)$$

- The TC density was determined by counting the cytokeratin 19 positive cells (CK19⁺) [55]. The volumetric TC density ρ_{TC} is then calculated as the product of the CK19⁺ percentage by the volumetric cell density given by DAPI ρ_C : $\rho_{TC} = \%_{\text{CK19}^+} \cdot \rho_C$.
- To illustrate the biological differences between the three tumour sublines, tumour samples were analysed. Samples were stained with haematoxylin and eosin (H&E) to visualise tumour morphology. Capillaries were stained with the cluster of differentiation (CD31), perfusion with Hoechst 33342, and hypoxia with pimonidazole. Images were obtained by A. Bendinger and are shown in Figure 2.14 along with samples of DAPI staining for the different tumour sublines [56].

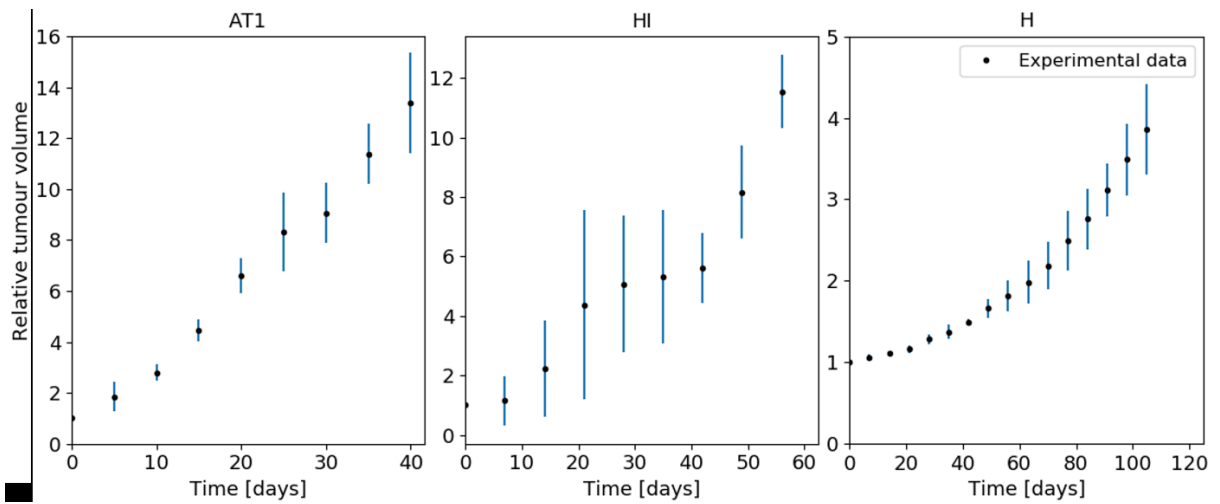


Figure 2.13: Relative tumour volume growth as a function of time for the tumour sublines AT1 (left), HI (centre), and H (right). The error bars correspond to one standard error (SE).

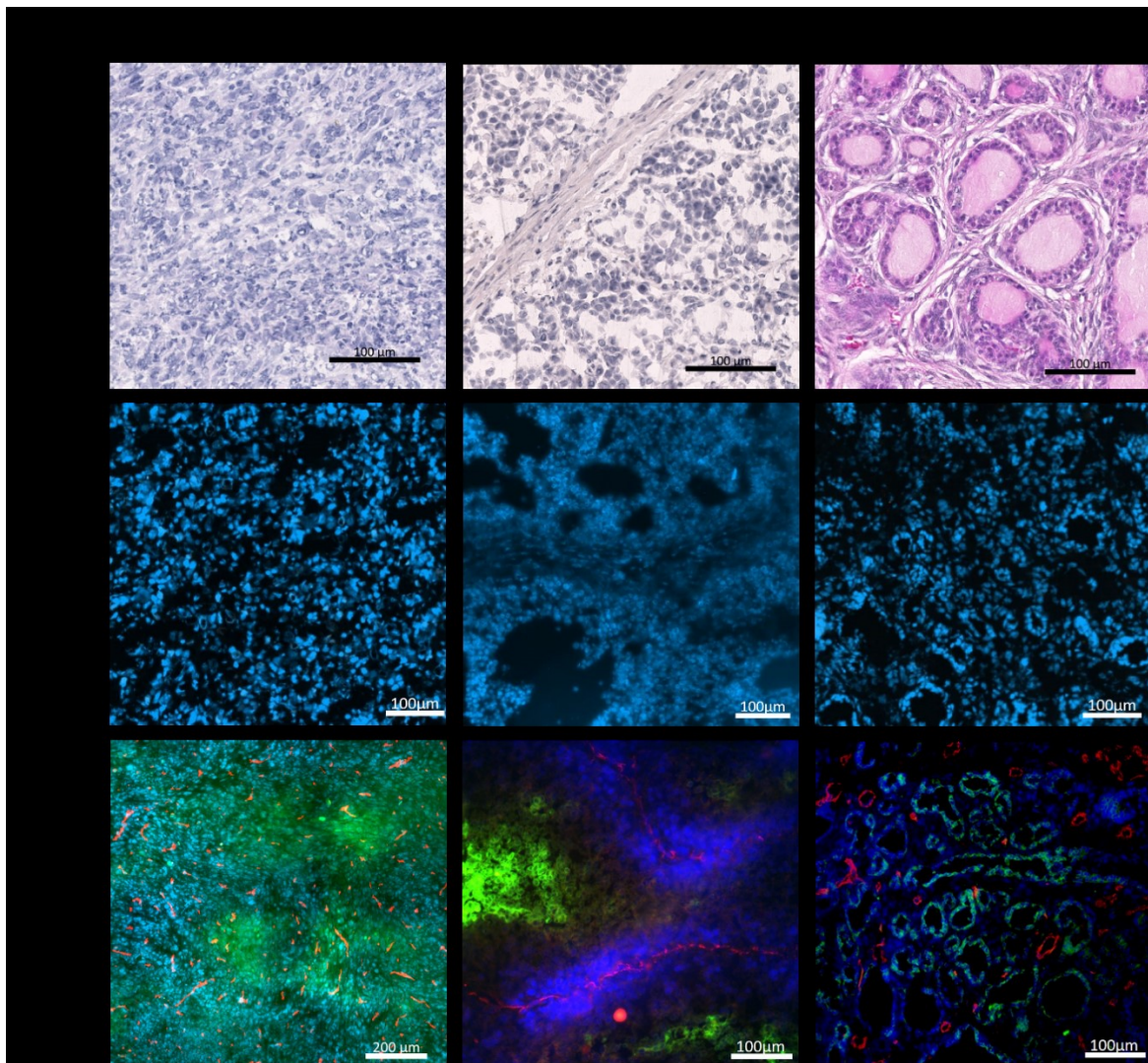


Figure 2.14: Tumour samples obtained for different staining procedures, showing morphology (H&E, top row), cell nuclei (DAPI, middle row), capillaries (CD31, bottom row, red), hypoxia (Pimo, bottom row, green) and perfusion (Hoechst, bottom row, blue), for the tumour sublines AT1 (left column), HI (centre column), and H (right column). According to A. Berdinger's observations, the anaplastic AT1

tumour exhibited no differentiated cells, short and thin capillaries, with the presence of both well-perfused and hypoxic areas. The moderately-differentiated HI tumour showed some glandular structures and immature vessels, not all of them perfused with hypoxic areas at large distances from vessels. The H tumour is well-differentiated, with glandular structures similar to those of healthy prostate glands. This tumour subline also showed good perfusion and only small confined hypoxic regions. [56].

TCP curves

Incidences for tumour control at different dose levels were determined for the three tumour sublines for 1, 2, and 6 fractions. TCP curves were fitted to this data with the logistic dose-response model given by equation (2.13) using a maximum likelihood estimation. As a result, each curve is described by the two fitting parameters b_0 and b_1 , with D_{50} given by equation (2.14). Additionally, the LQM parameter α/β was estimated by adjusting all TCP curves with a generalised logistic dose-response model [14]. In this case, the parameter α/β has to be considered as “effective” (α/β_{eff}^{exp}), since it is expected for *in-vivo* measurements that all tumour-related processes, such as repopulation and reoxygenation (section 2.1.2), impact its determination. Therefore, α/β_{eff}^{exp} effectively describes how the tumour control for each tumour subline is affected by fractionation without being solely related to repair as assumed in the LQM. All parameters of the adjusted TCP curves are summarised in Table 2.2, and the TCP curves for the different fractionation schemes are shown in Figure 2.15.

Table 2.2: Fitting parameters b_0 and b_1 for experimental TCP curves of 1, 2, and 6 fractions, with the corresponding D_{50} , and α/β_{eff}^{exp} for the three tumour sublines. The values of D_{50} and α/β_{eff}^{exp} are reported in the literature [11]–[14], whereas the original fitted values of b_0 and b_1 were kindly provided by C. Karger. The α/β_{eff}^{exp} for the H subline could not be calculated due to the non-convergence of the logistic regression. The reported value was therefore obtained with the Douglas-Fowler method, based only on the D_{50} values, and no uncertainty calculation was possible [14].

Tumour subline	Fractions	b_0	b_1	$D_{50} \pm SE$ [Gy]	TCP'(D ₅₀) [Gy ⁻¹]	$\alpha/\beta_{eff}^{exp} \pm SE$ [Gy]
AT1	1	-25.4844	0.33645	75.7 ± 1.6	0.08411	
	2	-18.6783	0.20614	90.6 ± 2.3	0.05154	84.7 ± 13.8
	6	-22.7177	0.19485	116.6 ± 3.0	0.04871	
HI	1	-6.8705	0.11016	62.4 ± 3.2	0.02754	
	2	-6.0478	0.08257	73.2 ± 4.0	0.02064	87.7 ± 32.9
	6	-5.3321	0.05841	91.3 ± 6.3	0.01460	

	1	-8.4854	0.22218	38.2 ± 1.8	0.05554	
H	2	-21.444	0.39941	53.7 ± 1.5	0.09985	0.40
	6	-4.6593	0.05115	93.0 ± 6.3	0.01279	

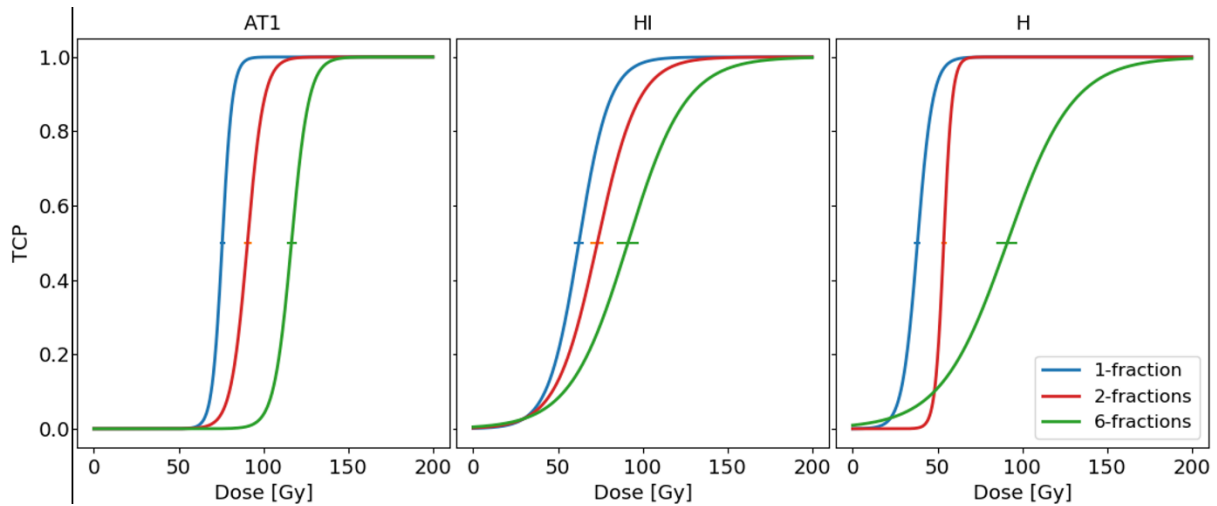


Figure 2.15: TCP curves obtained from the adjustment to the experimental data for the tumour sublines AT1 (left), HI (centre), and H (right), for 1, 2, and 6 fractions. The SE for D_{50} is marked by the horizontal error bars [11]–[14].

2.4.2 Adjustment to experimental *in-vivo* data

In this section, the procedure to adjust the input parameters of the TRM to fit the experimental *in-vivo* TCP curves (see section 2.4.1) is explained. Due to the complexity of the TRM, the parameters were fitted considering first the 1-fraction TCP curve and in a second step the 2- and 6-fractions curves. The strategy to simulate the incidence rates, to fit a single TCP curve and to adjust the TRM parameters to describe all the experimental dose-response curves for different fractionation schemes are described in this section. This procedure was repeated for each tumour subline.

Simulating incidence rates and adjusting TCP curves

The TCP curve is the result of fitting the logistic dose-response model to tumour control incidence rates (see section 2.1.2). These incidence rates are obtained by simulating the response of many tumours at different dose levels. After the treatment delivery, each tumour is either controlled or not controlled, and, as a result, an incidence rate is calculated for each dose level, as shown in Figure 2.7.

The TRM code cannot be parallelised, due to the complexity and interdependency of the biological processes considered. However, many TRM simulations of different tumours can be executed in

parallel: In this thesis, the Python* subprocess management module was used to spawn multiple TRM simulations of m tumours irradiated at different dose levels D to obtain a single TCP curve. The same procedure can be followed for different fractionation schemes, where $D = nd$ (section 2.1.2). Once the incidence rate is obtained, the TCP curve is fitted in R† using the logistic dose-response model shown in equation (2.13), using a maximum likelihood estimation.

Optimizing the TRM parameters to fit experimental 1-fraction TCP curves

To establish the best strategy to fit the TRM parameters to the experimental data, it is important to consider the four main factors influencing the simulated TCP curves:

- α : This parameter determines the radiosensitivity of the tumour, and therefore the cell survival as calculated with equation (2.10).
- σ_α : Variation of the radiosensitivity α between tumours. A larger variability leads to shallower TCP curves. The probability distribution used to sample α is given by equation (2.23).
- α/β : The behaviour of the TCP curves for different fractionation schemes is defined by α/β , as exemplified in Figure 2.2.
- Stochastic components of the TRM: As mentioned in section 2.2, the TRM is composed of different stochastic processes, associated with deciding the cell's fate for growth and survival, as well as with sampling the radiosensitivity of the simulated tumour. Therefore, it is expected that two independently simulated TCP curves for the same tumour type using the same input parameters result in slightly different TCP curves. This variation must be considered when searching the optimal TRM parameters.

Considering these factors, the following hierarchical strategy to fit the TRM parameters to a single experimental TCP curve is used:

- a. Use fixed values of VF and α/β .
- b. Use starting values of α and σ_α to simulate k independent TCP curves and to calculate the doses at TCP of 20%, 50%, and 80% for each curve (*i.e.*, D_{20} , D_{50} , and D_{80}).
- c. These dose levels are used for the adjustment to the experimental 1-fraction TCP curve using the objective function value $OF(\alpha, \sigma_\alpha)$ as the squared difference of the experimental and simulated reference doses, D^{exp} and D^{sim} respectively:

$$OF(\alpha, \sigma_\alpha)_k = (D_{20}^{sim} - D_{20}^{exp})^2 + (D_{50}^{sim} - D_{50}^{exp})^2 + (D_{80}^{sim} - D_{80}^{exp})^2 \quad (2.26)$$

* Python programming language, versions 4.7.12 and 4.8.2

† R software environment for statistical computing, versions 3.6.2 and 4.1.1.

While the D_{50} -term adjusts the position of the curve, the D_{20} and D_{80} - terms are sensitive to the slope.

- d. Minimize the average objective function given by:

$$\overline{\text{OF}(\alpha, \sigma_\alpha)} = \frac{1}{k} \sum_{i=1}^k \text{OF}(\alpha, \sigma_\alpha)_k \quad (2.27)$$

where k is the number of simulated TCP curves. The averaging over k TCP curves is performed to minimise the impact of the stochastic components of the TRM on the objective function. The minimisation of $\overline{\text{OF}(\alpha, \sigma_\alpha)}$ is performed with the `optimize.minimize` function of the Python-based ecosystem SciPy [59], via the Nelder-Mead gradient-less search method [60], [61].

This fitting strategy allows finding α and σ_α to simulate the 1-fraction experimental TCP curve for the given VF and α/β , taking into account the stochasticity of the TRM results.

Optimizing the TRM parameters to fit the fractionation dependence

Using the parameters obtained from the adjustment of the 1-fraction TCP-curve as starting values, the curves for 2 and 6 fractions are adjusted to the experimental curves as follows:

1. Use the fixed VF value
2. Select a new value of α/β . As this changes, also the 1-fraction TCP curve changes and therefore the adjustment of α and σ_α (steps a.-d. previously described) is repeated.
3. Simulate the 2- and 6-fractions TCP curves with the new α/β , and the readjusted α and σ_α , by changing only the treatment parameters (number of fractions and total dose).
4. Assess the parameter adjustment using the adjustment quantitative metric (AQM), based on the simulated and experimental TCP of 20%, 50%, and 80%, (*i.e.*, D_{20} , D_{50} , and D_{80}), for the 2- and 6-fraction experiments:

$$\text{AQM} = \frac{1}{2} \left(\left(\left(\frac{D_{50}^{exp} - D_{50}^{sim}}{D_{50}^{exp}} \right)^2 + \frac{1}{2} \left[\left(\frac{D_{20}^{exp} - D_{20}^{sim}}{D_{20}^{exp}} \right)^2 + \left(\frac{D_{80}^{exp} - D_{80}^{sim}}{D_{80}^{exp}} \right)^2 \right] \right) \right)_{2fx} \quad (2.28)$$

$$+ \left(\left(\frac{D_{50}^{exp} - D_{50}^{sim}}{D_{50}^{exp}} \right)^2 + \frac{1}{2} \left[\left(\frac{D_{20}^{exp} - D_{20}^{sim}}{D_{20}^{exp}} \right)^2 + \left(\frac{D_{80}^{exp} - D_{80}^{sim}}{D_{80}^{exp}} \right)^2 \right] \right)_{6fx}$$

5. Iterate α/β and consequently α and σ_α to best reproduce the 1-fraction TCP curve (based on minimising $\overline{\text{OF}(\alpha, \sigma_\alpha)}$) and to minimise the deviations for 2 and 6 fractions (based on minimising AQM).

The complete workflow for the parameter adjustment is shown in Figure 2.16.

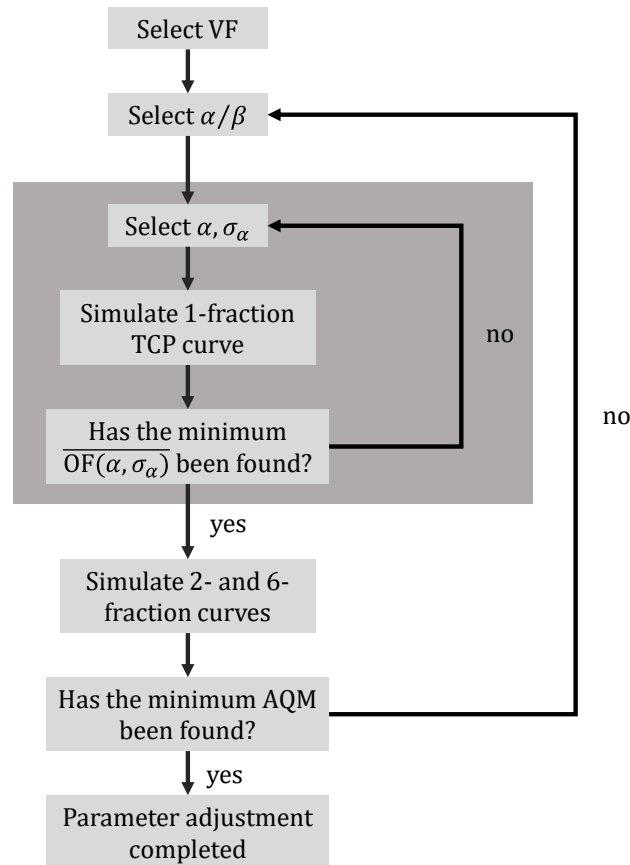


Figure 2.16: Workflow to adjust the TRM parameters to reproduce experimental TCP curves for 1, 2, and 6 fractions.

2.4.3 Simulations

The ultimate aim of this thesis is to investigate the capabilities of the TRM to reproduce experimental *in-vivo* data. For this investigation, three main questions are addressed:

1. Is the TRM consistent with LQM-based analytical calculations?
2. How do the key input parameters in the TRM impact the TCP curves?
3. Can the TRM input parameters be adjusted to reproduce experimental *in-vivo* data?

With this in mind, the simulations performed with the TRM were divided into three different groups, and the motivation behind each of these groups is explained in this section. The obtained results are described in section 3.

1. Validation by analytical calculations

The core of the TRM is the LQM, which allows calculating the SF considering the impact of oxygen in the tumour response to radiation, given by equation (2.10). Therefore, the TRM validation is achieved by comparing the simulated results with analytical calculations, in terms of SF and TCP. Additionally, the different features and improvements of the TRM described in section 2.3 are

shown. This set of results should equip the reader with an understanding of the different TRM components and improvements in terms of SF and TCP curves.

For these simulations, a spherical tumour was irradiated with a uniform dose distribution. No air or bony structures were considered, therefore the simulation volume was composed of only soft tissue, discretised by 1 mm³ cubic voxels. SF and TCP curves were generated with only the TRM radiation-induced cell kill process turned on to compare the simulated results with the LQM predictions, while all the other biological processes were turned off (see section 2.2.4). The different TRM features and improvements are shown by turning on and off different TRM biological processes and components, and by comparing the results with previous versions of the code. The dose to obtain the TCP curves was varied by increasing the number of fractions while keeping the same dose per fraction.

Table 2.3: Parameter values used for the simulations to compare the TRM with LQM predictions and to show the model features and improvements. The values for cell densities, OER, and those associated with the tumour development and treatment were chosen to exhibit the different features and improvements of the model. References are given for the VDT_{angio} and RT, which are kept constant for all the simulations presented in this thesis. The VDT corresponds to the average VDT value from the growth fit data for the three experimental tumour sublines, shown in section 3.3.1.

Characterization	Parameter	Symbol	Value
Anatomy	Tumour diameter	-	4 mm
	Total cell density	ρ_C	1×10^6 cells/mm ³
	Tumour cell density	ρ_{TC}	2.3×10^5 TC/mm ³
Hypoxic status	Oxygen partial pressure	pO_2	11.25 mmHg
	Oxygen enhancement ratio	OER	2.579
	Maximum OER	m	3
	pO_2 at OER half-range	k	3 mmHg
Tumour development	Volume doubling time	VDT	760.17 hours
	VDT angiogenesis	VDT_{angio}	612 hours [62]
	Resorption half-time	RT	168 hours [63]
	Tumour fractionation response	α/β	10 Gy
	Tumour radiosensitivity	α	0.2 Gy^{-1}
	Sensitivity heterogeneity	σ_α	$0 - 0.02 \text{ Gy}^{-1}$
Treatment	Total dose	D	2 - 70 Gy
	Dose per fraction	d	2 Gy

2. The interplay of key input parameters

As a first step to the parameter adjustment to experimental data, the interplay of the OER and α/β is shown. For this, a single pO_2 value is used, allowing the calculation of a tumour OER with equation (2.9). As for the previous simulations, all biological processes in the TRM were turned off, except for the radiation-induced cell kill. The impact of varying the OER for different α/β values is illustrated by the relative and absolute variation of the TCP curves. This set of simulations aims to show the behaviour of the clinical parameters predicted by the TRM and to establish how the TRM key parameters impact the TCP curves relative to the experimental curves.

For these simulations, a spherical tumour was irradiated with a uniform dose distribution. The simulation domain was conformed only by soft tissues, with no air or bony structures, discretised by 1 mm³ cubic voxels. Incidence rates were generated by increasing the total dose while maintaining the number of fractions fixed.

Table 2.4: Parameter values used for the simulations to study the interplay effect of the key input parameters of the TRM. The cell densities and VDTs correspond to the experimental values obtained for the AT1 tumour subline, shown in section 3.3.1. References are given for the VDT_{angio} and RT, which are kept constant for all the simulations presented in this thesis. α and σ_α were adjusted to the 1-fraction experimental TCP curve, as described in section 2.4.2.

Characterization	Parameter	Symbol	Value
Anatomy	Tumour diameter	-	4 mm
	Total cell density	ρ_C	593634 cells/mm ³
	Tumour cell density	ρ_{TC}	461253 TC/mm ³
Hypoxic status	Oxygen partial pressure	pO_2	1.25 – 38.75 mmHg
	Oxygen enhancement ratio	OER	1.59 – 3
	Maximum OER	m	3
	pO_2 at OER half-range	k	3 mmHg
Tumour development	Volume doubling time	VDT	121.66 hours
	VDT angiogenesis	VDT_{angio}	612 hours [62]
	Resorption half-time	RT	168 hours [63]
	Tumour fractionation response	α/β	1, 10 and 84.7 Gy
	Tumour radiosensitivity	α	<i>To be adjusted</i>
	Sensitivity heterogeneity	σ_α	<i>To be adjusted</i>
Treatment	Total dose	D	60 – 250 Gy
	Fractions	n	1, 2, and 6

3. Adjustment to experimental *in-vivo* data

The TRM input parameters are adjusted to simulate the experimental *in-vivo* TCP curves of three different rat prostate carcinomas, as described in sections 2.4.1 and 2.4.2. The parameters adjusted are α/β , α and σ_α , for three different oxygenation conditions: Severe hypoxia, mild hypoxia and well-oxygenated, defined by different initial oxygen histograms. The fitting quality is determined by the $\overline{OF}(\alpha, \sigma_\alpha)$ and the AQM, given by equation (2.27) and (2.28). This parameter adjustment aims to further understand how different biological processes, represented by the TRM components, impact the *in-vivo* tumour response to radiation, and how the oxygenation status influences the interplay of the TRM input parameters reflected in the TCP curves.

For these simulations, a spherical tumour was considered, without any adjacent air or bony structures. The simulation domain was discretised by 1 mm³ cubic voxels, and the simulations were performed including all TRM biological processes mentioned in section 2.2.4 unless specified otherwise. All tumours were irradiated with a dose distribution defined by the mean experimental dose profile shown in Figure 2.12, with a constant dose-depth profile. The parameters α , σ_α and α/β were fitted following the procedure described in section 2.4.2 and summarised in Figure 2.16. This procedure was repeated for three oxygenation scenarios: Severe hypoxia, mild hypoxia and well-oxygenated, characterised by an initial vascular fraction VF_0 of 1%, 3%, and 5-10% (selected as 5%, 7% or 10%), respectively. The corresponding initial histograms are shown in Figure 2.17. The three oxygenation scenarios were studied for the three experimental tumour sublines AT1, HI, and H, and the corresponding experimental parameters (parameters for incidence rates shown in section 2.4.1, cell densities and VDT described in section 3.3.1) were used for each case.

Table 2.5: Parameter values used for the simulations to adjust the TRM input parameters to experimental *in-vivo* data. The cell densities and VDTs are tumour-specific and were calculated for each tumour subline as shown in section 3.3.1. References are given for the VDT_{angio} and RT, which are kept constant for all the simulations presented in this thesis. The values of α , σ_α and α/β are obtained as a result of the parameter adjustment for each VF considered, as shown in section 2.4.2 and illustrated in Figure 2.16.

Characterization	Parameter	Symbol	Value
Anatomy	Tumour diameter	-	10 mm
	Total cell density	ρ_C	<i>Tumour-specific</i>
	Tumour cell density	ρ_{TC}	<i>Tumour-specific</i>
Hypoxic status	Initial vascular fraction	VF_0	1%, 3%, 5%, 7%, 10%
	Maximum OER	m	3
	pO_2 at OER half-range	k	3 mmHg

	Volume doubling time	VDT	<i>Tumour-specific</i>
	VDT angiogenesis	VDT _{angio}	612 hours [62]
Tumour development	Resorption half-time	RT	168 hours [63]
	Tumour fractionation response	α/β	<i>To be adjusted</i>
	Tumour radiosensitivity	α	<i>To be adjusted</i>
	Sensitivity heterogeneity	σ_α	<i>To be adjusted</i>
Treatment	Total dose	D	30 – 250 Gy
	Fractions	n	1, 2, and 6

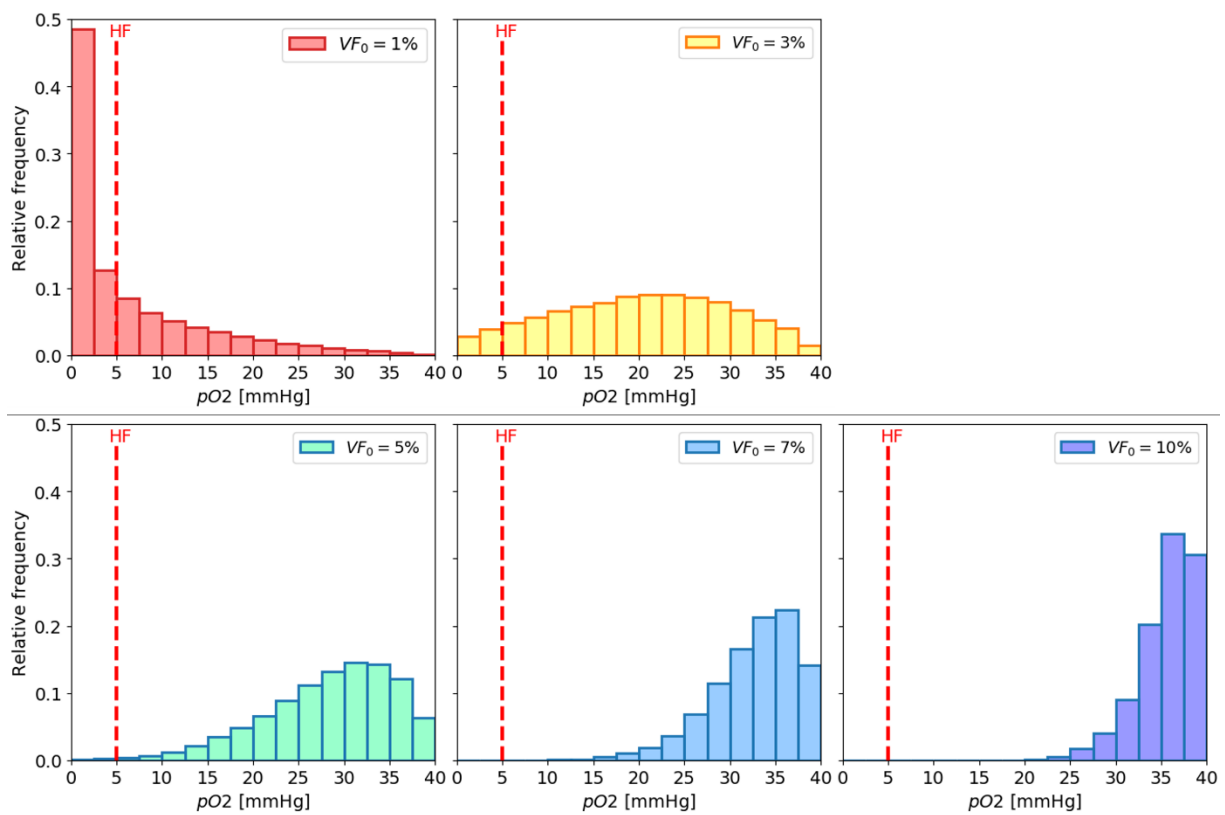


Figure 2.17: Initial oxygen histograms for the three oxygenation conditions considered, characterised by the corresponding VF_0 : severe hypoxia ($VF_0 = 1\%$), mild hypoxia ($VF_0 = 3\%$), and well-oxygenated ($VF_0 = 5\%$, 7% or 10%). The HF corresponds to the oxygen bins below the dashed red line. These oxygen histograms are a representative example of the three initial oxygenation conditions considered.

3 Results

3.1 Validation by analytical calculations

The TRM was compared to the LQM, as described in section 2.4.3. For this comparison, all the biological processes considered in the TRM were turned off, except for the radiation-induced cell kill. SF curves were generated for a fractionated treatment of 35 daily fractions of 2 Gy, delivered on consecutive days for three different degrees of radiosensitivity heterogeneity, as given by the parameter σ_α .

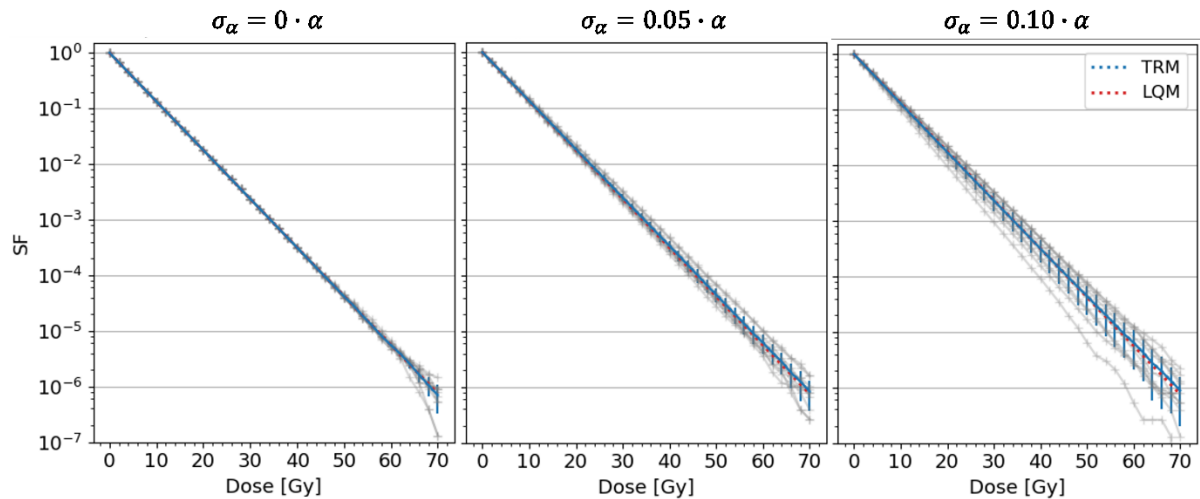


Figure 3.1: Comparison of SF curves calculated with the LQM and the TRM. For the TRM, three different radiosensitivity heterogeneities were used: $\sigma_\alpha = 0 \cdot \alpha$ (left), $\sigma_\alpha = 0.05 \cdot \alpha$ (centre), and $\sigma_\alpha = 0.10 \cdot \alpha$ (right), and the mean SF curve was obtained by averaging the SF curves for 10 independently simulated tumour samples, represented by the grey curves. Error bars of one standard deviation (SD) are shown for the TRM mean SF curve. Additional TRM input parameters are summarised in Table 2.3.

As shown in Figure 3.1, the average SF calculated with the TRM shows no significant deviations when compared to the LQM predictions, for the three degrees of radiosensitivity heterogeneity. As the heterogeneity increases, the slope variation between the curves of the individual tumours increases as a result of the lognormal distribution of the radiosensitivity parameter α given by equation (2.23). Additionally, as the SF decreases, larger deviations between the LQM and the TRM are observed. In particular, for the SF curves obtained for $\sigma_\alpha = 0 \cdot \alpha$, deviations between each sample and the mean curve occur for $SF < 10^{-5}$, due to implemented stochastic cell kill mechanism for less than 100 surviving TCs (see section 2.2.4 and Figure 2.11).

The following simulations were performed with the proliferation and angiogenesis components turned on, to also reflect the stochasticity associated with these two components, as described in section 2.3. Since the radiation-induced cell kill is the dominant process in changing the total

number of cells, it was necessary to add additional breaks in the radiation schedule to observe the proliferation-related changes in the response. For this reason, weekend breaks were introduced to the treatment, as well as 5 additional radiation-free days to monitor tumour growth after the delivery of the last fraction. The SF curves obtained for 10 independently simulated tumour samples are shown in Figure 3.2.

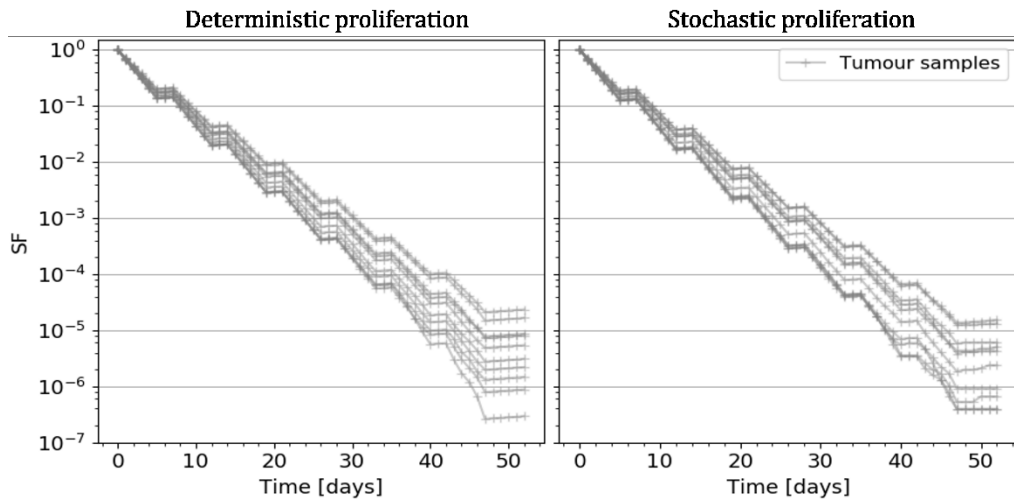


Figure 3.2: SF curves obtained with $\sigma_\alpha = 0.10 \cdot \alpha$ for 10 independently simulated tumour samples, with deterministic (left) and stochastic (right) proliferation and angiogenesis. The simulated radiation schedule consisted of daily 2 Gy fractions from Monday to Friday, with a weekend break and 5 days of tumour growth after the delivery of the last fraction (day 47). Additional TRM input parameters used for these simulations are summarised in Table 2.3.

When the proliferation is performed deterministically, the SF of all tumours increases at the same rate, regardless of their SF, as observed in Figure 3.2-left. On the other hand, with stochastic proliferation, the SF increment rate varies among tumours for $SF < 10^{-5}$, approximately from day 40.

The TRM was also compared with the LQM in terms of TCP. For this, the LQM-based Poisson model given by equation (2.12) was implemented. For the simulated TCP curves, 10 tumour samples were generated for each dose level, each level obtained by increasing the number of 2 Gy-fractions delivered. Simulations were performed considering only one TRM biological process at a time, and for each case, 10 TCP curves were independently simulated. Simulations were performed with $\sigma_\alpha = 0 \cdot \alpha$ to obtain results directly comparable to the LQM. The simulated and calculated TCP curves are shown in Figure 3.3, and the corresponding D_{50} values are summarised in Table 3.1.

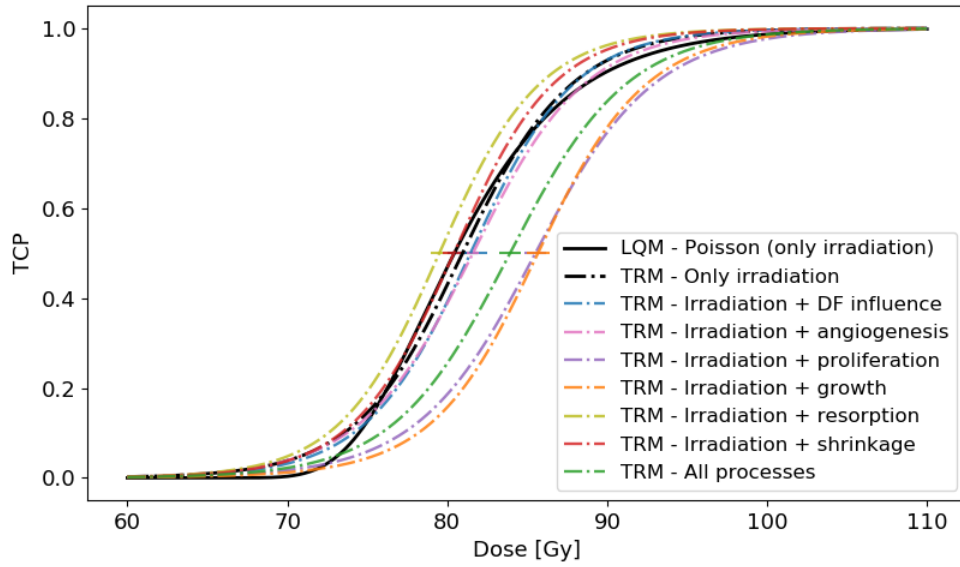


Figure 3.3: TCP curves simulated with the TRM (solid lines) and calculated with the LQM-based Poisson model (dotted lines). The different TRM-simulated curves were obtained by including only one biological process of the TRM at a time. Each of these curves corresponds to the average of 10 independently simulated curves, with error bars indicating one standard deviation (SD). Additional TRM input parameters used for these simulations are summarised in Table 2.3.

Table 3.1: Values of D_{50} and corresponding SD for the simulated and calculated TCP curves shown in Figure 3.3. The significance of the effect of turning on/off the different TRM components on the D_{50}^{TRM} vs D_{50}^{LQM} relative to the displayed standard deviations (SD) is shown in the third column.

Case	$D_{50} + SD$ [Gy]	D_{50}^{TRM} vs D_{50}^{LQM}
LQM-based Poisson model	80.44	-
TRM - Only irradiation	80.96 ± 0.92	$D_{50}^{TRM} \approx D_{50}^{LQM}$
TRM - Irradiation + DF influence	81.46 ± 1.05	$D_{50}^{TRM} \approx D_{50}^{LQM}$
TRM - Irradiation + angiogenesis	81.61 ± 0.40	$D_{50}^{TRM} > D_{50}^{LQM}$
TRM - Irradiation + proliferation	85.51 ± 0.66	$D_{50}^{TRM} > D_{50}^{LQM}$
TRM - Irradiation + angiogenesis + proliferation + growth	85.67 ± 0.73	$D_{50}^{TRM} > D_{50}^{LQM}$
TRM - Irradiation + resorption	79.51 ± 0.51	$D_{50}^{TRM} < D_{50}^{LQM}$
TRM - Irradiation + resorption + shrinkage	80.41 ± 0.66	$D_{50}^{TRM} \approx D_{50}^{LQM}$
TRM - All processes	83.93 ± 0.64	$D_{50}^{TRM} > D_{50}^{LQM}$

The TCP curves obtained with the TRM were comparable with the LQM-based Poisson model when the TRM considers only the radiation-induced cell kill with no influence of the DF in the oxygen histogram selection (see section 2.2.3), as well as no other biological process, *i.e.*, for the case “TRM – Only irradiation”. For these two cases, represented by the black solid (TRM) and dotted (LQM-Poisson model) lines in Figure 3.3, no significant difference in D_{50} was found: $D_{50}^{\text{LQM}} = 80.44 \text{ Gy}$ vs $D_{50}^{\text{TRM}} = 80.96 \text{ Gy} \pm 0.92 \text{ Gy}$, as shown in Table 3.1. However, the two TCP curves deviate slightly in their shape, as can be seen in the TCP intervals of 0.0 – 0.2 and 0.8 – 1.0. No significant differences in D_{50} between the simulated and LQM-calculated TCP curves were also found for the following cases: “TRM – Irradiation + DF influence” and “TRM - Irradiation + shrinkage”. The only case with $D_{50}^{\text{TRM}} < D_{50}^{\text{LQM}}$ was “Irradiation + resorption”, where the DCs are resorbed with a resorption half-time of 168 hours *i.e.*, 7 days (Table 2.3). $D_{50}^{\text{TRM}} > D_{50}^{\text{LQM}}$ was obtained for the following cases: “Irradiation + angiogenesis”, “Irradiation + DF influence”, “Irradiation + proliferation”, “Irradiation + growth”, and “All processes”. The largest deviation occurred for “Irradiation + growth”, with a D_{50}^{TRM} shifted to higher doses by 5.23 Gy. When all the TRM biological processes are included, D_{50}^{TRM} was shifted to higher doses by 3.49 Gy relative to D_{50}^{LQM} .

3.2 The interplay of key input parameters

To understand how the TRM key input parameters impact the TCP curves, simulations were performed for different fractionation responses given by three values of α/β , for different oxygenation conditions, as described in section 2.4.3. To isolate the effects caused by the mentioned parameters, all biological processes in the TRM were turned off except for the radiation-induced cell kill. The parameters α and σ_α were adjusted to reproduce the experimental 1-fraction TCP curve for the AT1 tumour subline, as described in section 2.4.2. Since the purpose of these simulations was to study the behaviour of the TCP curves rather than adjusting all the parameters to reproduce the experimental data, the second part of the adjustment, where α/β is fitted using the AQM (see section 2.4.2 and equation (2.28)), was not performed. The simulated TCP curves are shown in Figure 3.4, along with the experimental curves for all the fractionation schemes.

The results shown in Figure 3.4 reflect the complex interplay between the TRM key parameters, and therefore each effect will be considered separately. Additionally, it is important to remember that for all combinations of α/β and OER, the parameters α and σ_α were fitted to reproduce the 1-fraction AT1 experimental TCP curve, and therefore all 1-fraction simulated TCP curves overlap with the corresponding experimental curve.

Observing first the impact of the OER on the TCP curves and how they changed relatively to the best-possible oxygenation scenario of OER = 3.00, larger deviations were found as the α/β increased: for $\alpha/\beta = 1$ Gy, the 6-fraction D_{50} decreased 3.2 Gy when OER varied from 3.00 to 1.59. In contrast, for the same OER change, the 6-fraction D_{50} decreased by 11.8 Gy for $\alpha/\beta = 10$ Gy, and by 16.3 Gy for $\alpha/\beta = 84.7$ Gy, following equation (2.11). A similar but less pronounced effect is observed for the 2-fractions TCP curves.

Considering now the impact of α/β on the D_{50} , the fractionation effect is observed in the larger spread of the TCP curves as α/β decreased: Taking as reference the 1-fraction $D_{50} = 75.7$ Gy, the average D_{50} overall OER values, $\overline{D_{50}^{OER}}$, increased by 30.0 Gy and 107.3 Gy for the 2- and 6-fraction TCPs, respectively, for $\alpha/\beta = 1$ Gy. For $\alpha/\beta = 10$ Gy, a less pronounced $\overline{D_{50}^{OER}}$ increment of 28.0 Gy and 92.5 Gy were obtained for the 2- and 6-fraction TCP curves, respectively. For the largest α/β value of 84.7 Gy, corresponding to the experimental α/β_{eff}^{exp} (see section 2.4.1), the smallest $\overline{D_{50}^{OER}}$ shifts were found: 15.3 Gy and 35.6 Gy for the 2- and 6-fraction TCP curves.

Under the conditions of these simulations, where the only active biological process in the TRM was the radiation-induced cell kill, the experimental TCP curves were better reproduced with $\alpha/\beta = 84.7$ Gy, for either OER = 2.86 and 3.00 (see section 2.4.1, and Figure 3.4-bottom). For OER = 2.86, the obtained D_{50} was 76.0 ± 0.6 Gy, 92.4 ± 0.8 Gy, and 115.6 ± 1.0 Gy for the 1-, 2-, and 6-fraction TCP curves, respectively, while for OER = 3.00 the obtained D_{50} was 75.7 ± 0.9 Gy, 92.9 ± 1.2 Gy, and 117.5 ± 1.0 Gy for the 1-, 2-, and 6-fractions TCP curves, respectively.

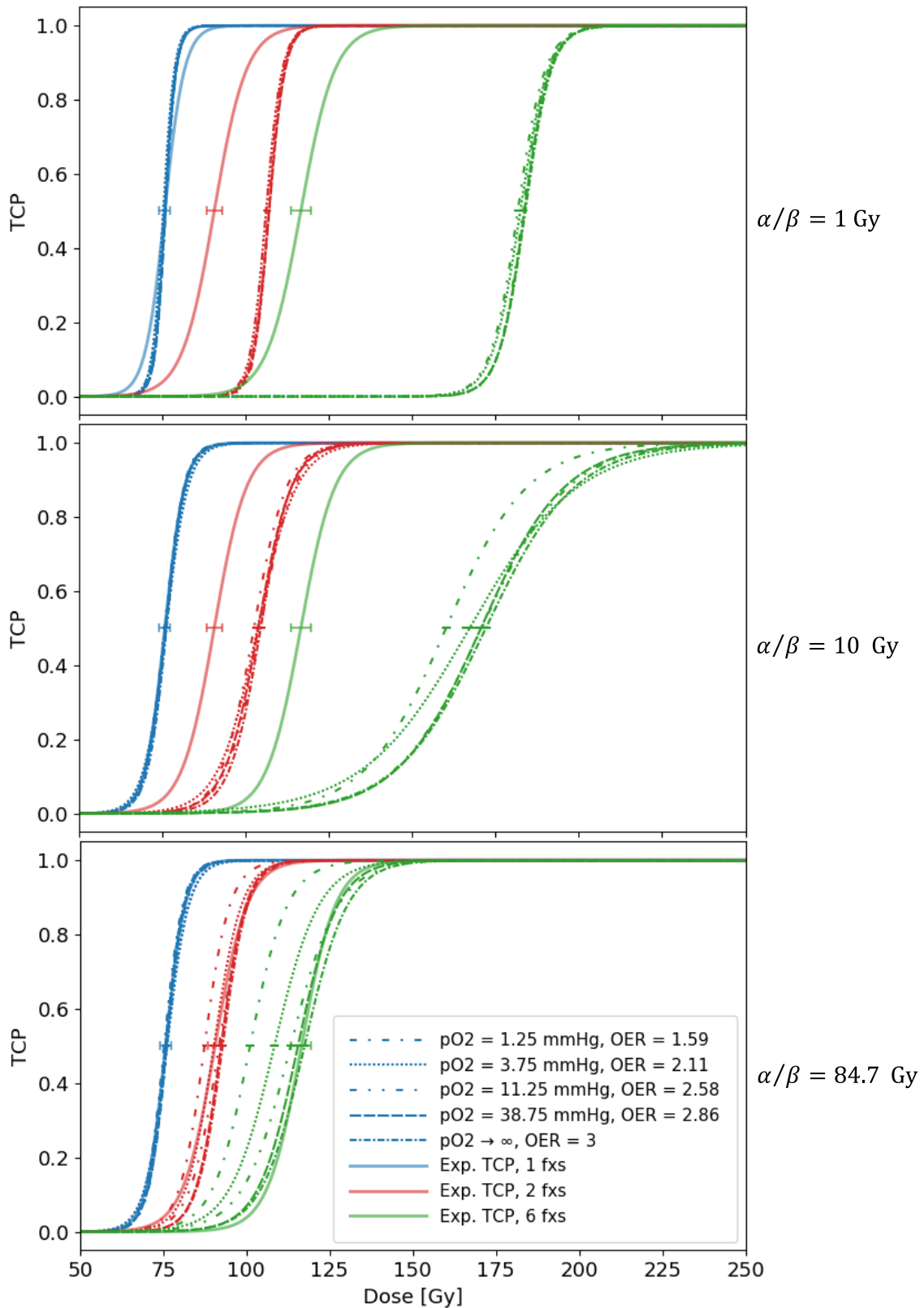


Figure 3.4: TCP curves simulated with the TRM for three α/β values: 1 Gy (top), 10 Gy (centre) and 84.7 Gy (bottom) and for five oxygenation conditions. The parameters α and σ_α were fitted to reproduce the experimental 1-fraction TCP curve for the AT1 tumour subline. The experimental curves for 1, 2, and 6 fractions are also shown. Error bars (1 SD) are shown for the value of D_{50} . Additional TRM input parameters used for these simulations are summarised in Table 2.4.

3.3 Adjustment to experimental *in-vivo* data

3.3.1 Experimental tumour parameters

Based on the experimental growth data shown in Figure 2.13, Gompertz growth curves were fitted using equation (2.20), from which the VDT was obtained for each tumour subline. The fitted curves are shown in Figure 3.5. Additionally, the values of ρ_C and ρ_{NC} were calculated as described in section 2.4.1 and are summarised in Table 3.2 along with the VDT.

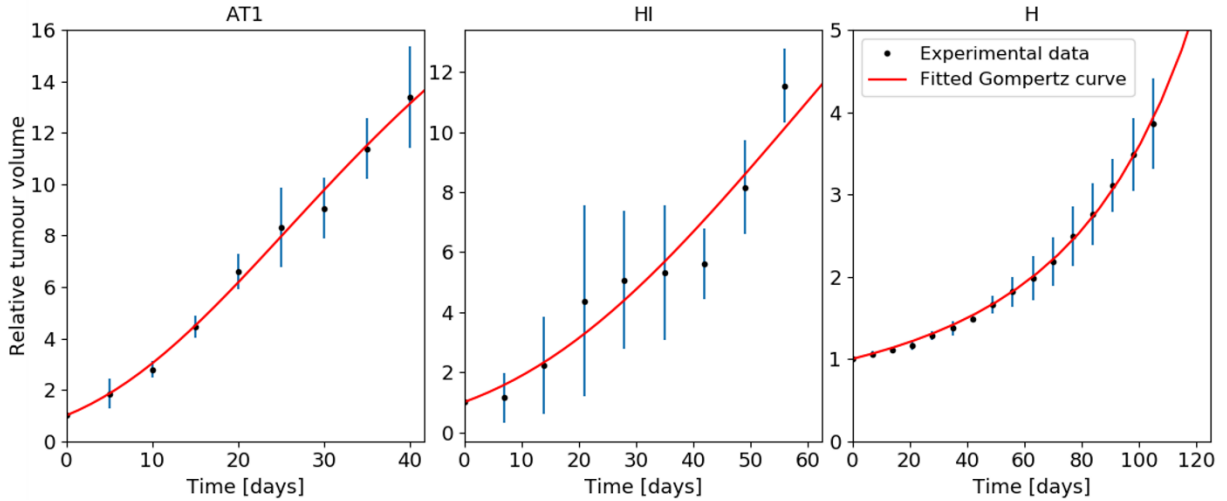


Figure 3.5: Measured relative tumour volume as a function of time and fitted Gompertz curves for the tumour sublines AT1 (left), HI (centre) and H (right). The error bars correspond to one standard error.

Table 3.2: VDT, total cell density ρ_C and tumour cell density ρ_{TC} for the three experimental tumour sublines.

Tumour subline	VDT \pm SD [hours]	$\rho_C \pm$ SD [cells/mm ³]	CK19+ [%] [55]	$\rho_{TC} \pm$ SD [cells/mm ³]
AT1	121.7 \pm 5.7	593634 \pm 69558	77.7	461253 \pm 54046
HI	239.3 \pm 41.0	458423 \pm 82441	87.1	399286 \pm 71807
H	1919.5 \pm 49.3	465413 \pm 81674	34.5	160567 \pm 28177

3.3.2 AT1 tumour subline

The first tumour subline studied in the parameter adjustment of the TRM was the AT1. Simulations were performed as described in section 2.4.3, with input parameters as specified in Table 2.5. The tumour-specific VDT and cell densities were taken from section 3.3.1.

The parameters α and σ were fitted to reproduce the experimental 1-fraction TCP curve, and the AQM was calculated based on the 2- and 6-fractions TCP curves, following the procedure

described in section 2.4.2 and Figure 2.16. To find the minimum value of AQM, simulations were performed for different α/β , ranging from 1 Gy to the experimental $\alpha/\beta_{eff}^{exp} = 84.7$ Gy. As the AQM approached its minimum value, the sampling of α/β was refined. This procedure was repeated for the three oxygenation conditions studied: Severe hypoxia, mild hypoxia, and well-oxygenated, with VF_0 1%, 3%, and 5%, respectively. The obtained AQM values are shown in Figure 3.6.

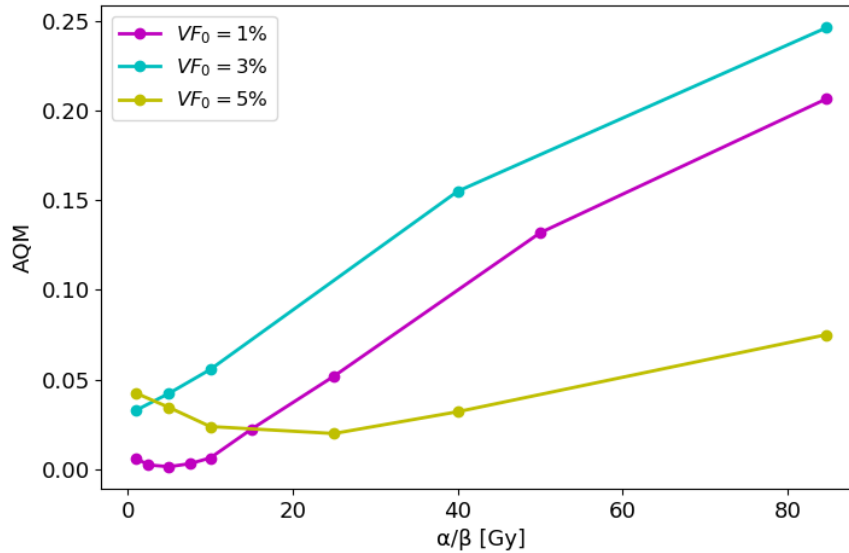


Figure 3.6: AQM as a function of α/β for the AT1 tumour subline, for the three oxygenation conditions studied. Simulations were performed as described in section 2.4.3, with all TRM biological processes turned on, and additional input parameters are specified in Table 2.5.

The minimum AQM for the VF_0 3% and 5% was found to be at least one order of magnitude larger than for VF_0 1%. The minimum AQM value was 1.29×10^{-3} for VF_0 1% and $\alpha/\beta = 5$ Gy, with adjusted $\alpha = 0.055$ Gy^{-1} and $\sigma = 0.044$ Gy^{-1} . The corresponding simulated TCP curves are shown in Figure 3.7, along with the experimental curves. From these results, it was possible to identify firstly, that there were still noticeable deviations between the simulated and experimental TCP curves for the minimum AQM shown in Figure 3.7, and secondly that the TCP curves of tumours with VF_0 3% and 5% were located at much too low doses after the first fraction, resulting in 2-fraction TCP curves at similar and even lower doses than for 1 fraction. As an example of the latter effect, the results for the minimum AQM at VF_0 3% and 5%, with $\alpha/\beta = 1$ Gy and 25 Gy respectively, are shown in Figure 3.8. Motivated by these two observations, the impact of the different TRM components on the TCP curves was studied for VF_0 3% and $\alpha/\beta = 10$ Gy, by keeping the radiation-induced cell kill turned on and turning on one additional biological process at a time. Besides the six core biological processes (see section 2.2.4), the influence of the DF in the selection of the oxygen histogram, termed as “DF influence”, was also studied (see TOM, section 2.2.3). The resulting TCP curves are shown in Figure 3.9, which were all simulated for VF_0 3% and $\alpha/\beta = 10$ Gy, and adjusted $\alpha = 0.084$ Gy^{-1} and $\sigma_\alpha = 0.051$ Gy^{-1} .

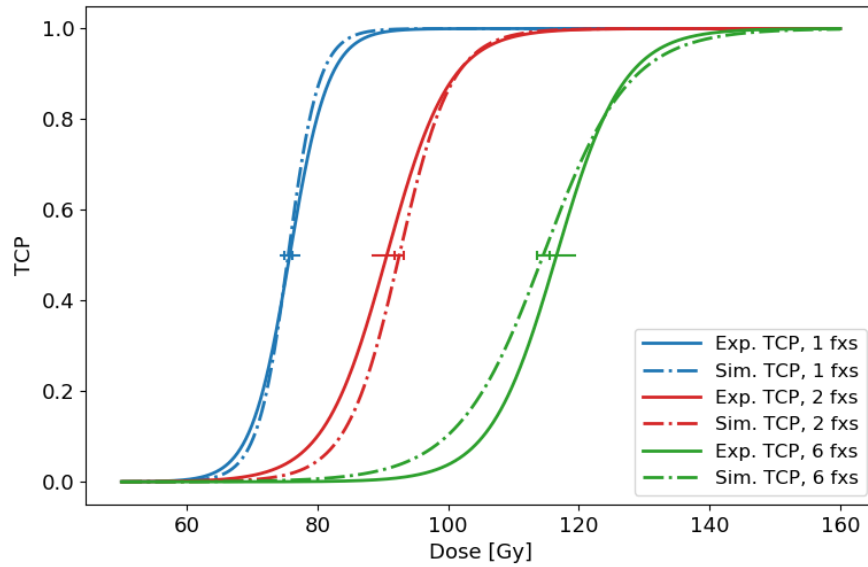


Figure 3.7: Simulated TCP curves (dash-dotted lines) for the minimum AQM. The related parameter adjustment led to the best fit of the experimental TCP curves for the AT1 tumour subline (solid lines). The simulated curves were obtained for $VF_0 = 1\%$ (severe hypoxia), $\alpha/\beta = 5$ Gy, and adjusted $\alpha = 0.055$ Gy⁻¹ and $\sigma_\alpha = 0.044$ Gy⁻¹, with all the TRM biological processes turned on. Additional TRM input parameters are specified in Table 2.5.

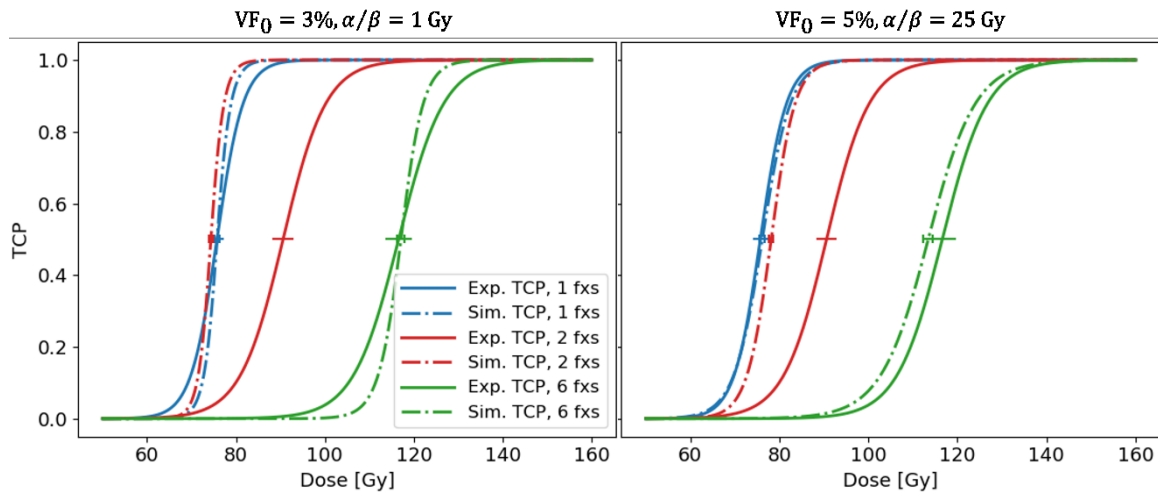


Figure 3.8: Simulated TCP curves (dash-dotted lines) obtained for the minimum AQM (see Figure 3.6) for $VF_0 = 3\%$ (mild hypoxia, left) and $VF_0 = 5\%$ (well-oxygenated, right). In both cases, the curves for 2 and 6 fractions deviate significantly from the AT1 experimental TCP curves (solid lines). For these simulations, all the TRM biological processes were turned on. Additional TRM input parameters are specified in Table 2.5.

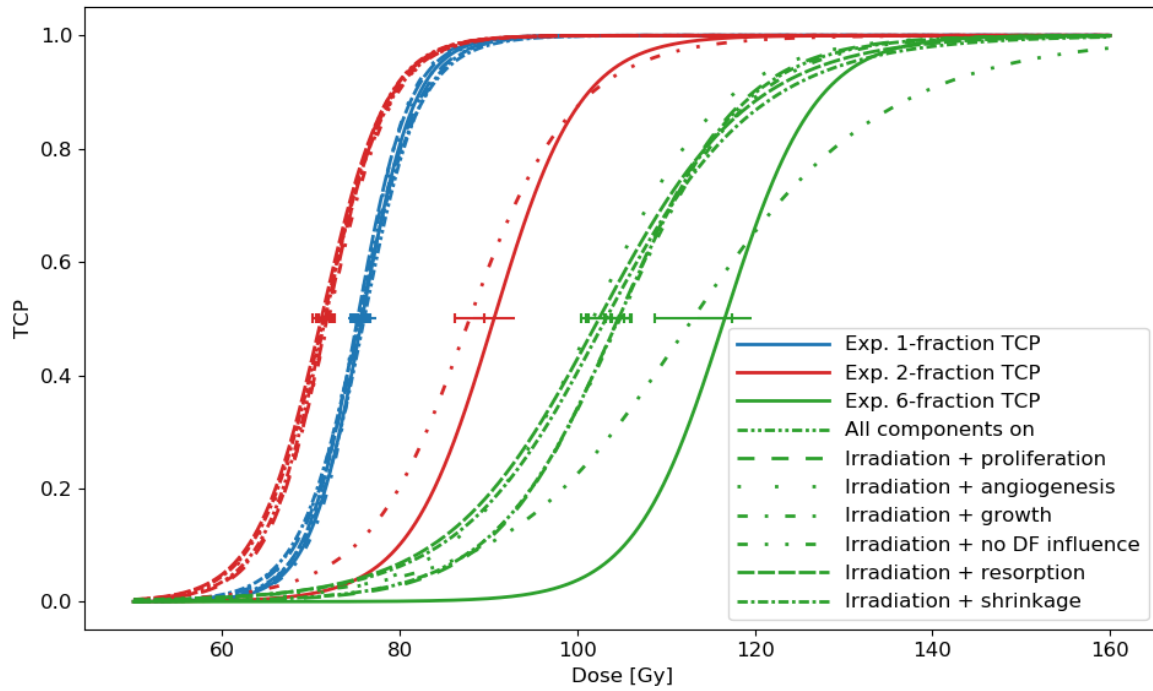


Figure 3.9: Simulated TCP curves with different TRM biological components turned on for $VF_0 = 3\%$ and $\alpha/\beta = 10 \text{ Gy}$, and with $\alpha = 0.084 \text{ Gy}^{-1}$ and $\sigma_\alpha = 0.051 \text{ Gy}^{-1}$ adjusted to reproduce the 1-fraction TCP curve. The experimental TCP curves are shown in solid lines. Additional TRM input parameters are specified in Table 2.5.

As shown in Figure 3.9, no significant differences in D_{50} were found between the results with all TRM components turned on and with the different combinations of biological effects, except for the DF influence on the oxygen histograms (*i.e.*, the assumption that DCs do not consume oxygen). In the case where the DCs were assumed to consume oxygen, the 2- and 6-fraction TCP curves shifted to higher doses in comparison to all the other simulated cases shown in Figure 3.9. Based on these observations, the parameter adjustment was repeated entirely, removing the DF influence on the oxygen histograms, *i.e.*, with the new assumption that DCs consume oxygen. The obtained AQM as a function of α/β for this parameter adjustment is shown in Figure 3.10. A minimum AQM was found for all oxygenation conditions, in contrast to the previous adjustment where no minimum AQM was found for the mild hypoxia case ($VF_0 = 3\%$ in Figure 3.6). The minimum AQM value was 1.03×10^{-3} and was obtained for $VF_0 = 3\%$ and $\alpha/\beta = 5 \text{ Gy}$, with adjusted $\alpha = 0.046 \text{ Gy}^{-1}$ and $\sigma_\alpha = 0.037 \text{ Gy}^{-1}$. The corresponding simulated TCP curves are shown in Figure 3.11.

The performed parameter adjustment assuming that DCs consume oxygen resulted in a slight decrease on the minimum AQM of 2.63×10^{-4} with respect to the previously obtained value when assuming DCs do not consume oxygen. The impact of this reduction on the simulated TCP curves in both scenarios is illustrated in Figure 3.8 and Figure 3.11, respectively. In both cases, deviations between simulated and experimental 2-fraction TCP were obtained: For the 2-fraction TCP, $D_{50} = 92.5 \pm 0.7 \text{ Gy}$ when considering that DCs do not consume oxygen, and $88.5 \pm 0.7 \text{ Gy}$

assuming DCs do consume oxygen (see Figure 3.8 and Figure 3.11, respectively), while for the experimental 2-fraction TCP curve, $D_{50} = 90.6 \pm 2.6$ Gy (see Table 2.2) was obtained. In addition, a better adjustment of the 6-fraction TCP was achieved when the DCs were assumed to consume oxygen. This case resulted in $D_{50} = 116.2 \pm 1.7$ Gy, compared to the experimental 6-fraction value $D_{50} = 116.6 \pm 3.0$ Gy.

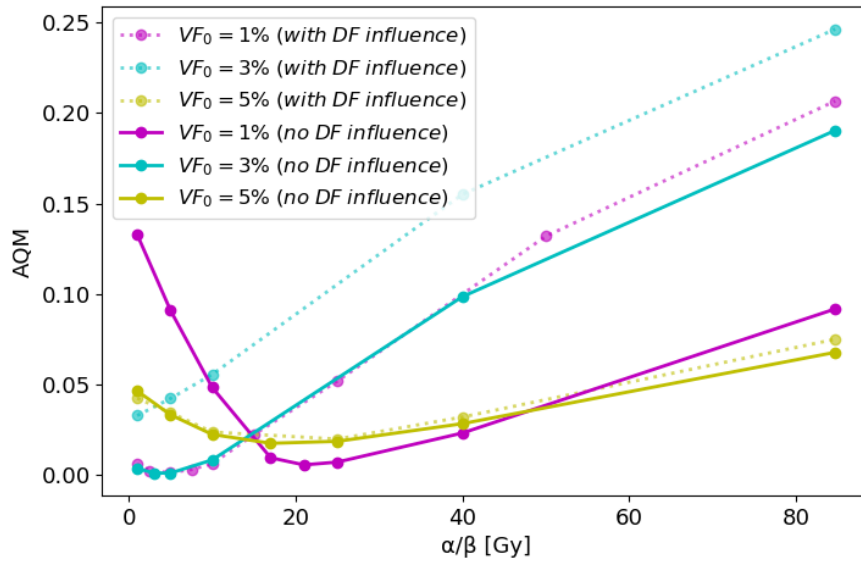


Figure 3.10: AQM as a function of α/β for the AT1 tumour subline obtained for the three oxygenation conditions studied. Simulations were performed as described in section 2.4.3, with all TRM biological processes turned on except for the DF influence on the oxygen histogram selection (solid lines). For comparison, the results obtained including the DF influence are also shown (dotted lines). Additional input parameters are specified in Table 2.5.

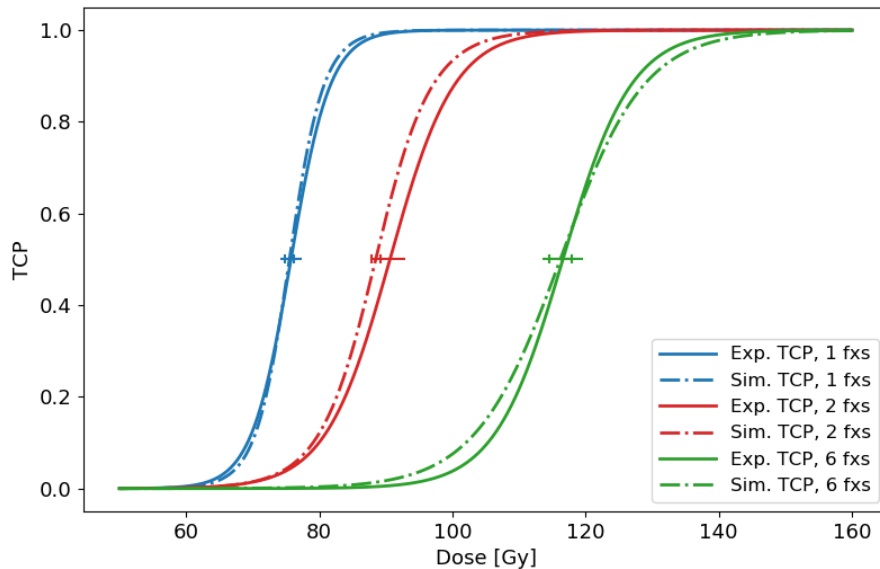


Figure 3.11: Simulated TCP curves (dash-dotted lines) for the minimum AQM for the parameter adjustment to the AT1 experimental TCP curves (solid lines). The simulated curves were obtained for $VF_0 = 3\%$ (mild hypoxia), $\alpha/\beta = 5$ Gy, and adjusted $\alpha = 0.047 \text{ Gy}^{-1}$ and $\sigma_\alpha = 0.037 \text{ Gy}^{-1}$, with all the TRM biological processes turned on except for the DF influence on histogram selection (*i.e.*, assuming DCs do consume oxygen). Additional TRM input parameters are specified in Table 2.5.

3.3.3 HI tumour subline

The TRM parameter adjustment was conducted for the HI tumour subline following the same procedure as for the AT1 subline, without the DF influence on the oxygen histogram selection, *i.e.*, assuming that DCs consume oxygen. The AQM was determined for α/β in the range from 1 Gy to 87.7 Gy, corresponding to α/β_{eff}^{exp} (see Table 2.2), and the results are shown in Figure 3.12.

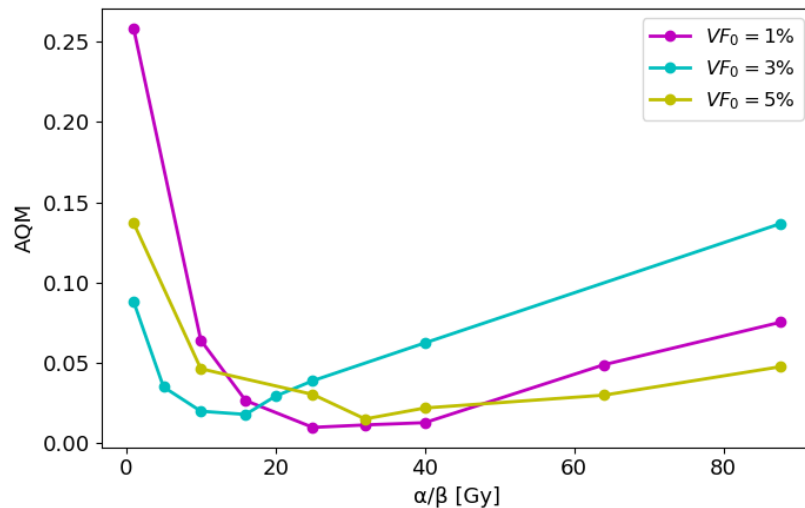


Figure 3.12: AQM as a function of α/β for the HI tumour subline obtained for the three oxygenation conditions studied. Simulations were performed as described in section 2.4.3, with all TRM biological processes turned on except for the DF influence on the oxygen histogram selection. Additional input parameters are specified in Table 2.5.

A minimum AQM was found in the α/β -range studied for the three oxygenation conditions studied. The overall minimum AQM was 9.8×10^{-2} for $VF_0 = 1\%$ and $\alpha/\beta = 25$ Gy and the corresponding TCP curves are shown in Figure 3.13.

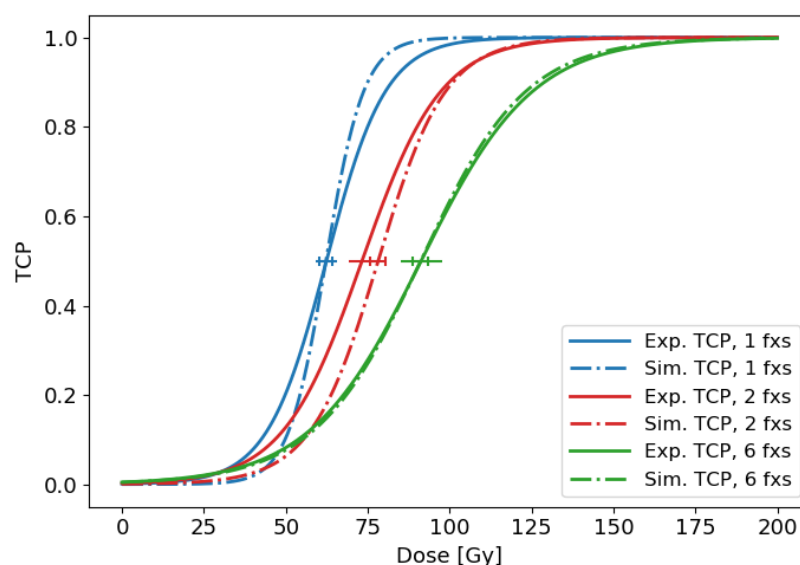


Figure 3.13: Simulated TCP curves (dash-dotted lines) for the minimum AQM for the parameter adjustment to the HI experimental TCP curves (solid lines). The simulated curves were obtained for $VF_0 = 1\%$ (severe hypoxia), $\alpha/\beta = 25$ Gy, and adjusted $\alpha = 0.265 \text{ Gy}^{-1}$ and $\sigma_\alpha = 0.212 \text{ Gy}^{-1}$, with all the TRM biological

processes turned on except for the DF influence on histogram selection (*i.e.*, assuming DCs do consume oxygen). Additional TRM input parameters are specified in Table 2.5.

3.3.4 H tumour subline

The TRM parameter adjustment was conducted for the H tumour subline following the same procedure as for the other two sublines. Taking into account the results obtained for the AT1 tumour subline, the adjustment was carried out without the DF influence on the oxygen histogram selection, *i.e.*, assuming DCs consume oxygen. The AQM was determined for α/β in the range from 0.4 Gy, corresponding to α/β_{eff}^{exp} (see Table 2.2), to 40 Gy, and the results are shown in Figure 3.14 for the three oxygenation conditions considered. For $VF_0 = 1\%$ and 5% , AQM decreased until the lowest value of the studied α/β -range. For $VF_0 = 3\%$, a minimum AQM of 0.12 was obtained for $\alpha/\beta = 1$ Gy. However, neither this minimum nor any of the different VF_0 - α/β combinations allowed reproducing the experimental results, and as a consequence, all AQM values resulted to be two orders of magnitude larger than those obtained in the adjustment for the AT1 subline. As an example, the simulated TCP curves for the minimum AQM for $VF_0 = 1\%$ and 3% , for α/β 0.4 Gy and 1 Gy respectively, are shown in Figure 3.15.

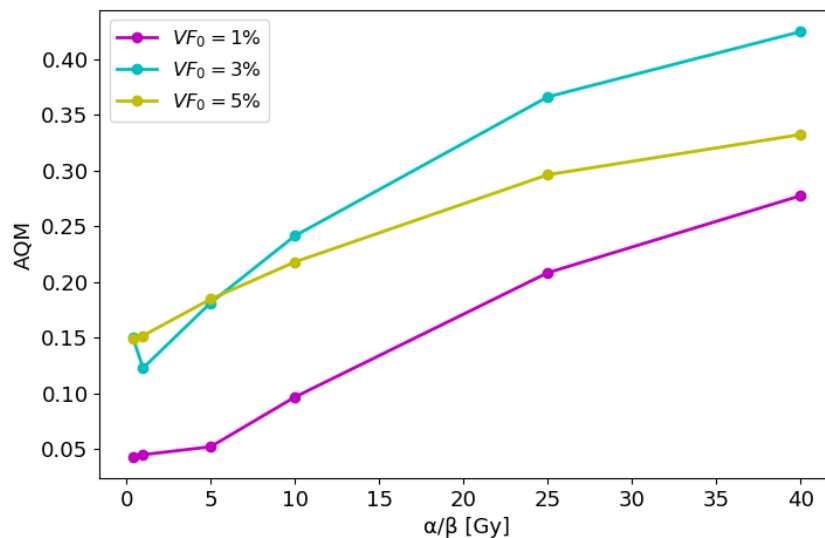


Figure 3.14: AQM as a function of α/β for the H tumour subline, for the three oxygenation conditions studied. Simulations were performed as described in section 2.4.3, with all TRM biological processes turned on except for the DF influence on the oxygen histogram selection. Additional input parameters are specified in Table 2.5.

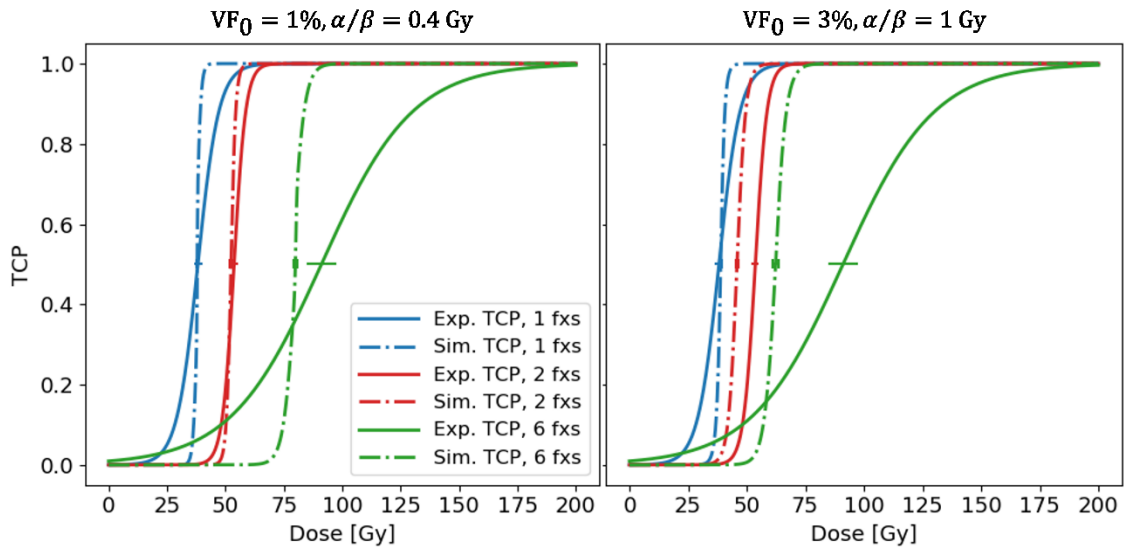


Figure 3.15: Simulated TCP curves (dash-dotted lines) obtained for $VF_0 = 1\%$ (severe hypoxia, left) and $VF_0 = 3\%$ (mild hypoxia, right) for the parameter adjustment to the H subline experimental TCP curves (solid lines). For these simulations, all the TRM biological processes were turned on except for the DF influence on the oxygen histogram selection. Additional TRM input parameters are specified in Table 2.5.

As shown in Figure 3.15, none of the VF_0 - α/β combinations corresponding to the minimum AQM for $VF_0 = 1\%$ and 3% allowed reproducing the experimental TCP curves. Based on these results, it was evident that the TCP curves needed to be shifted to higher doses as the number of fractions increased, *i.e.*, the fractionation effect needed to be larger (see Figure 2.2). Based on equation (2.11), the fractionation effect may be increased by increasing the OER, which in this case is achieved by increasing VF_0 . Hence, for the well-oxygenated condition, $VF_0 = 7\%$ and 10% were additionally considered for the adjustment to the experimental curves using an α/β -range from 0.4 Gy to 15 Gy. The resulting AQM is shown in Figure 3.16, where it can be seen that very similar results were obtained for $VF_0 = 7\%$ and 10% , with a minimum AQM at $\alpha/\beta = 8$ Gy in both cases. The minimum AQM over all VF_0 was 1.89×10^{-2} at $VF_0 = 7\%$, 7.36×10^{-4} below the minimum AQM obtained for $VF_0 = 10\%$. The TCP curves for $VF_0 = 7\%$ are shown in Figure 3.17.

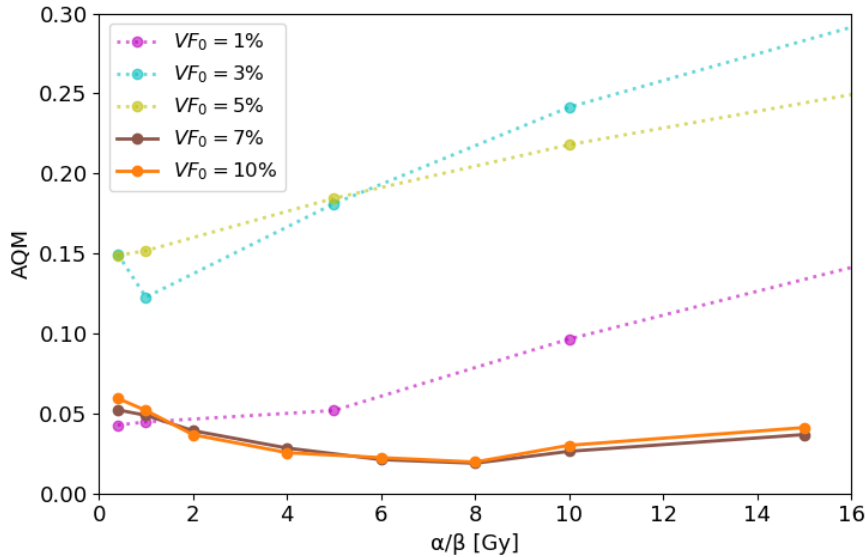


Figure 3.16: AQM as a function of α/β for the H tumour subline using additionally $VF_0 = 7\%$ and 10% (solid lines) as parameter setting for well-oxygenated conditions. Simulations were performed as described in section 2.4.3, with all TRM biological processes turned on except for the DF influence on the oxygen histogram selection. For comparison, the previous results obtained with lower VF_0 are also shown (dotted lines) in the α/β -range from 0.4 Gy to 15 Gy. Additional input parameters are specified in Table 2.5.

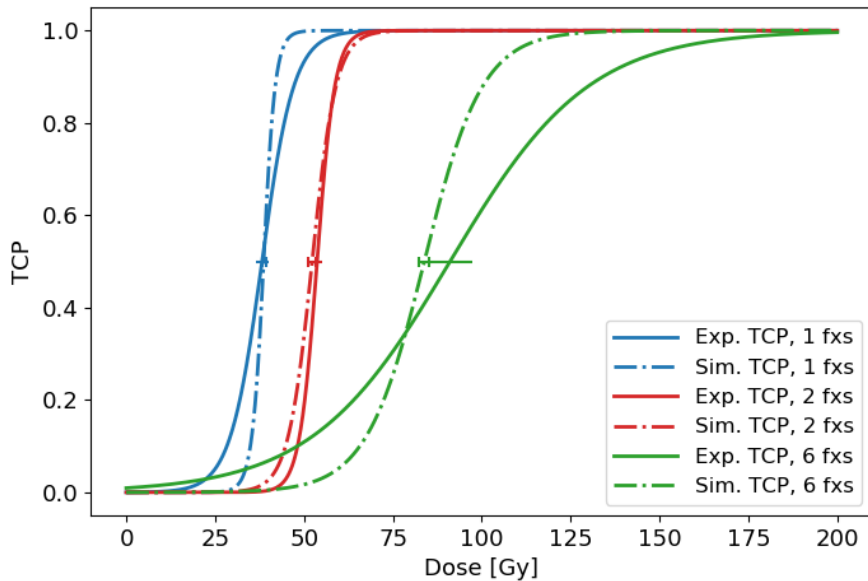


Figure 3.17: Simulated TCP curves (dash-dotted lines) for the minimum AQM for the parameter adjustment to the H experimental TCP curves (solid lines). The simulated curves were obtained for $VF_0 = 7\%$ (well-oxygenated), $\alpha/\beta = 8$ Gy, and adjusted $\alpha = 0.096$ Gy⁻¹ and $\sigma_\alpha = 0.092$ Gy⁻¹, with all the TRM biological processes turned on except for the DF influence on histogram selection (*i.e.*, assuming DCs do consume oxygen). Additional TRM input parameters are specified in Table 2.5.

3.3.5 Summary of adjusted parameters

This section summarises the parameters obtained from the adjustment of the TRM to the experimental data that has been performed in the previous sections (3.3.2, 3.3.3, and 3.3.4). In addition, the values of D_{50} and the slope, $TCP'(D_{50})$, of the TCP curves are displayed and

compared to the experimental values. The adjusted TCP curves are displayed in Figure 3.11 for the AT1-, in Figure 3.13 for the HI-, and in Figure 3.17 for the H-tumour subline.

Table 3.3: Parameters adjusted to reproduce the experimental TCP curves with the TRM for the three tumour sublines studied.

Subline	VF ₀ [%]	α/β [Gy]	α [Gy ⁻¹]	σ_α [Gy ⁻¹]
AT1	3	5	0.047	0.037
HI	1	25	0.265	0.212
H	7	8	0.096	0.092

Table 3.4: D_{50} and $TCP'(D_{50})$ for the simulated TCP curves that reproduce the experimental data for the three tumour sublines studied (see section 2.4.1). The simulations were performed with the adjusted parameters specified in Table 3.3. Additional input parameters are specified in Table 2.5.

Subline	Parameter	Method	Fractions		
			1	2	6
AT1	$D_{50} \pm SD$ [Gy]	Simulation	75.5 ± 0.7	88.5 ± 0.7	116.2 ± 1.7
		Experiment	75.7 ± 1.6	90.6 ± 2.3	116.6 ± 3.0
	$TCP'(D_{50}) \pm SD$ [Gy ⁻¹]	Simulation	0.100 ± 0.017	0.060 ± 0.012	0.040 ± 0.005
		Experiment	0.08411	0.04871	0.02064
HI	$D_{50} \pm SD$ [Gy]	Simulation	62.2 ± 2.1	78.2 ± 2.3	91.2 ± 2.3
		Experiment	62.4 ± 3.2	73.2 ± 4.0	91.3 ± 6.3
	$TCP'(D_{50}) \pm SD$ [Gy ⁻¹]	Simulation	0.045 ± 0.003	0.025 ± 0.003	0.016 ± 0.002
		Experiment	0.02754	0.02064	0.01460
H	$D_{50} \pm SD$ [Gy]	Simulation	38.7 ± 0.5	52.3 ± 1.2	83.8 ± 1.5
		Experiment	38.2 ± 1.8	53.7 ± 1.5	93.0 ± 6.3
	$TCP'(D_{50}) \pm SD$ [Gy ⁻¹]	Simulation	0.160 ± 0.039	0.076 ± 0.011	0.031 ± 0.004
		Experiment	0.05554	0.09985	0.01279

Table 3.5: Comparison of α/β_{eff}^{exp} , corresponding to the experimentally-obtained value, and α/β , obtained from the parameter adjustment.

Subline	AT1	HI	H
α/β [Gy]	5	25	8
$\alpha/\beta_{eff}^{exp} \pm SE$ [Gy]	84.7 ± 13.8	87.7 ± 32.9	0.40

4 Discussion

The discussion of this study follows the structure of the results presented in section 3. First, the validation by analytical calculations is discussed, followed by the interplay of the key input parameters. Then, the adjustment to experimental *in-vivo* data is discussed, also examining the findings regarding the TRM components and their biological significance, as well as the biological interpretation of the adjusted parameter values. The last part covers the limitations of the current study and challenges for future studies with the TRM.

4.1 Validation by analytical calculations

The TRM was validated by comparing the simulated results with those of the LQM, as described in section 2.4.3 and shown in section 3.1 for a fractionated treatment of 35 fractions of 2 Gy and for three tumour radiosensitivity heterogeneities as given by σ_α . The SF curves show that the TRM follows the LQM in all cases, which is an expected result since simulations were performed with only the radiation-induced cell-kill component of the TRM, given by equation (2.10). However, it is important to note that for larger heterogeneities, *i.e.*, larger σ_α , deviations may occur. This is due to the lognormal distribution used to model the radiosensitivity heterogeneity given by equation (2.23), with rising skewness as σ_α increases. In terms of SF curves, as σ_α becomes comparable or larger than α , the sampled radiosensitivity tends to decrease and approaches zero, and therefore deviations of the mean SF from the LQM may occur. Furthermore, an additional stochastic component was introduced to the TRM to sample the TC and CC proliferation, as shown in Figure 3.2. Also, prolonged irradiation breaks and additional biological processes that alter the number of cells were introduced, and therefore the simulated SF curves did not match the results of the LQM anymore. Although the differences were subtle, introducing stochastic cell proliferation to the TRM allows consistent modelling of all the processes that alter the number of cells in the tumour.

As a last step of the analytical validation, TCP curves were simulated and compared with the results of the LQM-based Poisson model, given by equations (2.10) and (2.12) and shown in Figure 3.3. Although the slope of the TCP curves differed, similar D_{50} values were obtained for the TRM with only the irradiation component of the TRM and the LQM-based Poisson model. The different curve shapes were likely caused by the different mathematical models, with the logistic model reaching its maximum steepness at 50% and the Poisson model at 37% [19]. The TCP curves in Figure 3.3, with D_{50} given in Table 3.1, show that each TRM component either sensitises

the tumour or makes it more resistant, and that this strongly depends on the parameter settings of each component.

Overall, the analytical validation indicates that the results obtained with the TRM behave as expected from the main principles described by the LQM. This demonstrates that the formalism used to model the TRM components studied was correctly implemented. The validation was performed using synthetic input parameters without specific biological meaning and assuming homogeneous tumour oxygenation (see Table 2.3), and it is difficult to extend the analytical validation to more complex scenarios due to the lack of ground truth. To assess the TRM performance in such cases, the model reliability and the interplay of the biologically most relevant input parameters was studied.

4.2 The interplay of key input parameters

The interplay between the two main input parameters, OER and α/β , and its impact on the simulated TCP curves, was analysed as described in section 2.4.3 and shown in section 3.2. The TRM results adequately described the TCP variations for the OER- and α/β -values considered in accordance to the OER- α/β relationship given by equation (2.11). These results also show that this finding is valid for a wide range of OER- and α/β -values for the fitted α and σ_α values, indicating that the TRM is reliable in this respect. It is important to note that it is not possible to directly compare the simulated TCP curves with analytical calculations, due to the complexity of the input data used and the inter-tumour radiosensitivity variation. It was only possible to confirm that the range of the simulated D_{50} values agreed well with LQM-based analytical calculations for the OER- α/β combinations studied (data not shown).

The experimental results of the AT1 tumour subline were reproduced in terms of D_{50} , using only the irradiation component in the TRM, with a uniform OER of 2.86 and 3.00, for $\alpha/\beta = \alpha/\beta_{eff}^{exp} = 84.7$ Gy. This result is in agreement with the value in Karger *et al.* [12]: If no additional biological process impacts the tumour response and if only the tumour intrinsic oxygen-independent radiosensitivity is considered to be relevant, a very large α/β is indeed needed to reproduce the TCP curves obtained for the AT1 subline.

4.3 Adjustment to experimental *in-vivo* data

The TRM was adjusted to reproduce experimental *in-vivo* data, as described in section 2.4.2 and shown in section 3.3. The AT1 subline and the findings regarding the TRM components are discussed in the first sections, followed by the HI and H sublines. The remaining sections are

dedicated to the modelling of tumour heterogeneity, the impact of the metrics used for the adjustment, and the biological interpretation of the adjusted parameters.

4.3.1 AT1 tumour subline

The TRM input parameters were adjusted to reproduce the TCP curves for the AT1 tumour subline, as shown in section 3.3.2. The lowest AQM among all tumour sublines was obtained for the AT1 for the two different conditions studied: With DF influence turned on, shown in Figure 3.6, and with DF influence turned off, shown in Figure 3.10. This might have been caused by the homogenous biological features of this subline which is mostly formed by poorly differentiated, anaplastic cells (see Figure 2.14 and [13], [56], [58], [64]). Therefore, the TCP curves are the steepest of all sublines and show similar slopes among the different fractionation schemes. The adjusted parameters allowed reproducing the slope of the TCP curve which results from the remaining tumour heterogeneity for all fractionation schemes, as well as the D_{50} values within one SD of the simulated results (see Table 3.4). The only exception was the slope for the 6-fraction TCP slope, which agreed only within four SD.

Initially, all the TRM components were turned on, including the DF influence on the oxygen histogram selection (see section 2.2.3). A striking observation was the location of the 2-fraction TCP curve for the mild hypoxia and well-oxygenated conditions (VF_0 of 3% and 5%, respectively): The TCP was located at similar and even lower doses than the single fraction curve, as shown in Figure 3.8. Taking into account that the main contributing factor was the DF influence on oxygenation (see Figure 3.9), a plausible explanation for this finding is that TCs at low and intermediate oxygen levels exhibited decreased radiosensitivity compared to the well-oxygenated TCs. After the first fraction, predominantly well-oxygenated TCs died, which increased the DF and correspondingly oxygen became available in the same proportion, as DCs were assumed not to consume oxygen. As a result of the better oxygenation, the radiosensitivity increased and more TCs died after the second fraction, which increased the DF and the available oxygen even further. This means that the tumours were considerably more sensitive at the second fraction than at the first. Accordingly, the reoxygenation effect observed for the 2-fraction scheme did not impact the 6-fraction TCP curves to the same extent. This may be explained by two different mechanisms: On the one hand, the reduced dose per fraction led to reduced DF for the 6-fraction scheme, resulting in reduced reoxygenation caused by the DF influence. On the other hand, the tumours may have been already well-oxygenated after a very small number of fractions. It should be noted that the differences observed with the DF influence turned on and off are important only when higher doses per fraction are delivered, *i.e.*, for larger DF, but not for conventional fraction sizes of 2 Gy, as discussed in the following section.

4.3.2 Cell death and oxygen availability

The results obtained for the AT1 subline (see section 3.3.2), show that when a few, but more than one, fractions are delivered, the resulting high doses per fraction cause significant reoxygenation, which discontinuously changes the radiosensitivity. For the AT1 subline, this effect was striking for the 2-fraction experiment, and for two of the three oxygenation conditions considered (mild hypoxia and well-oxygenated, see Figure 3.8).

In the TRM as initially implemented by Espinoza [9], [10], TCs killed by radiation were assumed to immediately abort cell metabolism, including the consumption of oxygen. Under this assumption, the oxygen that was previously consumed by DCs becomes available for the remaining TCs to consume, thereby increasing their radiosensitivity. Based on the problems with the parameter adjustment for the AT1 tumour subline, especially for the 2-fraction TCP curve, this initial assumption was discarded and replaced by the assumption that DCs continue to consume oxygen until they are resorbed. This *ad hoc* assumption prevented abrupt changes of the oxygen availability after irradiation and as a result, the adjustment of the AT1 TCP curves was possible for all three fractionation schemes, as well as for the other two tumour sublines.

From the radiobiological point of view, this new assumption can be explained as follows: While the effect of radiotherapy originates from the inactivation of TC proliferation leading finally to cell death, this inactivation is known to take place not immediately after irradiation. In cell experiments, it is observed that cells irradiated with x-rays may undergo several mitoses until daughter cells eventually die [65]. This implies that initial radiation-induced DNA damage becomes effective in terms of cell kill only after several cell cycles. This more detailed view on radiation-induced cell kill indicates that irradiated cells, although damaged, are still metabolically active over a limited period of several days. This biologically justifies the newly introduced assumption that DCs continue to consume oxygen for a limited period until they are resorbed.

Adjusting the TRM parameters to reproduce the tumour response to highly hypofractionated treatments led to the implementation of the new assumption on cell death and oxygen availability. In contrast, a parameter adjustment to conventional treatments with considerably lower doses per fraction would not have led to discarding the initial assumption, as supported by the results of the analytical validation. As shown in Figure 3.3 and Table 3.1, the reoxygenation driven by the DF influence was only minimal: No significant difference in the D_{50} value was observed when the DF influence was included in the TRM, in comparison to the D_{50} value obtained with only the irradiation component in the TRM turned on.

4.3.3 HI and H tumour sublimes

The TRM was also adjusted to reproduce the experimental results of the HI and H tumour sublimes, as shown in sections 3.3.3 and 3.3.4, with all TRM components turned on except for the DF influence. The minimum AQM obtained for these sublimes was one order of magnitude larger than that for the AT1, which reflects the larger deviations observed in the TCP curves (see Figure 3.13 and Figure 3.17). The HI subline exhibits rather shallow TCP curves for the three fractionation schemes, with less-optimal fitting for the 1- and 2-fraction TCP curves. For the H subline, the slope could not be perfectly adjusted for the 1- and 6-fraction TCP curves. Contrary to the AT1 subline, the HI shows a mixture of TCs and NCs, which leads to a larger inter-tumour heterogeneity, whereas the H subline is mostly composed of NCs and only a few TCs [13], [66]. Likewise, the three sublimes also show different patterns of perfusion, capillary structure and hypoxic regions, as shown in Figure 2.14 [56]. In the following section, the tumour heterogeneity and its impact on the TRM parameter adjustment are further discussed.

Regarding the H tumour subline, the parameter adjustment was not possible for the oxygenation conditions considered for the other two sublimes, defined by VF_0 of 1%, 3% and 5% (see section 2.4.3). A larger fractionation effect, governed by equation (2.11), was achieved by increasing VF_0 to 7% and 10%, with corresponding initial oxygen histograms shown in Figure 2.17. The resulting AQM turned out to be very similar for the additional VF_0 values and the minimum AQM was obtained for VF_0 7%, as shown in Figure 3.16. The oxygenation condition “well-oxygenated” was initially described by VF_0 5%, motivated by the fact that the corresponding initial oxygen histogram shows a HF close to zero. For comparison, the oxygen histograms for VF_0 5% and 7% are shown in Figure 4.1. Considering the established pO_2 -OER relationship (see equation (2.9) and Figure 2.4), the main OER difference between these histograms lies in the intermediate pO_2 range. In contrast, the difference at higher pO_2 values between VF_0 7% and 10% (see Figure 2.17) did not lead to significant changes in the tumour response, reflected in the similar AQM values obtained for the H subline (see Figure 3.16). The results of the parameter adjustment for the H subline then support previous findings of the reduced predictive power of the HF alone and the necessity to consider the whole tumour oxygenation [47], [67], [68]. Although the oxygen histograms do not provide information about the spatial pO_2 distribution, they are assigned voxel-wise in the TRM and this implementation has shown to impact the tumour response.

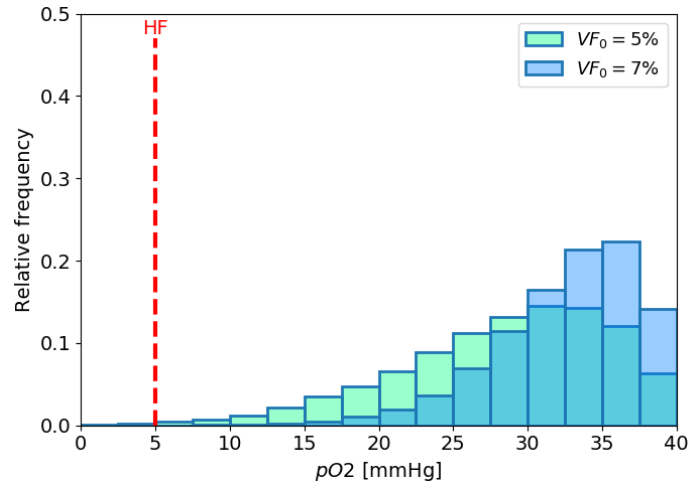


Figure 4.1: Superposition of the oxygen histograms for the "well-oxygenated" condition, for the initially used $VF_0 = 5\%$ and the additionally considered $VF_0 = 7\%$ (shown in separate plots in Figure 2.17), used for the parameter adjustment of the H tumour subline.

4.3.4 Modelling of tumour heterogeneity

The variation in tumour heterogeneity among patients is currently understood as the cause of shallow TCP slopes [19]. This variation is accounted for in the TRM by sampling the radiosensitivity for each simulated tumour, using a lognormal probability distribution (see equation (2.23) in section 2.2.4). For the AT1 subline, the adjustment of the 1-fraction TCP curve was achieved in terms of the D_{50} and $TCP'(D_{50})$ within the range of one SD, as mentioned in section 4.3.1, but for the HI and H sublines, this was not the case. For both sublines, it was not possible to fit the parameters α and σ_α to reproduce the 1-fraction TCP curve, and especially the slope, to the same extent as for the AT1. From the fitting for the 1-fraction curve, large values of σ_α were obtained for the three sublines, and in the case of the HI and H sublines, further increase in σ_α did not lead to a further decrease of the slope. This is an indication that modelling the tumour response heterogeneity solely based on the inter-tumour radiosensitivity variation might have certain limitations and that additionally, the intra-tumour radiosensitivity variation may be important. Technically, it would be feasible to include intra-tumour heterogeneities similarly into the simulation. However, this implementation would result in an additional parameter, which would have to be fitted to outcome data. Finally, it should be considered that the experimental dose-response curves used as a reference for the TRM simulations also represent only estimates of the true TCP curve, as they were determined from a limited number of animals. Despite these limitations, the parameter adjustment still provides useful insights into the biological processes that might impact the tumour response to radiation.

4.3.5 Impact of the choice of OF and AQM

The parameter adjustment was performed step-wise and based on two quantities: OF and AQM (see section 2.4.3). These metrics were chosen to compare the simulation results with the experimental TCP curves. Consequently, the selection of these metrics directly impacts the adjusted parameters.

Fitting α and σ_α based on the 1-fraction TCP curves allowed to separately determine these two parameters, under the assumption that the tumour radiosensitivity and its inter-patient heterogeneity, determined by α and σ_α respectively, are the only parameters that impact the position and slope of this curve. As the position and the slope of the simulated TCP curve needed to be adjusted, the OF was composed of equally-weighted summed squared differences of three reference doses (D_{50} , D_{20} and D_{80}) of the curve: D_{50} describing the position, and D_{20} and D_{80} describing the slope (equation (2.26)). On the other side, the AQM was the metric for finding the best combination of VF and α/β (and for readjusting α and σ_α to maintain the fit to the 1-fraction TCP curve) to reproduce the 2- and 6-fraction TCP curves. For this metric, the squared differences at 20% and 80% TCP were weighted by a factor of 0.5, to assign equal weights to the parameters related to the TCP curve position (D_{50}) and slope (D_{20} and D_{80}). Additionally, all differences were normalised by the experimental value to account for the larger absolute doses of the 2- and 6-fraction TCP curves, respectively. If different weights were given to the reference doses in OF or AQM, or if OF and AQM were defined differently, the adjusted parameters would also be expected to differ from those obtained in this study. Nonetheless, based on the reasoning underlying the metric definition, the applied definition of OF and AQM appears appropriate.

Alternatively to the step-wise adjustment, the simultaneous optimisation of all parameters could have been considered, with a simultaneous adjustment of all three TRM-simulated TCP curves steered by an adequately redefined AQM. However, this would significantly increase the complexity of the fit and the computation time and might lead to convergence problems. For this reason, the fitting procedure in this study was split into the adjustment of the 1-fraction curve (resulting in α and σ_α) and the adjustment of the 2- and 6-fraction curves (resulting in VF and α/β , and only slightly readjusted α and σ_α).

4.3.6 Biological interpretation of the adjusted α/β

The adjustment performed in section 3.3 resulted in the parameters summarised in Table 3.3. Taking into account the ongoing debate about the α/β value for prostate and the increased use of hypofractionated treatments for prostate cancer [14], [69]–[75], it is worth exploring the biological meaning of the adjusted α/β .

The α/β values for the AT1 and HI sublines obtained from the TRM parameter adjustment were lower than the experimental values reported by Glowa *et al.* [14], as shown in Table 3.5. This can be explained by the fact that the experimental α/β value reflects the effective tumour response to the given fractionation schemes rather than the intrinsic fractionation dependence of isolated cells. As α/β in the TRM is directly associated to the underlying cells, this parameter must be considered as an intrinsic value. In real experiments as well as in the TRM, also other biological processes, such as hypoxia, impact the result of the α/β -adjustment, as shown in Figure 3.3 and Figure 3.9. Besides being hypoxic, the AT1 and HI sublines (see Figure 2.14) are also characterised by a moderate to high growth rate, which for extended overall treatment times results in increased D_{50} and α/β values [14], [73]. The adjustment of the TRM to the experimental TCP curves further supports the hypothesis of increased effective α/β values, but considerably lower intrinsic α/β values defining the repair capacity of the underlying cells.

For the H tumour subline, a larger α/β was found in comparison to the experimental value, which however was still comparable within one order of magnitude with α/β values reported for prostate [69], [70], [72], [73], [75]. With this respect, it has to be noted that for the H tumour subline, the generalised logistic dose-response could not be fitted [14], and α/β was therefore determined by a linear regression using the Douglas-Fowler method [76]. In this method, however, the dependent quantity on the y-axis (reciprocal total isoeffective dose) is not independent of the independent quantity on the x-axis (isoeffective fractional dose), and therefore the uncertainty of α/β cannot be assessed. The low experimental α/β value adjusted for the H subline is most likely a result of the good oxygenation observed in the immunohistochemical samples and was confirmed so far by the α/β adjustment of the TRM simulations. Here, the minimum AQM was obtained for $VF_0 = 7\%$, and considering the relatively narrow distribution of the TCP curves over the dose range, a larger α/β allowed reproducing the results.

Finally, the parameters α/β and α have also been experimentally determined in cell culture for the AT1 tumour cells in the work by von Neubeck [77]. This experimental measurement was performed *in-vitro* for a single dose with a 250 kVp photon beam. Interestingly, the experimentally-determined values are comparable to those obtained from the parameter adjustment of the TRM-simulated TCP curves for the AT1 tumour subline: The obtained parameters were $\alpha = 0.174 \pm 0.052 \text{ Gy}^{-1}$, $\alpha/\beta = 6.8 \pm 0.5 \text{ Gy}$ for the *in-vitro* study in comparison to $\alpha = 0.047 \pm 0.037 \text{ Gy}^{-1}$, $\alpha/\beta = 5 \text{ Gy}$ for the TRM simulations. Considering that the two methods are very different in their methodology, the two parameter sets appear well comparable. This shows that the TRM is a valuable tool to analyse the different biological processes on the overall radiation response of tumours and to separately investigate their contributions.

4.4 Limitations and challenges

Modelling of the radiation-induced cell kill

The core of the TRM is the radiation-induced cell kill as defined by the LQM and modified by the OER to account for the oxygen impact on tumour response (see equation (2.10) and section 2.1.2). The tumour response is then defined by the oxygen-dependent TC survival, as well as by the other biological processes included in the model. The TRM has been validated based on *in-vivo* tumours irradiated at very high doses per fraction (see section 2.4.1), which might impose different challenges to the TRM.

The first challenge implementing the LQM in the TRM is related to the heterogeneity of the tumour tissue, which is not purely composed of TCs. Assigning a unique radiosensitivity to the complete tumour tissue might disregard other types of cells, particularly for highly heterogeneous tumours such as the HI and H sublines (see section 2.4.1). Therefore, the adjusted parameters do not reflect the isolated TC radiosensitivity, but rather the average radiosensitivity over all the cell types found in the tumour.

The second challenge originates from modelling the radiation response of TCs at high doses per fraction using only the LQM [78]. Besides the intrinsic repair capacity of TCs, additional biological processes have been reported to impact the tumour response at high doses per fraction as well. For example, the involvement of the immune response might result in enhanced cell kill [79], [80], and potential vessel damage could further alter the tumour oxygenation which in turn affects the response of TCs. These additional biological processes that alter the tumour response may be considered separately from the LQM. This strategy has already been applied in the implementation of the TRM, and could potentially be extended. For example, a separate radiosensitivity value could be assigned to CCs to reflect the vessel damage at high doses. However, this would come with the cost of an increased number of model parameters to be determined or adjusted. On the other hand, if the repair mechanisms present at high doses per fraction differ from those at conventional doses, the LQM would no longer be valid. Nonetheless, considering there is currently not enough quantitative evidence to prefer an alternative model [21], [81]–[84], the LQM is the best available model to implement in the TRM.

Finally, the TRM implementation of the LQM considers a modified formulation to account for the oxygen effect on tumour response. As a result, the oxygen-dependent cell kill is modelled by equation (2.10), where the dependence of the model on the OER-related parameters is evident. The mechanisms behind the pO_2 -OER relationship are still being studied and the current model is mainly a result of *in-vitro* measurements [36]. The *in-vivo* OER may depend on additional

parameters, such as the dose per fraction and cell-dependent characteristics [85]. The TRM would therefore benefit from an improved OER model, but again this might come with the cost of an increased number of parameters in the model.

Implementation of oxygen histograms

The TRM considers the tumour oxygenation via the oxygen histogram database generated with the TOM, as described in section 2.2.3. At each simulation time step, the histogram is updated based on the VF (previously also on the DF) and different pO_2 values are correspondingly assigned to the TCs. This implementation allows considering a temporally changing microscopic oxygen distribution within each voxel without significant additional computing time. However, this implementation does not account for the oxygen-dependent cell kill for the following fraction: When the highly oxygenated and thus highly radiosensitive TCs are killed, these cells are no longer considered as TCs but as DCs. Therefore, for the following simulation step, the remaining available TCs would have to be considered as being more hypoxic, which would require a different oxygen histogram. Since the current oxygenation model in the TRM does not record which TCs are killed, a similar or even better-oxygenated histogram is assigned instead. The oxygen histogram update therefore leads to instantaneous reoxygenation of the tumour when more than one fraction is delivered.

5 Conclusion

The objective of this thesis was to further improve and validate the tumour response model (TRM) previously developed by Espinoza *et al.* [9], [10]. The TRM was validated by analytical calculations to test the various modelled radiobiological processes. This validation confirmed the correct implementation of the different components, in particular of the linear quadratic model (LQM), modified to consider the oxygen enhancement ratio (OER). Together, these components consistently describe the oxygen-dependent response of tumours.

To understand the interaction of effects between the OER and the LQM-parameter α/β , the TRM simulations were studied for different settings of OER and α/β . The variations of the dose-response curves for the different OER- α/β parameter settings showed a larger fractionation effect for larger OER and for smaller α/β . This in turns demonstrates a reliable implementation of the OER- α/β relationship also when more complex input data is used for the simulations.

This is the first study where the multi-scale oxygen-dependent TRM was applied to reproduce *in-vivo* data. For this, three sublines of the Dunning R3327 rat prostate carcinoma (-AT1, -HI, and -H) were used, which differ in cell differentiation, growth rate and oxygenation status. This thesis has shown that the TRM can be adjusted to reproduce the radiation response of these tumours for different fractionation schemes. As a result, the following conclusions can be drawn:

- i) The assumption that tumour cells killed by radiation do not consume oxygen was not compatible with the comparison of the simulated and experimental dose-response curves. This assumption was successfully replaced by assuming that dead cells continue to consume oxygen until they are resorbed.
- ii) The concept of considering the impact of oxygenation by oxygen histograms when modelling the tumour response to radiation is supported by the simulation results.
- iii) The study reveals that intrinsic α/β values are lower than the experimental α/β values and the differences can be explained by the influence of additional biological processes that impact the tumour response to radiation.
- iv) The adjusted radiation response parameters α/β and α for the AT1 tumour subline were comparable to those experimentally determined *in-vitro*.

In summary, this study established a consistent parameter set for the TRM that predicts the oxygen-dependent radiation response of three sublines of an experimental prostate tumour. The model has shown to be a suitable tool to investigate the impact of different biological processes on the radiation response and to study their relative importance for tumour control.

6 Outlook

The present study demonstrated the ability of the TRM to reproduce the response of experimental *in-vivo* tumours after radiation. Some of the most relevant parameters describing the tumour characteristics were determined or were adjusted from existing data, but certain assumptions on the initial simulation conditions were necessary. As previously shown, tumour oxygenation has a great impact on the response, and therefore an estimation of the actual initial vascular fraction (VF) would improve the available information on input parameters and thus reduce the number of additional assumptions required for the parameter adjustment. The VF could in principle be estimated using pharmacokinetic modelling of signals from dynamic contrast-enhanced MRI (DCE-MRI) [56] or ¹⁸F-fluoromisonidazole PET (¹⁸F-MISO-PET) [57], [58], although the resulting values are often rather unstable and model-dependent.

Overall, the TRM was successfully adjusted to reproduce the experimental data on three experimental tumour sublines with the currently implemented oxygenation model. As an alternative oxygenation model, one could consider a spatiotemporal development of the oxygen histograms: Initially, an oxygen histogram would be assigned to each voxel based on an initial VF. Then, the effect of different biological processes on the oxygen distribution would be tracked. With this approach of temporally propagated oxygen histograms, a generally more hypoxic histogram would be obtained after each irradiation as the well-oxygenated and thus more radiosensitive TCs are predominantly killed. Additional investigations are necessary on whether this constitutes a more realistic representation of the oxygen availability for the tumour cells.

Furthermore, the TRM predictions could be compared against clinical patient data, paying particular attention to early-detectable morphological and functional imaging signals. Considering that the tumour control can only be reliably determined years after irradiation, the TRM might rather be used as a short- and medium-term predictive tool after adjusting the input parameters adequately. Studies have shown that hypoxia imaging has strong predictive power when assessed before and during radiotherapy [34], [86], [87]. Complementary, a tumour response model such as the TRM might be able to predict how hypoxic tumours reoxygenate after a sequence of irradiation sessions to decide if a modification of the treatment schedule is required before continuing the treatment.

Appendix

Image processing to count DAPI⁺ cell nuclei

1. Import cleared image to Fiji[‡]
2. "image" → "colour" → "split channels"
3. Keep only blue channel
4. "Process" → "Subtract background" → radius: 100
5. "Image" → "Adjust" → "threshold"
6. "Process" → "Binary" → "make Binary"
7. "Edit" → "Invert"
8. "Process" → "binary" → "Watershed"
9. "Analyse" → "Analyse Particles" → "Size: 30-infinity" in pixel units
10. "Summary" → "count"

Image processing to determine DAPI area

1. Load "mask" to Fiji
2. "Analyse" → "set scale" → "Click to remove scale" → "OK"
3. "Image" → "Adjust" → "threshold"
4. "Analyse" → "Analyse Particles" → "Size: 0-infinity" in pixel units

[‡] Fiji image processing software

Publications

Peer-reviewed scientific articles

I. Paredes-Cisneros, C. P. Karger, P. Caprile, D. Nolte, I. Espinoza, A. Gago-Arias, "Simulation of hypoxia PET-tracer uptake in tumours: Dependence of clinical uptake-values on transport parameters and arterial input function", *Physica Medica*, Vol 70 (2020) 109-117, <https://doi.org/10.1016/j.ejmp.2020.01.012>.

Poster presentations

I. Paredes-Cisneros, "Computer simulation of the radiation response of hypoxic tumours", presented at the 1st German Cancer Research Congress, Heidelberg, Germany, 2019.

I. Paredes-Cisneros, "Computer simulation of the radiation response of hypoxic tumours", presented at the DeGBS Annual Conference *der Deutschen Gesellschaft für Biologische Strahlenforschung e.V.*, Mannheim, Germany, 2019.

I. Paredes-Cisneros, "Simulating the radiation response of in-vivo hypoxic tumours", presented at the German Cancer Research Center PhD Poster presentation, Heidelberg, Germany, 2020.

Bibliography

- [1] American Cancer Society, "Global Cancer Facts & Figures, 4th Edition," 2018.
- [2] R. Atun *et al.*, "Expanding global access to radiotherapy," *Lancet Oncol.*, vol. 16, no. 10, pp. 1153–1186, 2015, doi: 10.1016/S1470-2045(15)00222-3.
- [3] Y. Lievens, J. M. Borras, and C. Grau, "Provision and use of radiotherapy in Europe," *Mol. Oncol.*, vol. 14, no. 7, pp. 1461–1469, 2020, doi: 10.1002/1878-0261.12690.
- [4] M. R. Horsman, L. S. Mortensen, J. B. Petersen, M. Busk, and J. Overgaard, "Imaging hypoxia to improve radiotherapy outcome," *Nat. Rev. Clin. Oncol.*, vol. 9, no. 12, pp. 674–687, 2012, doi: 10.1038/nrclinonc.2012.171.
- [5] P. Vaupel and A. Mayer, "Hypoxia in cancer: Significance and impact on clinical outcome," *Cancer Metastasis Rev.*, vol. 26, no. 2, pp. 225–239, 2007, doi: 10.1007/s10555-007-9055-1.
- [6] L. H. Gray, A. D. Conger, M. Ebert, S. Hornsey, and O. C. Scott, "The concentration of oxygen dissolved in tissues at the time of irradiation as a factor in radiotherapy," *Br. J. Radiol.*, vol. 26, no. 312, pp. 638–648, 1953, doi: 10.1259/0007-1285-26-312-638.
- [7] W. R. Wilson and M. P. Hay, "Targeting hypoxia in cancer therapy," *Nat. Rev. Cancer*, vol. 11, no. 6, pp. 393–410, 2011, doi: 10.1038/nrc3064.
- [8] D. R. Grimes, D. R. Warren, and S. Warren, "Hypoxia imaging and radiotherapy: Bridging the resolution gap," *Br. J. Radiol.*, vol. 90, no. 1076, 2017, doi: 10.1259/bjr.20160939.
- [9] I. Espinoza, "Computer simulation of the radiation response of hypoxic tumours," Heidelberg University, 2013.
- [10] I. Espinoza, P. Peschke, and C. P. Karger, "A voxel-based multiscale model to simulate the radiation response of hypoxic tumors," *Med. Phys.*, vol. 42, no. 1, pp. 90–102, 2015, doi: 10.1118/1.4903298.
- [11] P. Peschke, C. P. Karger, M. Scholz, J. Debus, and P. E. Huber, "Relative biological effectiveness of carbon ions for local tumor control of a radioresistant prostate carcinoma in the rat," *Int. J. Radiat. Oncol. Biol. Phys.*, vol. 79, no. 1, pp. 239–246, 2011, doi: 10.1016/j.ijrobp.2010.07.1976.
- [12] C. P. Karger, P. Peschke, M. Scholz, P. E. Huber, and J. Debus, "Relative biological effectiveness of carbon ions in a rat prostate carcinoma in vivo: Comparison of 1, 2, and 6 fractions," *Int. J. Radiat. Oncol. Biol. Phys.*, vol. 86, no. 3, pp. 450–455, 2013, doi: 10.1016/j.ijrobp.2013.01.019.
- [13] C. Glowa, P. Peschke, S. Brons, J. Debus, and C. P. Karger, "Intrinsic and extrinsic tumor characteristics are of minor relevance for the efficacy of split-dose carbon ion irradiation in three experimental prostate tumors," *Radiother. Oncol.*, vol. 133, pp. 120–124, 2019, doi: 10.1016/j.radonc.2018.12.017.
- [14] C. Glowa, P. Peschke, S. Brons, J. Debus, and C. P. Karger, "Effectiveness of fractionated carbon ion treatments in three rat prostate tumors differing in growth rate, differentiation and hypoxia," *Radiother. Oncol.*, vol. 158, pp. 131–137, 2021, doi: 10.1016/j.radonc.2021.01.038.
- [15] F. M. Khan and J. P. Gibbons, *Khan's The Physics of Radiation Therapy*, 5th ed. Wolters Kluwer Health, 2014.

- [16] E. B. Podgorsak, *Radiation Physics for Medical Physicists*, 2nd ed., vol. 1. Springer International Publishing, Cham, 2009.
- [17] P. Mayles, A. E. Nahum, and J. C. Rosenwald, *Handbook of Radiotherapy Physics - Theory and Practice*. Taylor & Francis Group, CRC Press, 2007.
- [18] F. Salvat and J. M. Fernández-Varea, "Overview of physical interaction models for photon and electron transport used in Monte Carlo codes," *Metrologia*, vol. 46, no. 2, 2009, doi: 10.1088/0026-1394/46/2/S08.
- [19] M. C. Joiner and A. van der Kogel, *Basic Clinical Radiobiology*, 4th ed. London: CRC Press Taylor & Francis Group, 2009.
- [20] B. G. Douglas and J. F. Fowler, "The effect of multiple small doses of X rays on skin reactions in the mouse and a basic interpretation," *Radiat. Res.*, vol. 66, no. 2, pp. 401–426, 1976, doi: 10.2307/3574407.
- [21] S. J. McMahon, "The linear quadratic model: Usage, interpretation and challenges," *Phys. Med. Biol.*, vol. 64, no. 1, 2019, doi: 10.1088/1361-6560/aaf26a.
- [22] J. S. Bedford, "Sublethal damage, potentially lethal damage, and chromosomal aberrations in mammalian cells exposed to ionizing radiations," *Int. J. Radiat. Oncol. Biol. Phys.*, vol. 21, no. 6, pp. 1457–1469, 1991, doi: 10.1016/0360-3016(91)90320-4.
- [23] C. A. Tobias, "The repair-misrepair model in radiobiology: comparison to other models," *Radiat. Res. Suppl.*, vol. 8, no. 104, p. S-77-S-95, 1985, doi: 10.2307/3583515.
- [24] S. B. Curtis, "Lethal and potentially lethal lesions induced by radiation - A unified repair model," *Radiat. Res.*, vol. 106, no. 2, pp. 252–270, 1986, doi: 10.2307/3576798.
- [25] D. T. Goodhead, "Saturable repair models of radiation action in mammalian cells," *Radiat. Res. Suppl.*, vol. 8, no. 104, p. S-58-S-67, 1985, doi: 10.2307/3583513.
- [26] P. Vaupel, "Tumor microenvironmental physiology and its implications for radiation oncology," *Semin. Radiat. Oncol.*, vol. 14, no. 3, pp. 198–206, 2004, doi: 10.1016/j.semradonc.2004.04.008.
- [27] M. R. Horsman, "Measurement of tumor oxygenation," *Int. J. Radiat. Oncol. Biol. Phys.*, vol. 42, no. 4, pp. 701–704, 1998, doi: 10.1016/S0360-3016(98)00332-0.
- [28] R. H. Thomlinson and L. H. Gray, "The Histological Structure of Some Human Lung Cancers and the Possible Implications for Radiotherapy," *Br. J. Cancer*, vol. 9, no. 4, pp. 539–549, 1955, doi: 10.1038/bjc.1955.55.
- [29] M. Nordsmark, M. Overgaard, and J. Overgaard, "Pretreatment oxygenation predicts radiation response in advanced squamous cell carcinoma of the head and neck," *Radiother. Oncol.*, vol. 41, no. 1, pp. 31–39, 1996, doi: 10.1016/S0167-8140(96)91811-3.
- [30] A. Yaromina *et al.*, "Radiobiological hypoxia, histological parameters of tumour microenvironment and local tumour control after fractionated irradiation," *Radiother. Oncol.*, vol. 96, no. 1, pp. 116–122, 2010, doi: 10.1016/j.radonc.2010.04.020.
- [31] S. Welz *et al.*, "Prognostic value of dynamic hypoxia PET in head and neck cancer: Results from a planned interim analysis of a randomized phase II hypoxia-image guided dose escalation trial," *Radiother. Oncol.*, vol. 124, no. 3, pp. 526–532, 2017, doi: 10.1016/j.radonc.2017.04.004.
- [32] D. Thorwarth, S. M. Eschmann, F. Paulsen, and M. Alber, "Hypoxia Dose Painting by Numbers: A Planning Study," *Int. J. Radiat. Oncol. Biol. Phys.*, vol. 68, no. 1, pp. 291–300, 2007, doi: 10.1016/j.ijrobp.2006.11.061.
- [33] D. Thorwarth, X. Geets, and M. Paiusco, "Physical radiotherapy treatment planning based on functional PET/CT data," *Radiother. Oncol.*, vol. 96, no. 3, pp. 317–324, 2010, doi:

- 10.1016/j.radonc.2010.07.012.
- [34] D. Zips *et al.*, “Exploratory prospective trial of hypoxia-specific PET imaging during radiochemotherapy in patients with locally advanced head-and-neck cancer,” *Radiother. Oncol.*, vol. 105, no. 1, pp. 21–28, 2012, doi: 10.1016/j.radonc.2012.08.019.
- [35] T. Alper and P. Howard-Flanders, “Role of oxygen in modifying the radiosensitivity of *E. Coli B.*,” *Nature*, vol. 178, pp. 978–979, 1956.
- [36] D. Robert Grimes and M. Partridge, “A mechanistic investigation of the oxygen fixation hypothesis and oxygen enhancement ratio,” *Biomed. Phys. Eng. Express*, vol. 1, no. 4, p. 045209, 2015, doi: 10.1088/2057-1976/1/4/045209.
- [37] T. R. Munro and C. W. Gilbert, “The relation between tumour lethal doses and the radiosensitivity of tumour cells,” *Br. J. Radiol.*, vol. 34, no. 400, pp. 246–251, 1961, doi: 10.1259/0007-1285-34-400-246.
- [38] J. M. Brown, D. J. Carlson, and D. J. Brenner, “The tumor radiobiology of SRS and SBRT: Are more than the 5 Rs involved?,” *Int. J. Radiat. Oncol. Biol. Phys.*, vol. 88, no. 2, pp. 254–262, 2014, doi: 10.1016/j.ijrobp.2013.07.022.
- [39] L. G. Marcu and W. M. Harriss-Phillips, “In silico modelling of treatment-induced tumour cell kill: Developments and advances,” *Comput. Math. Methods Med.*, vol. 2012, no. i, 2012, doi: 10.1155/2012/960256.
- [40] I. Espinoza, P. Peschke, and C. P. Karger, “A model to simulate the oxygen distribution in hypoxic tumors for different vascular architectures,” *Med. Phys.*, vol. 40, no. 8, pp. 1–12, 2013, doi: 10.1118/1.4812431.
- [41] S. Mang, “How to use TRM with DIPP.” pp. 1–15, 2014.
- [42] I. Liedtke, “Computer simulation of the radiation response of a hypoxic prostate tumor in the rat using a multi-scale tumor response model,” Heidelberg University, 2015.
- [43] A. Daşu, I. Toma-Daşu, and M. Karlsson, “Theoretical simulation of tumour oxygenation and results from acute and chronic hypoxia,” *Phys. Med. Biol.*, vol. 48, no. 17, pp. 2829–2842, 2003, doi: 10.1088/0031-9155/48/17/307.
- [44] I. Toma-Dasu and A. Dasu, “Modelling tumour oxygenation, reoxygenation and implications on treatment outcome,” *Comput. Math. Methods Med.*, vol. 2013, 2013, doi: 10.1155/2013/141087.
- [45] D. Mönnich, E. G. C. Troost, J. H. A. M. Kaanders, W. J. G. Oyen, M. Alber, and D. Thorwarth, “Modelling and simulation of [18F]fluoromisonidazole dynamics based on histology-derived microvessel maps,” *Phys. Med. Biol.*, vol. 56, no. 7, pp. 2045–2057, 2011, doi: 10.1088/0031-9155/56/7/009.
- [46] I. Espinoza, P. Peschke, and C. P. Karger, “A model to simulate the oxygen distribution in hypoxic tumors for different vascular architectures,” *Med. Phys.*, vol. 40, no. 8, 2013, doi: 10.1118/1.4812431.
- [47] A. Neuholz, “3D characterization of vascular architectures in experimental tumors based on LSFM microscopy and simulation of the oxygen distributions,” Heidelberg University, 2021.
- [48] I. Paredes-Cisneros, “Simulation of oxygen and hypoxia PET-tracer distributions in 3D vascular architectures of tumours,” Heidelberg University, DKFZ, 2018.
- [49] I. Paredes-Cisneros, C. P. Karger, P. Caprile, D. Nolte, I. Espinoza, and A. Gago-Arias, “Simulation of hypoxia PET-tracer uptake in tumours: Dependence of clinical uptake-values on transport parameters and arterial input function,” *Phys. Medica*, vol. 70, pp. 109–117, 2020, doi: 10.1016/j.ejmp.2020.01.012.

- [50] I. F. Tannock, "Oxygen diffusion and the distribution of cellular radiosensitivity in tumours.," *Br. J. Radiol.*, vol. 45, no. 535, pp. 515–524, 1972, doi: 10.1259/0007-1285-45-535-515.
- [51] B. W. Pogue, J. A. O'Hara, C. M. Wilmot, K. D. Paulsen, and S. H. M., "Estimation of Oxygen Distribution in RIF-1 Tumors by Diffusion Model-Based Interpretation of Pimonidazole Hypoxia and Eppendorf Measuremen," *Radiat. Res.*, vol. 155, no. 1, pp. 15–25, 2001, doi: 10.1667/0033-7587(2001)155[0015:EODDIR]2.0.CO;2.
- [52] D. C. Chow, L. A. Wenning, W. M. Miller, and E. T. Papoutsakis, "Modeling pO₂ distributions in the bone marrow hematopoietic compartment. II. Modified Kroghian models," *Biophys. J.*, vol. 81, no. 2, pp. 685–696, 2001, doi: 10.1016/S0006-3495(01)75733-5.
- [53] B. Fertil and E. P. Malaise, "Inherent cellular radiosensitivity as a basic concept for human tumor radiotherapy," *Int. J. Radiat. Oncol. Biol. Phys.*, vol. 7, no. 5, pp. 621–629, 1981, doi: 10.1016/0360-3016(81)90377-1.
- [54] D. B. Flint *et al.*, "Cell lines of the same anatomic site and histologic type show large variability in intrinsic radiosensitivity and relative biological effectiveness to protons and carbon ions," *Med. Phys.*, vol. 48, no. 6, pp. 3243–3261, 2021, doi: 10.1002/mp.14878.
- [55] C. Glowa *et al.*, "Flow cytometric characterization of tumor subpopulations in three sublines of the dunning R3327 rat prostate tumor model," *Prostate*, vol. 73, no. 15, pp. 1710–1720, 2013, doi: 10.1002/pros.22710.
- [56] A. Bendinger, "Investigation of hypoxia in syngeneic rat prostate tumors after irradiation with photons or carbon ions by multimodal imaging and histology," Heidelberg University, 2019.
- [57] P. Mena-Romano, "Characterization of hypoxia in three sublines of the Dunning R3327 rat prostate adenocarcinoma using Positron Emission Tomography and histology," p. 114, 2015.
- [58] P. Mena-Romano *et al.*, "Measurement of hypoxia-related parameters in three sublines of a rat prostate carcinoma using dynamic 18F-FMISO-PET-CT and quantitative histology," *Am. J. Nucl. Med. Mol. Imaging*, vol. 5, no. 4, pp. 348–362, 2015, doi: 10.1016/S0167-8140(15)31924-1.
- [59] "scipy.optimize.minimize — SciPy v1.7.1 Manual." [Online]. Available: <https://docs.scipy.org/doc/scipy/reference/generated/scipy.optimize.minimize.html>. [Accessed: 16-Sep-2021].
- [60] "minimize(method='Nelder-Mead') — SciPy v1.7.1 Manual." [Online]. Available: <https://docs.scipy.org/doc/scipy/reference/optimize.minimize-neldermead.html>. [Accessed: 16-Sep-2021].
- [61] J. A. Nelder and R. Mead, "A Simplex Method for Function Minimization," *Comput. J.*, vol. 7, no. 4, pp. 308–313, 1965, doi: 10.1093/comjnl/7.4.308.
- [62] J. Denekamp and B. Hobson, "Endothelial-cell proliferation in experimental tumours," *Br. J. Cancer*, vol. 46, no. 5, pp. 711–720, 1982, doi: 10.1038/bjc.1982.263.
- [63] C. Harting, P. Peschke, K. Borkenstein, and C. P. Karger, "Single-cell-based computer simulation of the oxygen-dependent tumour response to irradiation," *Phys. Med. Biol.*, vol. 52, no. 16, pp. 4775–4789, 2007, doi: 10.1088/0031-9155/52/16/005.
- [64] C. Glowa *et al.*, "Carbon ion radiotherapy decreases the impact of tumor heterogeneity on radiation response in experimental prostate tumors," *Cancer Lett.*, vol. 378, no. 2, pp. 97–103, 2016, doi: 10.1016/j.canlet.2016.05.013.
- [65] H. B. Forrester, C. A. Vidair, N. Albright, C. C. Ling, and W. C. Dewey, "Using Computerized Video Time Lapse for Quantifying Cell Death of X-irradiated Rat Embryo Cells Transfected

- with c- myc or c-Ha- ras 1," *Cancer Res.*, vol. 59, no. 415, pp. 931–939, 1999.
- [66] C. Glowa *et al.*, "Carbon ion radiotherapy decreases the impact of tumor heterogeneity on radiation response in experimental prostate tumors," *Cancer Lett.*, vol. 378, no. 2, pp. 97–103, 2016, doi: 10.1016/j.canlet.2016.05.013.
- [67] B. G. Wouters and J. M. Brown, "Cells at Intermediate Levels Can Be More Important Oxygen in Determining Than the " Hypoxic Fraction " Tumor Response to Fractionated Radiotherapy," *Radiat. Res.*, vol. 147, no. 5, pp. 541–550, 1997.
- [68] A. Yaromina *et al.*, "Exploratory study of the prognostic value of microenvironmental parameters during fractionated irradiation in human squamous cell carcinoma xenografts," *Int. J. Radiat. Oncol. Biol. Phys.*, vol. 80, no. 4, pp. 1205–1213, 2011, doi: 10.1016/j.ijrobp.2011.02.015.
- [69] P. Nickers, J. Hermesse, J. M. Deneufbourg, S. Vanbelle, and E. Lartigau, "Which α/β ratio and half-time of repair are useful for predicting outcomes in prostate cancer?," *Radiother. Oncol.*, vol. 97, no. 3, pp. 462–466, 2010, doi: 10.1016/j.radonc.2010.06.006.
- [70] C. Proust-Lima *et al.*, "Confirmation of a low α/β ratio for prostate cancer treated by external beam radiation therapy alone using a post-treatment repeated-measures model for PSA dynamics," *Int. J. Radiat. Oncol. Biol. Phys.*, vol. 79, no. 1, pp. 195–201, 2011, doi: 10.1016/j.ijrobp.2009.10.008.
- [71] R. Shaffer, T. Pickles, R. Lee, and V. Moiseenko, "Deriving prostate alpha-beta ratio using carefully matched groups, long follow-up and the phoenix definition of biochemical failure," *Int. J. Radiat. Oncol. Biol. Phys.*, vol. 79, no. 4, pp. 1029–1036, 2011, doi: 10.1016/j.ijrobp.2009.12.058.
- [72] R. Valdagni *et al.*, "Is the alpha-beta ratio of prostate cancer really low? A prospective, non-randomized trial comparing standard and hyperfractionated conformal radiation therapy," *Radiother. Oncol.*, vol. 75, no. 1, pp. 74–82, 2005, doi: 10.1016/j.radonc.2004.12.019.
- [73] I. R. Vogelius and S. M. Bentzen, "Meta-analysis of the alpha/beta ratio for prostate cancer in the presence of an overall time factor: Bad news, good news, or no news?," *Int. J. Radiat. Oncol. Biol. Phys.*, vol. 85, no. 1, pp. 89–94, 2013, doi: 10.1016/j.ijrobp.2012.03.004.
- [74] I. R. Vogelius and S. M. Bentzen, "Dose Response and Fractionation Sensitivity of Prostate Cancer After External Beam Radiation Therapy: A Meta-analysis of Randomized Trials," *Int. J. Radiat. Oncol. Biol. Phys.*, vol. 100, no. 4, pp. 858–865, 2018, doi: 10.1016/j.ijrobp.2017.12.011.
- [75] S. G. Williams *et al.*, "Use of Individual Fraction Size Data from 3756 Patients to Directly Determine the α/β Ratio of Prostate Cancer," *Int. J. Radiat. Oncol. Biol. Phys.*, vol. 68, no. 1, pp. 24–33, 2007, doi: 10.1016/j.ijrobp.2006.12.036.
- [76] B. G. Douglas and J. F. Fowler, "The effect of multiple small doses of X rays on skin reactions in the mouse and a basic interpretation," *Radiat. Res.*, vol. 178, no. 2, pp. AV125–AV138, 2012, doi: 10.2307/3574407.
- [77] C. von Neubeck, "Radiobiological experiments for carbon ion prostate cancer therapy: Interplay of normal and tumor cells in co-culture and measurement of the oxygen enhancement ratio," Technische Universität Darmstadt, 2009.
- [78] J. P. Kirkpatrick, D. J. Brenner, and C. G. Orton, "The linear-quadratic model is inappropriate to model high dose per fraction effects in radiosurgery," *Med. Phys.*, vol. 36, no. 8, pp. 3381–3384, 2009, doi: 10.1118/1.3157095.
- [79] M. Z. Dewan *et al.*, "Fractionated but not single-dose radiotherapy induces an immune-mediated abscopal effect when combined with anti-CTLA-4 antibody," *Clin. Cancer Res.*,

- vol. 15, no. 17, pp. 5379–5388, 2009, doi: 10.1158/1078-0432.CCR-09-0265.
- [80] G. G. Hanna, V. M. Coyle, and K. M. Prise, “Immune modulation in advanced radiotherapies: Targeting out-of-field effects,” *Cancer Lett.*, vol. 368, no. 2, pp. 246–251, 2015, doi: 10.1016/j.canlet.2015.04.007.
- [81] M. Guckenberger *et al.*, “Applicability of the linear-quadratic formalism for modeling local tumor control probability in high dose per fraction stereotactic body radiotherapy for early stage non-small cell lung cancer,” *Radiother. Oncol.*, vol. 109, no. 1, pp. 13–20, 2013, doi: 10.1016/j.radonc.2013.09.005.
- [82] G. Borst *et al.*, “Radiation pneumonitis after hypofractionated radiotherapy: evaluation of the LQ(L) model and different dose parameters,” *Int. J. Radiat. Oncol. Biol. Phys.*, vol. 77, no. 5, pp. 1596–1603, 2010, doi: 10.1016/j.ijrobp.2009.10.015.
- [83] A. C. Tree, V. S. Khoo, N. J. Van As, and M. Partridge, “Is Biochemical Relapse-free Survival After Profoundly Hypofractionated Radiotherapy Consistent with Current Radiobiological Models?,” *Clin. Oncol.*, vol. 26, no. 4, pp. 216–229, 2014, doi: 10.1016/j.clon.2014.01.008.
- [84] I. Shuryak, D. J. Carlson, J. M. Brown, and D. J. Brenner, “High-dose and fractionation effects in stereotactic radiation therapy: Analysis of tumor control data from 2965 patients,” *Radiother. Oncol.*, vol. 115, no. 3, pp. 327–334, 2015, doi: 10.1016/j.radonc.2015.05.013.
- [85] T. Wenzl and J. J. Wilkens, “Theoretical analysis of the dose dependence of the oxygen enhancement ratio and its relevance for clinical applications,” *Radiat. Oncol.*, vol. 6, no. 1, pp. 1–9, 2011, doi: 10.1186/1748-717X-6-171.
- [86] D. Thorwarth *et al.*, “Prospective Evaluation of a Tumor Control Probability Model Based on Dynamic 18 F-FMISO PET for Head and Neck Cancer Radiotherapy,” *J. Nucl. Med.*, vol. 60, no. 12, pp. 1698–1704, 2019, doi: 10.2967/jnumed.119.227744.
- [87] A. Sörensen *et al.*, “Textural features of hypoxia PET predict survival in head and neck cancer during chemoradiotherapy,” *Eur. J. Nucl. Med. Mol. Imaging*, no. 47, pp. 1056–1064, 2020.

Acknowledgements

First and foremost, I would like to express my gratitude to my supervisor Prof. Dr. Christian Karger. Christian guided me with endless patience and supported me through the challenging phases of my project. Under his supervision, I was able to observe and learn from his exceptional scientific and work practices. I am lucky to carry these lessons with me for the rest of my career.

I would also like to thank my first reviewer Prof. Dr. Joao Seco for his guidance and interest in my project, and Dr. Ralf Floca for supporting the computational aspect of my project.

I am very grateful to all the colleagues at the DKFZ that further supported my PhD. From the Medical Image Computing Team, I am especially thankful to Dr. Sarina Thomas and Stephen Schaumann, for their hands-on assistance with the code maintenance and improvement. From the Radiotherapy Optimisation group, I would like to thank Dr. Niklas Wahl for his advice on code optimisation. I am also grateful to Dr. Christin Glowa for supporting the biological aspects of my project. I would also like to thank my colleagues at the PhD Program Office for their support and encouragement while working and writing my thesis.

My PhD in Germany was greatly motivated by the mentors I met during my time in Chile. I would like to thank Dr. Ignacio Espinoza and Dr. Araceli Gago-Arias for setting the path for my PhD and for their continuous encouragement during all these years. I am also thankful to Dr. Pamela Mena-Romano, for her coaching and overall support while writing this thesis.

During the past years, I have met many people that today continue to make this a remarkable part of my life. To all my colleagues in the E0402 group at the DKFZ, thanks for the great times in and outside the office. I am especially thankful to Dr. Alexander Neuholz and Dr. Amit Bennan for their constant support with my project and for their friendship during both the fun and the difficult times. I am also thankful to all my friends that stood by my side through this intensely transformative period. In particular, I am thankful to Nikhil for his unconditional support, his patience and for the many ways he comforted me during this time.

Last but not least, I am deeply thankful to my family: Darío Vicente, María del Carmen, Darío and Santiago. They have been my cheerleaders from the very beginning, even now when we are many kilometres apart. I thank you for supporting me in every way and for providing me with everything I needed to become the person I am today.